Electron Dynamics of Cs covered Cu(111): A Scanning Tunneling Spectroscopy Investigation at Low Temperatures

Dissertation
zur Erlangung des Doktorgrades der
Mathematisch-Naturwissenschaftlichen Fakultät
der Christian-Albrechts-Universität
zu Kiel

vorgelegt von
Thomas von Hofe

Kiel 2005

Referent/in: Prof. Dr. Richard Berndt
Korreferent/in: Prof. Dr. Lutz Kipp
Tag der mündlichen Prüfung: 30. Januar 2006
Zum Druck genehmigt: Kiel,

Der Dekan

Kurzdarstellung

Während dieser Arbeit wurde ein Rastertunnelmikroskop, das im Ultrahochvakuum und bei tiefen Temperaturen arbeit, aufgebaut und um eine Probenheizung zum Betrieb bei verschiedenen Temperaturen erweitert. Desweiteren wurde eine weitere Stufe der Vibrationsdämpfung entworden und in Betrieb genommen.

Untersucht wurde Cu(111)-Cs bei verschiedenen Bedeckungen. Bei einer Bedeckung von $\Theta = 0.05\,\mathrm{ML}$ zeigt die Schicht eine kommensurable $(\sqrt{19} \times \sqrt{19}\mathrm{R}23.4^\circ$ Struktur, die womöglich durch Wechselwirkungen, die durch den Substrat-Oberflächenzustand übertragen werden, stabilisiert wird. Bei höheren Bedeckungen ist die Cs-Schicht inkommensurabel und gegen das Substrat gedreht. Der Drehwinkel hängt dabei von der Bedeckung ab. Bei der Sättigungsbedeckung von $\Theta = 0.25\,\mathrm{ML}$ ist die Schicht kommensurabel, jedoch nicht geschlossen, sondern weist viele Defekte auf.

Die Bindungsenergie des Quantum Well States (QWS), der sich in der Cs-Schicht bildet, nimmt mit zunehmender Bedeckung ab. Dieses Verhalten wurde bereits für andere Systeme beobachtet. Die Lebensdauer des QWS nimmt mit der Bindungsenergie ab. Die verhältnismäßig lange Lebensdauer für Cu(111)-p(2×2)Cs führte zur Einführung der Brillouinzonen-Rückfaltung, eines neuen Prozesses, der die Lebensdauer verkürzt. Die Messung der Dispersionskurven des QWS für verschiedene Bedeckungen ergab, dass die effective Masse mit steigender Bindungenergie abnimmt.

Abstract

During this Ph.D. a scanning tunneling microscope operating in ultra-high vacuum and at low temperatures was assembled and modified to allow operation at variable temperatures. Also, an additional vibration isolation stage was conceived and mounted.

Measurements were performed on Cu(111)-Cs for different coverages. For a coverage of $\Theta = 0.05\,\mathrm{ML}$, the layer shows a commensurate $(\sqrt{19} \times \sqrt{19}\mathrm{R}23.4^\circ$ structure which may be stabilized by surface-state mediated adatom interactions. For higher coverages, the layer is incommensurate and rotated with respect to the substrate, where the angle of rotation depends on the coverage. At the saturation coverage $\Theta = 0.25\,\mathrm{ML}$, the layer, although commensurate, reveals many defects.

The binding energy of the quantum well state (QWS) confined to the Cs layer decreases with increasing coverage as has been observed before for other systems. The lifetime of the QWS decreases with increasing binding energy. The comparatively short lifetime for Cu(111)-p(2×2)Cs led to the introduction of Brillouin Zone Backfolding as a new lifetime-limiting process. Acquisition of dispersion relations of the QWS for different coverages revealed that the effective mass of the excitations increases with decreasing binding energy.

Contents

1 Introduction **1**

2 Scanning Tunneling Microscopy **3**

2.1 Principles of Tunneling 3

2.2 Topographical imaging 5

2.3 Spectroscopy 8

2.3.1 dI/dU-spectroscopy 8

2.3.2 $z(U)$-spectroscopy 9

2.3.3 $I(z)$-spectroscopy 10

2.4 dI/dU-maps 10

3 Experimental **12**

3.1 Overview 12

3.1.1 Preparation Chamber 14

3.1.2 Analysis Chamber 15

3.2 HEAT! — The Bake-out Controller 16

3.3 Variable Temperature STM — The new Slider 20

3.4 Damping the Cryostat 25

4 Lifetimes of Electronic Excitations **29**

4.1 Types of states localized at the surface 29

4.1.1 Surface states 29

4.1.2 Image potential states 33

4.1.3 Field-emission resonances 35

4.1.4 Quantum well states 37

4.2 Influences on the lifetime 39

4.2.1 Electron-electron scattering 40

4.2.2 Electron-phonon scattering 42

4.2.3 Electron-defect scattering 43
4.2.4 Brillouin zone back folding 44

5 Evaluation of Measured Spectra 46
5.1 Line shape 46
5.2 Broadening by lock-in modulation 48

6 Cesium on Copper(111) 52
6.1 Introduction 52
6.2 Geometric Structure 54
6.2.1 Low Coverage: $\Theta = 0.05\,\mathrm{ML}$ 54
6.2.2 Intermediate coverage: $\Theta = 0.15 - 0.20\,\mathrm{ML}$ 57
6.2.3 Saturation coverage: $\Theta = 0.25\,\mathrm{ML}$ 63
6.3 Electronic Properties 66
6.3.1 $z(U)$-characteristics 66
6.3.2 $\mathrm{d}I/\mathrm{d}U$-spectroscopy 67
6.3.3 Dispersion relations 70

7 Summary 74

A Cesium on Silver(111) 75

B Low-Temperature STM on Silicon 80
B.1 Silicon(111)-7×7 80
B.1.1 Preparation of Si(111)-7×7 80
B.1.2 Scanning Tunneling Spectroscopy on Si(111) 83
B.2 Indium on Silicon(111) 84

List of Figures

2.1 The tunneling effect 4
2.2 Energy levels during tunneling 6
2.3 Principle of scanning a surface 7
2.4 The two modes of operation of the STM 7
2.5 dI/dU- and $z(U)$-spectroscopy 9

3.1 Overview of the apparatus 13
3.2 The preparation chamber 14
3.3 The shields around the STM 16
3.4 The STM 17
3.5 The main window of the bake out controller HEAT! 19
3.6 The main window of the bake out controller HEAT! 19
3.7 Modified slider 21
3.8 Progression of temperature after heating 22
3.9 Heating power for different temperatures 23
3.10 Prediction of the powers needed to keep the temperature constant 25
3.11 Damping assembly 26
3.12 Frequencies measured on the damped and undamped cryostat . 27

4.1 Localization of the surface state 30
4.2 Formation of direct and inverted band gaps 32
4.3 The image potential 34
4.4 Comparison between surface and image potential states 35
4.5 Field emission resonances 36
4.6 Field emission resonances of Si(111)-Sn 37
4.7 Formation of QWS 38
4.8 Electron-electron scattering processes 41
4.9 Electron-phonon scattering 42
4.10 Back folding 44

5.1 Example of different fitting intervals 47
5.2 Influence of the fitting interval on the resulting width 48
5.3 Graphical evaluation of the width Δ of a state 49
5.4 Broadening of the width of a state by modulation 50
5.5 Correction factor for the measured width 50

6.1 LEED image of clean Cu(111) 55
6.2 Cu(111)-Cs, $\Theta = 0.05\,\mathrm{ML}$ 56
6.3 Cu(111)-Cs, $\Theta = 0.18\,\mathrm{ML}$ 58
6.4 Rotation angle of the Cs adlayer on Cu(111) 59
6.5 Cu(111)-Cs, $\Theta = 0.25\,\mathrm{ML}$ 63
6.6 Cu(111)-Cs, $\Theta = 0.25\,\mathrm{ML}$, at different voltages 64
6.7 $\mathrm{d}I/\mathrm{d}U$-spectra acquired over the Cs-layer and a defect 65
6.8 $z(U)$-spectroscopy on Cu(111)-Cs 66
6.9 Distribution of the binding energies 67
6.10 Scanning tunneling spectra on Cu(111)-Cs at different coverages 68
6.11 Coverage-dependence of the binding energy of the QWS 69
6.12 Experimental width in dependence on the binding energy . . . 70
6.13 $\mathrm{d}I/\mathrm{d}U$-spectrum of surface state and QWS on Cu(111)-Cs 71
6.14 Scattering of the QWS 72
6.15 Line profile from a scattered QWS 73
6.16 Dispersion relations for Cu(111)-Cs 73

A.1 LEED of Ag(111)-Cs at saturation coverage 76
A.2 Constant-current images of Ag(111)-Cs 78
A.3 Binding energy of the QWS of Ag(111)-Cs 79

B.1 The Si-Sampleholder 81
B.2 LEED images of Si(111)-7×7 82
B.3 Si(111)-7×7 83
B.4 Spectra acquired on Si(111) at 9 K 84
B.5 Band structure in a metal-semiconductor junction 85
B.6 The In-evaporator 86
B.7 Large-scale view of Si(111)-In 86
B.8 Topographies and $\mathrm{d}I/\mathrm{d}U$ maps of Si(111)-In 88

List of abbreviations

2DEG	2-Dimensional Electron Gas
2PPE	2-Photon Photoemission
DOS	Density of States
IPES	Inverse Photoemission Spectroscopy
LDOS	Local Density of States
QWS	Quantum Well State
SBZ	Surface Brioullin Zone
SPM	Scanning Probe Microsopy
STM	Scanning Tunnelling Microscopy/Microscope
STS	Scanning Tunnelling Spectroscopy
UHV	Ultrahigh Vacuum

Chapter 1

Introduction

The ongoing miniaturization, especially in computer technology, described by Moore's law [1], requires knowledge about structures at the nanometer scale, where surfaces play an important role. Moreover, the electronic properties of surfaces are of fundamental interest, and in particular the lifetimes of excitations of electronic states since they are important for processes at surfaces, e.g. in catalysis and solar cells. Surfaces have therefore become a major field of research in the last decades.

There is a variety of techniques to examine the properties of surfaces [2]. Since the invention of the Scanning Tunneling Microscope (STM) by Gerd Binnig, Heinrich Rohrer, Christoph Gerber and Edmund Weibel [3, 4] a new powerful technique is available. With the STM it is possible to obtain information about the atomic position in real space, which was demonstrated impressively when STM solved the long-standing problem of the geometry of the Si(111)-(7×7) surface [5]. The possibility to perform tunneling spectroscopy [6] with the STM [7,8] opened the path to spatially resolved spectroscopy of the occupied as well as the unoccupied states of the surface. Recently, it has been demonstrated that the STM is capable of vibrational spectroscopy of single molecules [9], extending the capabilities of the STM by the possibility to chemically identify adsorbates.

In this work, a scanning tunneling microscope operated at low temperatures (9 K, 55 K and 80 K) and room temperature and ultra-high vacuum was assembled. The thesis is organized as follows.

Chapter 2 gives a brief introduction to the theory of scanning tunneling microscopy and spectroscopy.

Chapter 3 presents the apparatus and modifications that were made as part of this work: A PC based controller for bake out of the apparatus was developed in cooperation with J. Neubauer. The STM was extended by the possibility to heat the sample in order to allow for variable-temperature scanning tunneling microscopy. The design of the heating stage and first tests are presented as well as extended calculations concerning the working parameters. Additionally, a new vibration isolation stage for the helium cryostat was conceived and

mounted. Successful operation is demonstrated.

Chapter 4 discusses different types of surface-localized states and influences on their lifetime.

The evaluation of scanning tunneling spectra is described in Chapter 5. Two approaches for evaluation (geometric line-shape analysis and curve fitting) are compared and discussed. Calculations on the broadening of spectra due to the lock-in modulation are presented.

Chapter 6 presents measurements on Cesium on Copper(111). At low coverages, a commensurate phase which is stabilized by surface-state mediated adatom interactions was observed. For coverage near the saturation coverage, rotation of the adlayer with respect to the substrate depending on the coverage was found. The binding energy and the lifetime of quantum well states have been examined in dependence on the coverage using different types of spectroscopy. The results showed that the process of *Brillouin Zone Backfolding*, which had so far not been taken into account, shortens the lifetime of electronic excitations.

Additionally, first measurements on Ag(111)-Cs and Si(111)-(7×7)In have been performed. Due to time limitations only preliminary results are available that are presented in the appendices.

Chapter 2

Scanning Tunneling Microscopy

This chapter gives a brief introduction into STM, starting with the basic principles, and explaining the topographical and spectroscopical modes of operation.

2.1 Principles of Tunneling

In a scanning tunneling experiment, an atomically sharp metallic tip is positioned above a surface in a distance of a few Å. For electrons in the tip, the vacuum gap is a barrier they can not pass offhand. The situation is sketched in Fig. 2.1: In classical mechanics, an electron hitting the barrier is reflected when its energy E is lower than the barrier height V_0, as depicted in Fig. 2.1a. Only when $E > V_0$, the electron will pass the barrier. Since in quantum mechanics the behavior of electrons is described by their wave function which is also defined inside the barrier, there is a probability for the electron to pass the barrier, shown in Fig. 2.1b. Solving the Schrödinger equation for a step-like barrier (see e.g. [10]), one obtains for the transmitted wave function Ψ

$$\Psi = \Psi_0 e^{-\kappa z}, \quad \kappa = \frac{\sqrt{2m(V_0 - E)}}{\hbar} \tag{2.1}$$

with Ψ_0 the incoming wave function, κ the decay constant, z the width and V_0 the height of the barrier, m the mass and E the energy of the electron, and $\hbar$ Planck's constant divided by 2π. Thus, for sufficiently small barriers, the wave function of the electron does not vanish after passing the barrier, the electron can therefore *tunnel* through the barrier.

When a voltage is applied to the barrier, the tunneling electrons lead to a current

$$I \sim |\Psi|^2 = |\Psi_0|^2 e^{-2\kappa z}. \tag{2.2}$$

The current depends exponentially on the width of the tunneling barrier. With a typical barrier height of $\approx 4\,\text{eV}$ in an experiment, resulting in $\kappa \approx 1\,\text{Å}^{-1}$, this means that increasing the barrier width by 1 Å decreases the current by about one order of magnitude.

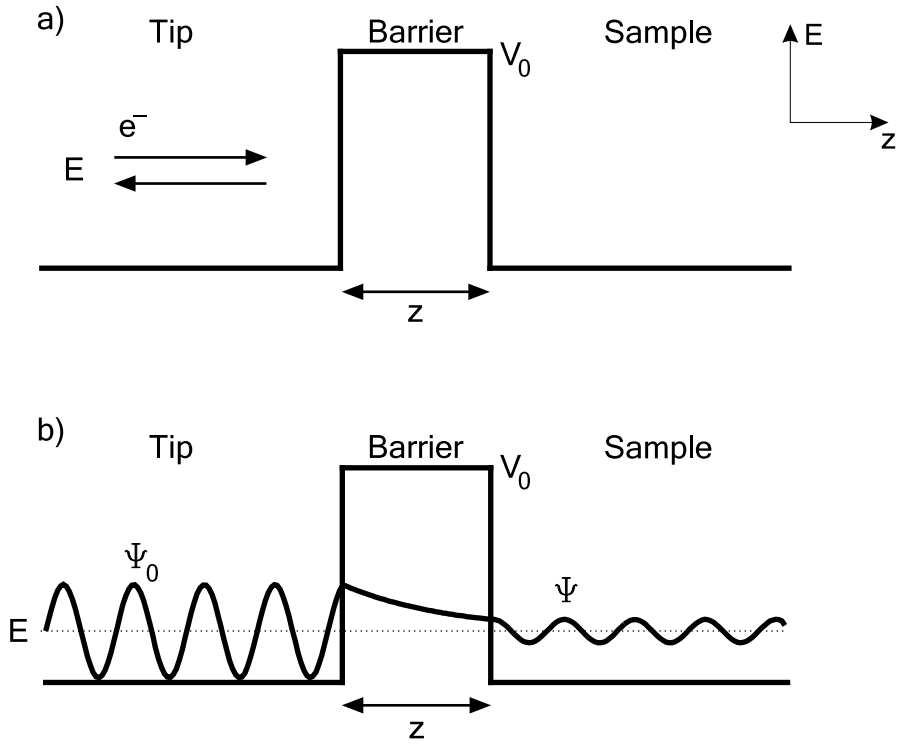

Figure 2.1: The tunneling effect. a) Classical situation: The electron can not pass the barrier, when its energy E is lower than the barrier V_0. b) Quantum mechanical situation: Because the wave function is also defined inside the barrier, there is a probability for the electron to pass the barrier, although its energy is not high enough. This process is called the *tunneling process.*

A more detailed analysis of the tunneling current [11–13] gives for the tunneling current density j:

$$j \approx \frac{2\pi e}{\hbar}\left(\frac{\hbar^2}{2m}\right)^2 \int_{-\infty}^{\infty} T(E,U,z)[f(E+eU)-f(E)]\rho_T(E+eU)\rho_S(E)\,dE, \quad (2.3)$$

where e denotes the electron charge, $f(E)$ the Fermi function, E the energy, U the applied voltage, and ρ_T (ρ_S) the local density of states (LDOS) of the tip (sample). The transmission coefficient T is defined as

$$T(E,U,z) \approx \exp\left\{-2z\sqrt{\frac{2m}{\hbar^2}\left[\bar{\Phi}+\frac{eU}{2}-(E-E_{||})\right]}\right\} \quad (2.4)$$

with E_F the Fermi energy, z the distance, $\bar{\Phi}$ the average of work function of the tip and the sample, and $E_{||}$ the energy of the electron in the surface plane. The current does not only depend on the distance, but also contains information about the LDOS of the surface, ρ_S, and the tip, ρ_T – the latter is usually assumed to be constant in the energy range of interest [11, 12]. At sufficiently low temperatures, the Fermi functions in (2.3) can be approximated by step

functions, and the limits of the integral become E_F (Fermi energy, chosen to be 0) and $E_F + eU$. Thus, the current becomes approximately

$$I \propto \int_0^{eU} \rho_S(E_F + E) T(E_F + E, U, z)\, dE \tag{2.5}$$

Fig. 2.2 illustrates the processes taking place when the tip approaches the surface. While tip and sample are separated, the vacuum levels are the same, whereas the Fermi levels $E_{F,T}$ and $E_{F,S}$ adjust to each other when tip and sample come into tunneling contact. As soon as a voltage is applied between tip and sample, electrons tunnel from occupied states of the tip to unoccupied states of the sample (or vice versa, depending on the voltage polarity). The resulting current is therefore proportional to the sum of the density of unoccupied states, weighted by the transmission coefficient, as described by (2.5).

2.2 Topographical imaging

The mode of operation the STM has become famous for is the topographical imaging. The basic principle of this is sketched in Fig. 2.3. The tip is positioned over the surface by a piezo[1] device which can move the tip in the x-, y- and z-directions. When the voltage U_T is applied between tip and sample, a current I_T will flow through the gap. To keep the current constant while the tip is scanned over the surface in the xy-plane, the control unit CU (the *feedback loop*) adjusts the distance z by varying the voltage U_z applied to the z-piezo P_z. Recording the changes in U_z in dependence on the x/y-position, one obtains detailed information about the LDOS according to Eq. 2.5. Surface steps (A in Fig. 2.3) can easily be detected and identified, but other features in the image can be difficult to interpret. Since the tunneling current is an integral over the LDOS, areas of different LDOS (B in Fig. 2.3) may appear as protrusions (C) or indentations. As has been shown by Lang [16, 17], the apparent height of atoms depends on the voltage due to the energy dependence of the DOS of atoms. Depending on the voltage, adatoms can appear as protrusions, indentations [18], and they can disappear completely in the images [17]. Because the images obtained do not necessarily show the real topography of the surface, it is reasonable to use the term *constant-current images* instead of *topographies*.

As an alternative to the constant-current mode, one can use the constant-height mode. The difference between the two modes is shown in Fig. 2.4. While in constant-current mode the tip-sample distance is adjusted to keep the current constant, the distance is not adjusted in constant-height mode, resulting in changes of the current, which contain the information about the LDOS. The advantage of this mode of operation is that the tip can be scanned across the surface very fast, because the height-adjustment is omitted. On the other

[1] Piezo ceramics, or piezos for short, are materials that elongate or contract when a voltage is applied to them. These changes in length are in the range of a few 10 Å/V, therefore piezos are used when the steps of mechanical motors are too large.

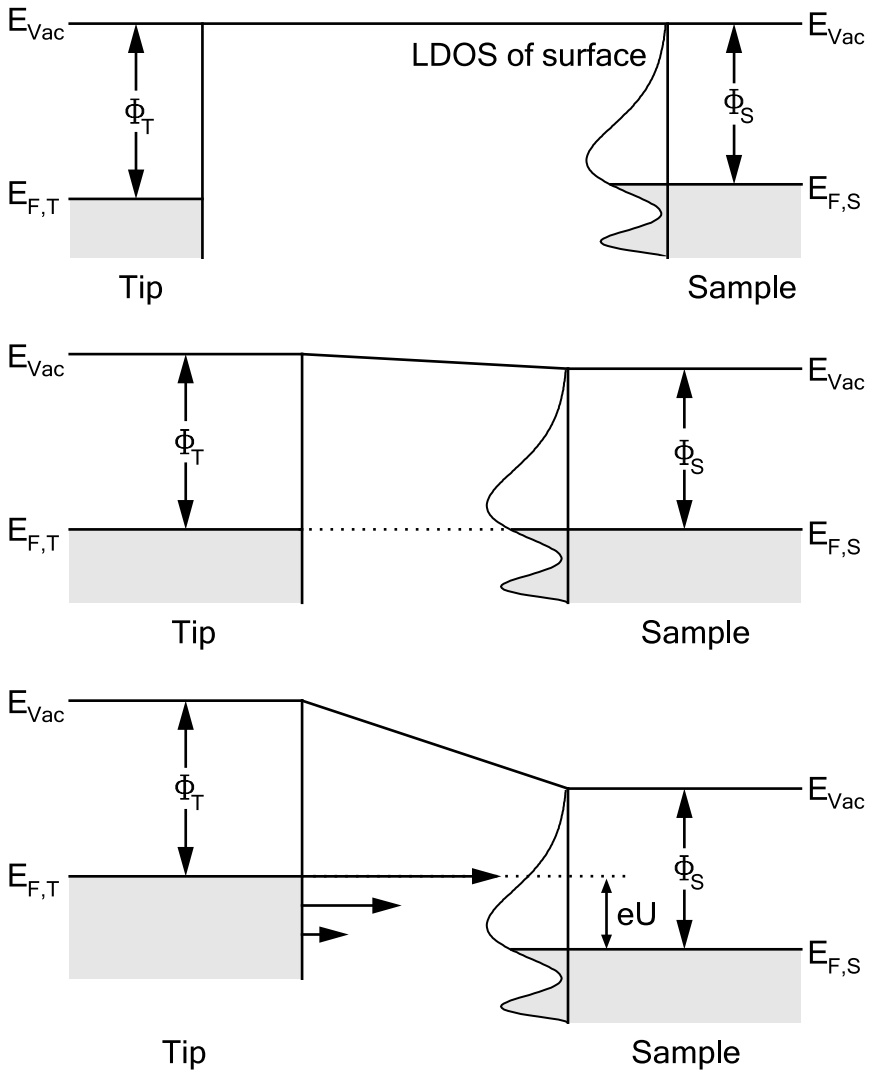

Figure 2.2: Energy levels of tip (left) and sample (right) while tunneling. The sample surface LDOS is structured, while the LDOS of the tip is considered unstructured. The energy bands of tip and sample are filled with electrons up to the Fermi energies $E_{F,T}$ and $E_{F,S}$, respectively. The difference between the vacuum energy levels and the Fermi levels are the work functions Φ_T and Φ_S. Top: Tip and sample are separated, the vacuum energy levels E_{Vac} are the same. Middle: Tip and sample are in tunneling contact, the Fermi levels $E_{F,S}$ and $E_{F,T}$ are adjusted to each other. Bottom: A voltage U is applied between tip and sample, and electrons are tunneling from occupied states of the tip to unoccupied states of the sample. Due to the transmission coefficient T, the density of the tunneling electrons becomes the lower the larger the difference of the electron energy and the Fermi level. Thus, the tunneling current is a weighted sum of the LDOS of the sample surface. (Adapted from [14].)

hand, adjusting the height prevents the tip from colliding with protrusions or loosing tunneling contact above indentations.

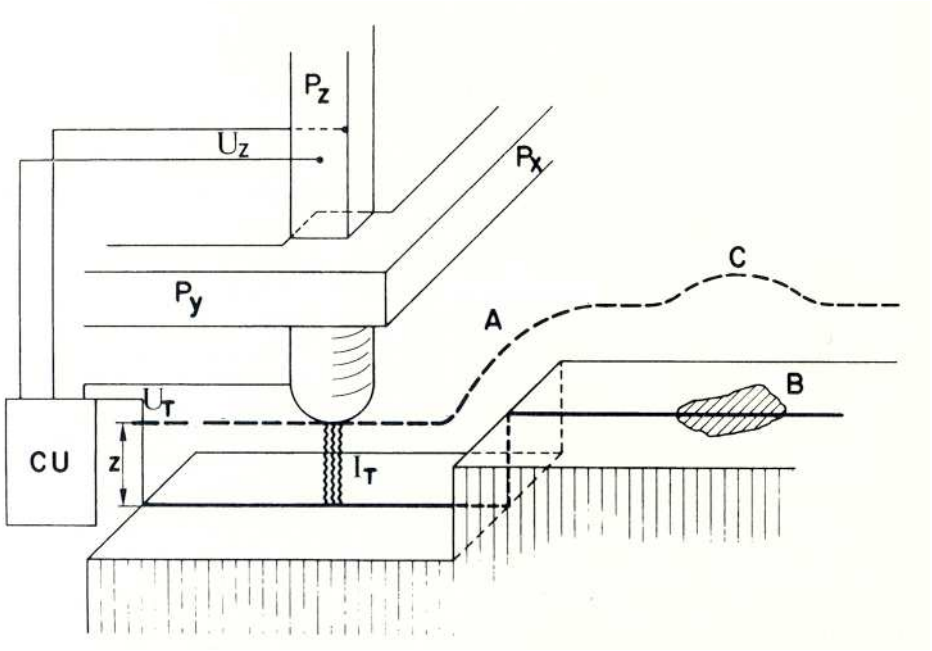

Figure 2.3: Principle of scanning a surface. The tip is positioned over the surface using the piezos P_x, P_y and P_z. While the tip is scanned across the surface, the distance of the tip to the surface is controlled such that the tunneling current is constant. This way, the tip follows the contours of steps (A). If there is a defect in the surface (B), this might appear as a protrusion (C) or an indentation. (Adapted from [15].)

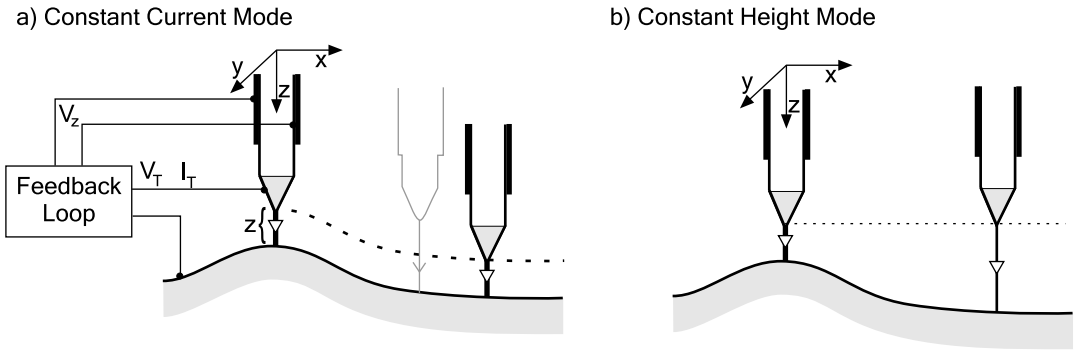

Figure 2.4: The two modes of operation of the STM. a) Constant Current Mode. While scanning the tip over the surface in the x- and y-direction, the height z of the tip is adjusted by the feedback loop to keep the current constant. The adjustments of the tip carry the LDOS information. b) The height of the tip is kept constant while scanning the tip. The current depends on the distance z between tip and surface and carries the information. (Adapted from [19].)

2.3 Spectroscopy

2.3.1 dI/dU-spectroscopy

The integration of the surface LDOS in (2.5) makes it difficult to obtain information about the LDOS at a certain energy. Taking the derivative of the tunneling current solves this problem:

$$\begin{aligned}\frac{dI}{dU} \propto\ & e\rho_S(E_F+eU)T(E_F+eU,U,z) \\ & +\int_0^{eU}\rho_S(E_F+E)\frac{dT}{dU}(E_F+E,U,z)\,dE \\ & +\int_0^{eU}\rho_S(E_F+E)\frac{dT}{dz}(E_F+E,U,z)\frac{dz}{dU}\,dE\end{aligned} \tag{2.6}$$

The third term vanishes when the tip is held at constant height z. The transmission coefficient T varies monotonously and smooth with voltage, its derivative does hence not change the position of peaks and onsets in dI/dU [20]. Thus, the second term is neglected. Then, the derivative is approximately proportional to the surface LDOS:

$$\frac{dI}{dU} \sim e\rho_S(E_F+eU)T(E_F+eU,U,z) \tag{2.7}$$

By determining $dI/dU(U)$, one obtains the LDOS of the sample surface.

The easiest way to obtain $dI/dU(U)$ would be to measure $I(U)$ and calculate the derivative numerically. However, experimental data show a certain amount of noise, which is of low amplitude, but high frequency compared to the features of the undisturbed data. When taking the derivative of experimental data, the noise may dominate the result, and the interesting features can be completely hidden.

Thus, it is better to directly measure the derivative of the tunneling current using a lock-in technique [21, 22]. An AC voltage $\Delta U = U_L\cos(\omega_L t)$ with small amplitude U_L and frequency ω_L is added to the tunneling voltage. The effect on the tunneling current can not be evaluated generally, but the current can be expressed using the Taylor-expansion as

$$\begin{aligned}I(U+\Delta U) &= I(U)+\frac{dI(U)}{dU}\Delta U+\frac{1}{2}\frac{d^2I(U)}{dU^2}(\Delta U)^2+\dots \\ &= I(U)+\frac{dI(U)}{dU}U_L\cos(\omega_L t)+\frac{1}{2}\frac{d^2I(U)}{dU^2}(U_L\cos(\omega_L t))^2+\dots\end{aligned} \tag{2.8}$$

A lock-in amplifier is used to detect the signal proportional to $\cos(\omega_L t)$ and hence measure dI/dU.

If the modulation amplitude U_L is too large, terms of higher order in (2.8) can no longer be neglected. These will lead to an amplitude-depended broadening of the dI/dU-signal [23] which can not easily be taken care of.

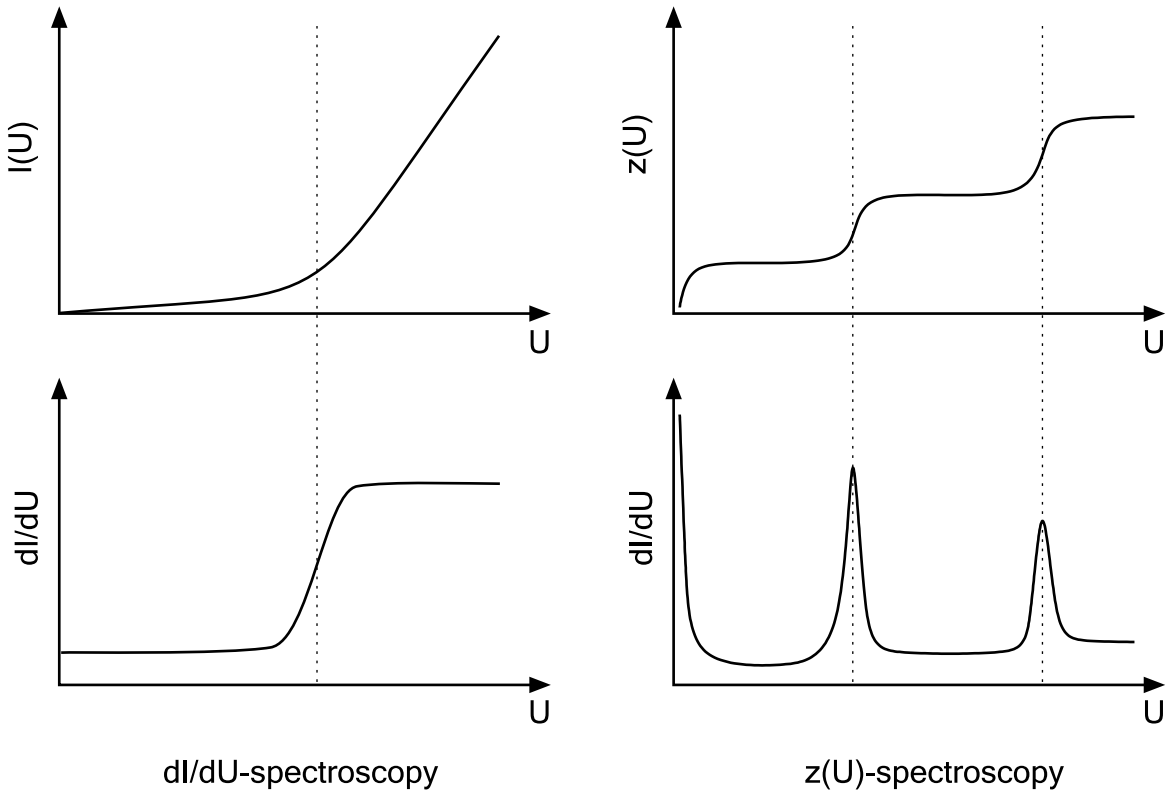

Figure 2.5: dI/dU- (left) and $z(U)$-spectroscopy (right). During dI/dU-spectroscopy, the z-position of the tip is constant (feedback loop off). While ramping the voltage U, the current and its first derivative is recorded. When the voltage reaches a new tunneling channel, the slope of the current increases, resulting in a step in the derivative. In $z(U)$-spectroscopy, the current is constant (feedback loop on). While ramping the voltage, the z-position and the derivative of the current is recorded. When the voltage reaches new tunneling channels (states), steps appear in the $z(U)$-curve, and sharp peaks appear in the dI/dU-curve.

A typical result of dI/dU-spectroscopy is sketched in Fig. 2.5 on the left side: The tip is held at constant height, so the current increases when the voltage is ramped. When the voltage reaches the energy of a new tunneling channel (state), the current increases faster (higher slope), leading to a step in the simultaneously recorded derivative dI/dU of the current. dI/dU-spectroscopy is the mode most useful for determining the lifetime of excited states, because the spectra contain a measure for the lifetime as will be discussed in Chapter 4.2.

2.3.2 $z(U)$-spectroscopy

When ramping the voltage with active feedback loop, the tip will retract to keep the current constant. If the LDOS of the sample is constant except for some distinct, sharp features like surface states or quantum well states, the re-

sulting $z(U)$-curve is flat except for the positions of the features, where clearly visible step-like onsets appear, as sketched on the right side of Fig. 2.5.

It is possible to do dI/dU-spectroscopy while recording a $z(U)$-curve. In contrast to the dI/dU-spectroscopy described in the previous section, the feedback loop is active in this case, so the derivative of the current becomes

$$\frac{dI}{dU} \sim e\rho_S(E_F+eU)T(E_F+eU,U,z) - \frac{dz}{dU}\int_0^{eU} \rho_S(E_F+E)\kappa T(E_F+E,U,z)\,dE \quad (2.9)$$

where $\kappa = -2\sqrt{2m(\bar{\Phi} + \frac{eU}{2} - (E-E_{||}))/\hbar^2}$ (compare with (2.4)). The first term is the same as in (2.5), and is only a small background to the signal dominated by the second term: the dz/dU-term results in sharp, high peaks close to the position of the distinct features of the LDOS, sketched in Fig. 2.5.

The active feedback loop prevents the current to become very high or too low to be detected, as can happen in dI/dU-spectroscopy at constant height. Hence, large voltage ranges can easily be scanned, and the position of states can be identified.

2.3.3 $I(z)$-spectroscopy

Information about the tunneling barrier can be obtained using $I(z)$-spectroscopy, where the current I is recorded while varying the tip-sample distance z. Because of (2.4) and (2.5), the current depends exponentially on the distance: $I \propto \exp(-\kappa z)$, where $\kappa \propto \sqrt{\bar{\Phi}}$, where $\bar{\Phi}$ is the *apparent barrier height*. Simmons found that [24,25]

$$\bar{\Phi}/\mathrm{eV} = -0.952\left(\frac{d\ln I}{dz/\text{Å}}\right)^2. \quad (2.10)$$

In first order approximation, $\bar{\Phi} = (\Phi_T+\Phi_S)/2$, where Φ_T (Φ_S) is work function of the tip (sample). As Lang showed [25], the distance between tip and sample has a major effect on $\bar{\Phi}$ because the close proximity lowers the overall barrier height.

2.4 dI/dU-maps

A combination of the standard STM imaging mode and dI/dU-spectroscopy are dI/dU-maps. In this mode, additionally to acquiring constant-current or constant-height images, the dI/dU-signal, measured with a lock-in amplifier, is recorded. While the image is the integral of the density of states from 0 to the tunneling energy eU, the dI/dU-map selects the LDOS at eU, since $dI/dU \propto \rho(eU)$ [26–28].

An important usage of dI/dU-maps is to image standing wave patterns of scattered electrons at a certain energy. Avouris et al. calculated the LDOS for well defined scatterers [29]. For the LDOS of electrons scattered at a step edge

they found

$$\rho(E, x) \propto 1 - J_0(2k_{\parallel}x), \tag{2.11}$$

where J_0 is the zeroth-order Bessel function, $k_{\parallel}$ the wave vector of the electrons parallel to the surface, and x the distance to the step. Scattering at a point defect results in a LDOS distribution of

$$\rho(E, r) \propto 1 + \frac{2}{\pi k_{\parallel} r}\left[\cos^2\left(k_{\parallel}r - \frac{\pi}{4} + \eta_0\right) - \cos^2\left(k_{\parallel}r - \frac{\pi}{4}\right)\right], \tag{2.12}$$

where η_0 is a scattering phase shift depending on the scatterer, and r the distance from the scatterer. Using these equations, one can determine the wave vector for the energy at which the map was recorded. Recording maps at different voltages, the dispersion relation $E(k)$ can be determined [30,31].

A problem arising when acquiring dI/dU-maps in constant-current mode is that the tip–sample distance, and this changes the transmission coefficient (2.4). To correct for this, it has been proposed [30] to divide the dI/dU-map by $\exp(-z)$:

$$\rho_S(x, y, eU) \propto \frac{dI}{dU}(x, y, U) \cdot \frac{1}{\exp(-z(x, y, U))}, \tag{2.13}$$

where $z(x, y, U)$ is taken from the topography.

Chapter 3

Experimental

The experiments were carried out on a low-temperature, ultrahigh vacuum (UHV) STM designed by Jörg Kröger, which is described in this chapter. In Sec. 3.1, the original design is presented, followed by extensions made during this work: the controller for baking out the apparatus (Sec. 3.2), modifications of the STM for variable temperature ability (Sec. 3.3), and the damping of the helium cryostat (Sec. 3.4).

3.1 Overview

The apparatus is sketched in Fig. 3.1. It is divided into two main parts, a chamber for preparation of the samples and an analysis chamber which contains the STM. Additionally, there is a small fast-entry load lock for moving samples, tips and evaporators into the apparatus without breaking the UHV. The chambers are mounted on a framework consisting of aluminium rods. All three chambers are evacuated with turbomolecular pumps (*Pfeiffer Vacuum*, Asslar), preparation and analysis chamber have additional iongetter pumps (*Meca 2000*, France) and titanium sublimation pumps (*VACOM*, Jena). With this system, an ultrahigh vacuum (UHV) down to 10^{-8} Pa can easily be established. Since the turbomolecular pumps are mechanical pumps creating undesired vibrations, they can be separated from the preparation and analysis chambers with gate valves (*VAT*, Switzerland) and turned off. The vacuum is then maintained by the iongetter pumps.

For moving samples and equipment between the chambers, there are two magnetic motion drives (*Huntington*, USA) at the load lock and the preparation chamber. A third magnetic motion drive, mounted at the preparation chamber, is used for sample preparation. To each chamber a wobble stick (*Ferrovac*, Switzerland) is mounted to transfer UHV equipment in the chamber.

To damp vibrations of the building, the complete framework is supported by passive vibration isolation mounts (*Newport*, USA). In addition, the floor is cut around the apparatus so the floor it is standing on is has no direct contact to the building.

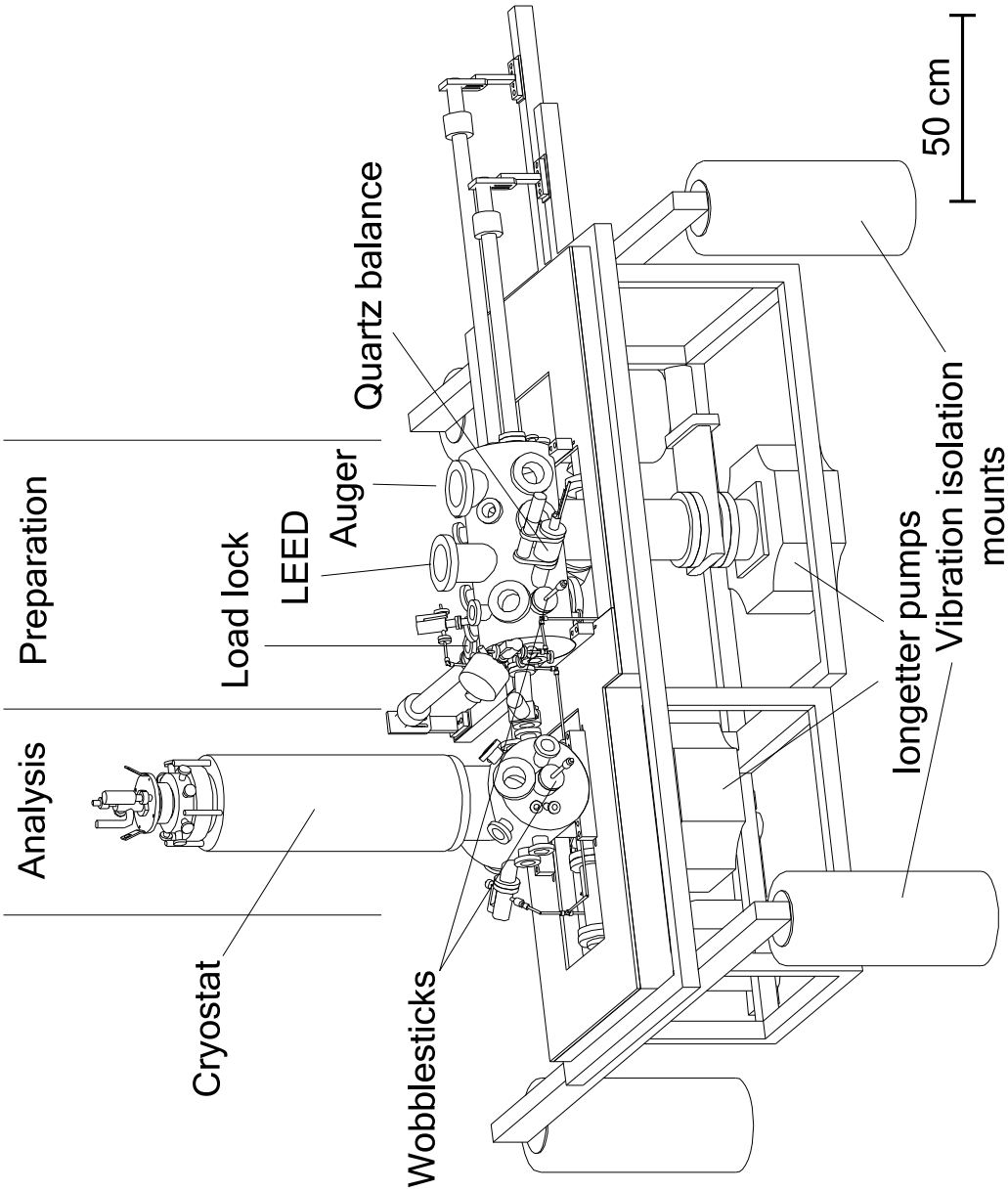

Figure 3.1: Overview of the apparatus.

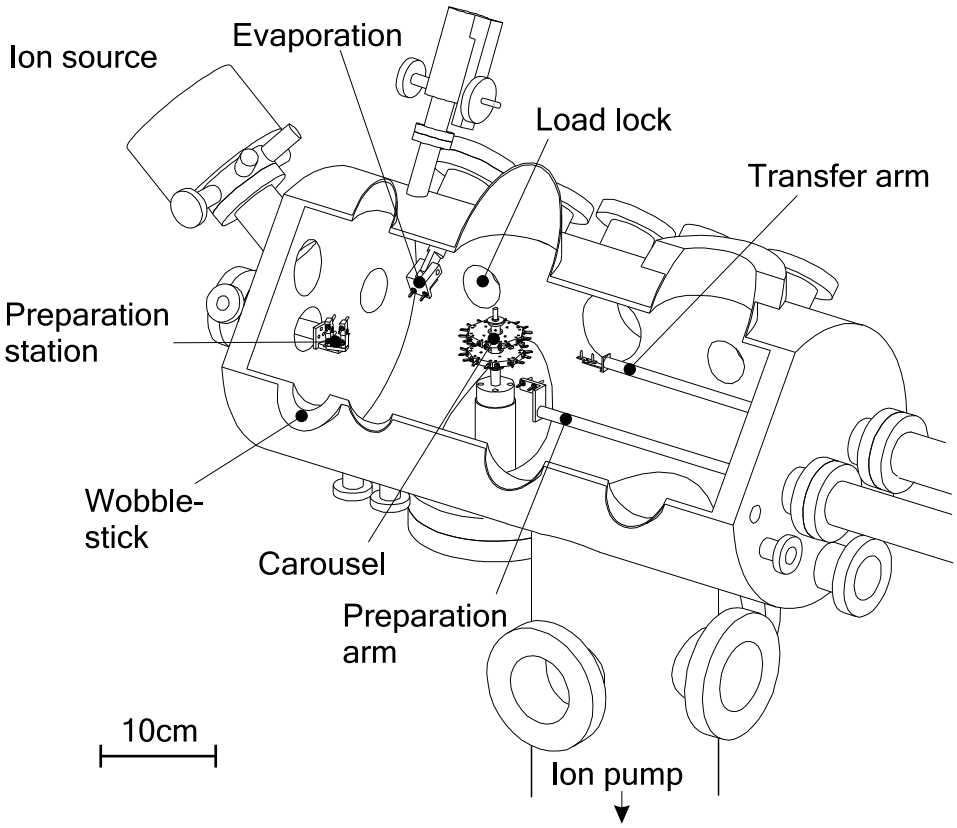

Figure 3.2: The preparation chamber.

The measurements were carried out with commercial electronics and software (*RHK*, USA). The tunneling current is converted to a voltage by an I/V-converter (*FEMTO*, Germany) with a variable conversion factor of 10^3 V/A to 10^9 V/A (low noise) resp. 10^{11} V/A (higher noise).

3.1.1 Preparation Chamber

The preparation chamber is used for storage and preparation of samples and UHV equipment. An interior view is shown in Fig. 3.2. The samples enter the preparation chamber from the load lock. To store samples and equipment, a two-storey carousel is used. Each storey can carry up to eight samples, evaporators or tips.

On the left, an ion source (*Omicron*, Taunusstein) is mounted to clean the sample surface or sharpen a tip by argon ion bombardment. The sample resp. the tip is set on the preparation arm for this. As a second step in the cleaning process, the sample can be heated by a coil from the back on the upper level of the preparation station. The lower level of the preparation station is used for cleaning freshly introduced tips from oxide.

After repeated cycles of the cleaning procedure, the cleanliness and crystalline

order of the surface can be checked using a Low Energy Electron Diffractometer (LEED, *Specs*, Berlin). Pictures of the LEED-images can be taken with a digital camera. Also, the surface can be checked for contaminations with an Auger-spectrometer (*STAIB*, Langenbach).

After cleaning the surface, adsorbates can be deposited using the evaporation stage above the load lock (alkali metals, indium, ...) or the fork of the load lock (molecules; due to the design of the molecule evaporator it can not be used on the evaporation station). A quartz balance (*Intellimetrics*, UK) is used for checking the rate of deposition. For depositing gases, such as CO_2, a leak valve is mounted above the evaporation station.

Also, a mass spectrometer (*Spectra*, UK) is mounted to the preparation chamber which can be used to look for leaks and residual gas analysis.

3.1.2 Analysis Chamber

The cryostat (*Cryovac*, Troisdorf), which is the mounted to the analysis chamber, consists of an outer cryostat for 15 ℓ liquid nitrogen, and an inner cryostat which can hold 4 ℓ of liquid helium or liquid nitrogen. Between these two cryostats, there is a shield that covers the inner cryostat completely. This shield is cooled by the evaporating gas from the inner cryostat and reaches about 20 K when cooling with liquid helium. This two-stage mechanism very effectively protects the inner cryostat from heat radiation, thus reducing coolant consumption.

Gold covered radiation shields mounted to the bottom of the cryostats form the experiment chamber containing the STM. Each shield consists of two parts (see Fig. 3.3): The shields are mounted to the bottom of the cryostat and closed at the bottom. Moving on a rail surrounding the bottom are the doors. They cover the openings left in the shields for manipulation in the STM and can be moved using the wobblestick.

The STM[1] itself is shown in Fig. 3.4. The sample is mounted on the slider which can be moved by the coarse piezos. The coarse piezos are glued on one end to the base plate and end in titanium rings on which slider is lying. By contracting or bending the coarse piezos, the slider can be moved forwards, backwards and to the sides. The tip is mounted on a segmented tube piezo scanner. By applying voltages up to 130 V to the segments of the scanner, the tip can be moved by some 100 nm in all directions.

Tip and sample can be changed in UHV using the wobblestick mounted to the analysis chamber.

On the top railing, which is supported by three rods, are two clamps which fix the cables for the piezos and scanning voltage and current. The rods end in eyes to attach to springs. The other ends of the springs are attached to the bottom of the inner cryostat so that the STM can be suspended in the experiment chamber. For manipulation and cooling of the sample, the complete STM can

[1] A detailed description of the STM can be found in [32].

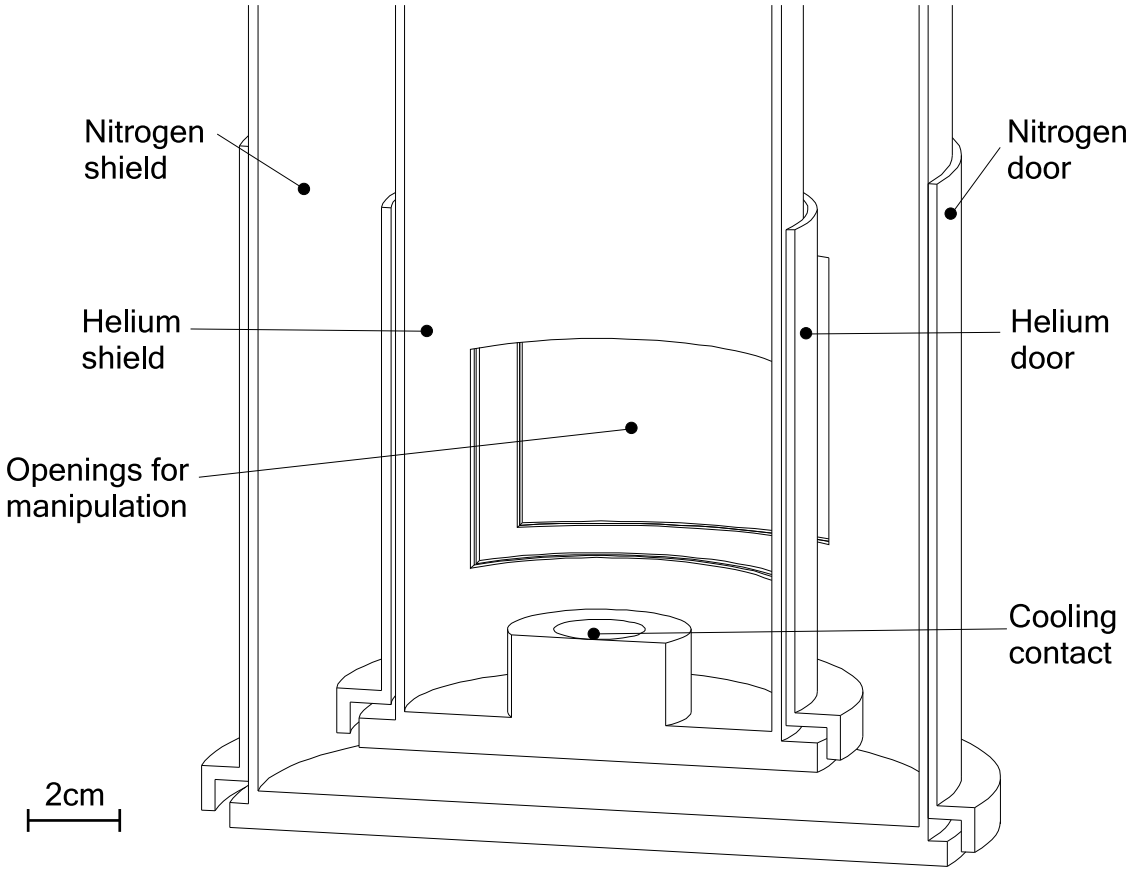

Figure 3.3: Helium and nitrogen shield at the bottom of the cryostats forming the experiment chamber.

be pressed into the cooling contact (see Fig. 3.3).

3.2 HEAT! — The Bake-out Controller

Introduction

For baking out the apparatus a computer based controller was built. It consists of a power supply by Jörg Neubauer which is capable of measuring temperatures of up to 24 temperature sensors and operating up to 18 heating tapes. The power supply does not control the tapes, it only transmits the temperature data to a computer and turns heating tapes on or off on demand from the computer. The reason for this separation is the bigger flexibility when programming a PC instead of a microcontroller. In this chapter, the main focus lies on the PC program, HEAT!.

Each heating tape can be associated with one or more temperature sensors.[2] Before the bake out is started, it is checked if all the sensors and tapes are

[2]The possibility to associate a tape with two or more sensors is not used anymore during

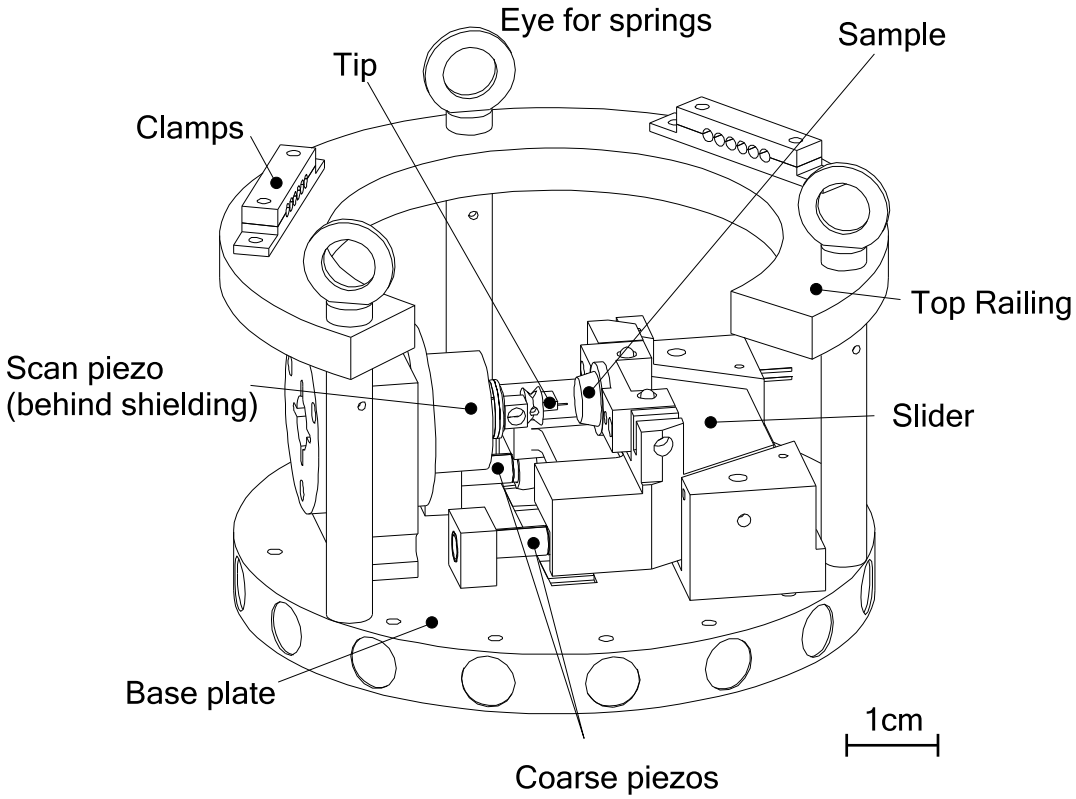

Figure 3.4: The STM.

connected correctly by heating a tape and looking which sensor measures an increase in temperature.

For every sensor, the desired temperature during bake out can be preset. The complete baking out consists of three parts: First, a slow heating up takes place, then the temperatures are controlled to be constant, and finally, slow cooling is processed.

In addition to the temperatures the pressures in the analysis and the preparation chamber are measured. This is used for logging only.

The control circuit

The central part of the control circuit is a PID-controller. For every sensor, it compares the currently measured temperature with the preset temperature and calculates three values:

Proportional part = difference of desired and current temperature

$$P = T^{\text{desired}}_{\text{this cycle}} - T^{\text{current}}_{\text{this cycle}}$$

The proportional part ensures a fast response to a deviation.

bake out.

Integral part = sum of all deviations

$$I = \sum_{i=0}^{\text{all cycles}} T^{\text{desired}}_{\text{cycle \#i}} - T^{\text{current}}_{\text{cycle \#i}}$$

If I is less than zero, it will be set $I = 0$.

The integral part acts in the long term and is necessary to reach and hold the desired temperature.

differential part = difference of the temperature in this cycle and the temperature of the last cycle

$$D = T^{\text{current}}_{\text{this cycle}} - T^{\text{current}}_{\text{last cycle}}$$

The differential part averts sudden changes in temperature.

The control signal is calculated by a weighted sum where the weighing of

$$CS = 200 \cdot P + 3 \cdot I + 500 \cdot D \tag{3.1}$$

for all sensors has proven to be a good choice. The control signal is restricted to values from 0 to 255. Since some tapes can be controlled by several sensors, a decent value has to be chosen that will be send to the tape. With this value, it is decided if a heating tape is actuated, taking care that the activation of a tape is evenly distributed in time. The periodicity of actuation is 0.5 s.

The main window

When starting the program, the main window (Fig. 3.5) appears. It contains the most important controls for the bake out. The menu bar (1)[3] allows access to the control functions like starting the bake out, and to a new window where all settings for the bake out can be adjusted.

The LED bar (2) shows if the designated tape is heating (LED is red) or not (LED is black). In the message line (3) information about the status of the bake out and error messages and warnings are shown.

During bake out, the pressures of the preparation chamber and the analysis chamber are plotted in the pressure graph (4), the current values are also shown in the digital pressure indicators (8), the temperatures are plotted in the temperature graph (5). The axes scales of the graphs are adjusted using the knobs (9) (pressure range) and (10) (time scale). The field (6) shows the status of the sensors: working sensors are shown in green, not working sensors in red, and sensors which are not used for the bake out are not shown.

There are two clocks (7): The Run Up Time shows the time passed since the program was started. The Remaining Time shows the time that is left for the current section of the bake out (checking of the assignment, heating up, bake

[3] The numbers in the following description refer to the numbers in Fig. 3.5 and Fig. 3.6.

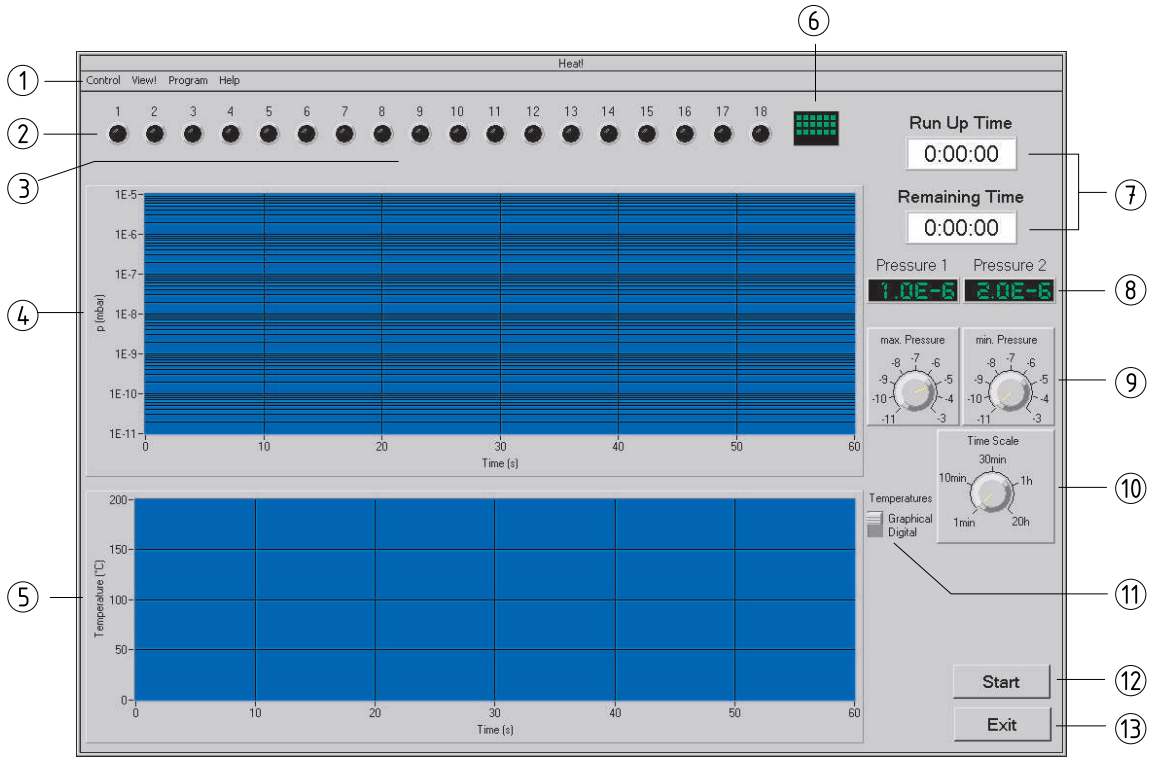

Figure 3.5: The main window of the bake out controller HEAT! on start-up, with graphical temperature display.

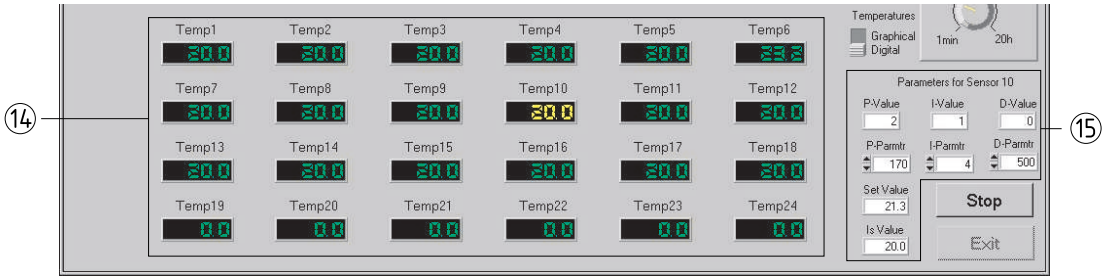

Figure 3.6: The lower part of the main window of the bake out controller HEAT! with digital temperature indicators.

out, cooling down). Button (12) starts and stops the bake out, and, when a minor problem occurred that could be adjusted, the bake out can be resumed. Button (13) ends the program. It is blocked during bake out.

With toggle (11) the display for the temperatures can be switched between graphical and digital, (14) in Fig. 3.6. By clicking on an indicator, the information (15) appear. They show the calculated P-, I-, and D-values, the parameters (which can also be changed) and the set value and the current value of the temperature.

3.3 Variable Temperature STM — The new Slider

Using the design described in Sec. 3.1, the sample can be examined at four different temperatures: room temperature, 80 K (cooling with liquid nitrogen), 60 K (cooling with frozen nitrogen) and 9 K (cooling with liquid helium). Sometimes it is desired to vary the temperature, for example to study temperature effects on surface diffusion [33, 34], on single molecule vibrations [35, 36], or on defect-induced perturbation [37]. To reach intermediate temperatures, one has to counter heat the sample or the whole STM. The heating can be done with a filament [38, 39], a button heater [40], a resistor [41], or using Zener-diodes [42]. In the last case, the diode is operated in reverse-biasing mode with voltages larger than the Zener voltage. The advantage of Zener diodes is that, since the Zener voltage can be some 10V, only a low current is needed to transport fairly high power. For this reason, heating with a Zener diode was chosen.

For choosing the right diode, several issues have to be taken into account. Heating the whole STM would require rather high power ($\approx$500 g of copper would have to be heated), and Zener diodes with high power would be too large for the existing design. Therefore, only the slider with the sample is heated. The diode is connected via steel cables to reduce heat transport. Steel is a bad electrical conductor, so the cables have a large resistivity, resulting in heating of the cables if the current is too high. Therefore, the current has to be low while maintaining a high power, that is at high voltages. And last, the diode has to be UHV compatible, plastic housings are out of question. A Zener diode fulfilling these requirements is the BZT03 which is about 4 mm long (without contacts), comes in a sintered glass case and with various Zener voltages up to 250 V and can stand up to 3 W. A diode with 68 V Zener voltage was chosen.

The modifications made to the slider are shown in Fig. 3.7. The diode is mounted in a small pit behind the pins supporting the sample. It is pressed into the pit by the cover. To avoid electrical contact, the walls of the pit are covered with capton foil. The cables are led out of the pit through a trench to the back of the slider; at the end of the trench, they are glued to the slider.

In the original design, the temperature sensor was mounted to the body of the STM. As only the slider is heated, the sensor is now mounted to it. This makes in total six copper cables leading to the slider (two for the diode, four for the sensor).

The heating of the slider has so far only been tested at the temperature of liquid nitrogen (77.6 K).[4] A typical temperature progression is shown in Fig. 3.8. The time-dependence of the temperature T during cooling showed to be

$$T(t) = (T_0 - T_M)e^{-t/\tau} + T_M, \tag{3.2}$$

with T_0 the temperature before cooling, $T_M = 77.6\,K$ the temperature of the

[4] For security reasons, a resistor of 1 kΩ was connected in series. With a maximum power of 1/8 W, this resistor can stand up to 11 mA – a value that the cables should easily withstand.

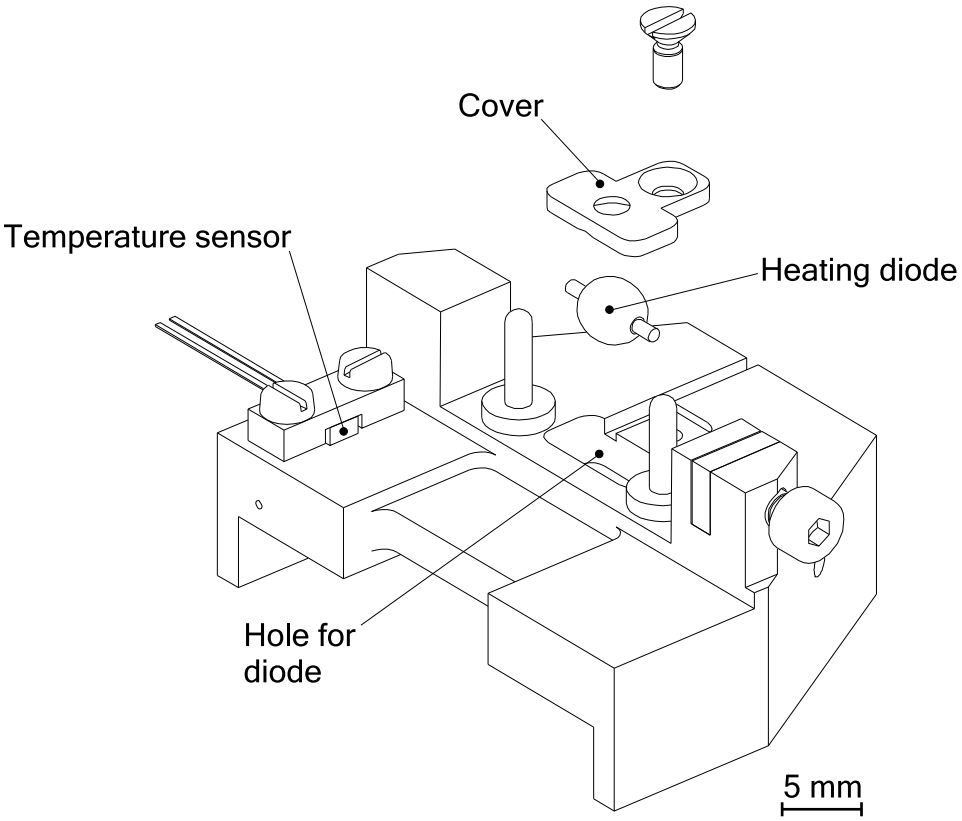

Figure 3.7: The modified slider

surrounding, $\tau = (177 \pm 7)$ min.

To calculate the cooling processes, the specific heat of copper was taken from the Debye model [43, 44] and calibrated to the room temperature value of 0.385 J/g·K [43]. In the range of 70 K to 120 K, it can be approximated by

$$c_V(T) = c_1(T - T_c)^2 + c_0, \tag{3.3}$$

with $c_1 = -2 \cdot 10^{-5}$ J/g·K^3, $c_0 = 0.3$ J/g·K, $T_c = 150$ K. Then, the change of energy, that is the power, is

$$\frac{dQ}{dt} = m \cdot c_V(T)\frac{dT}{dt}, \tag{3.4}$$

with $m = 42$ g the mass of the slider. Using (3.2), the emitted power P at a given temperature is

$$P(T) = -\frac{m}{\tau}\left\{c_1(T - T_c)^2 + c_0\right\}(T - T_M). \tag{3.5}$$

This is the power that has to be brought into the slider by adjusting the current through the diode to keep the temperature T constant. The comparison of experiment and calculation is shown in Fig. 3.9. As can be seen, the agreement is very good.

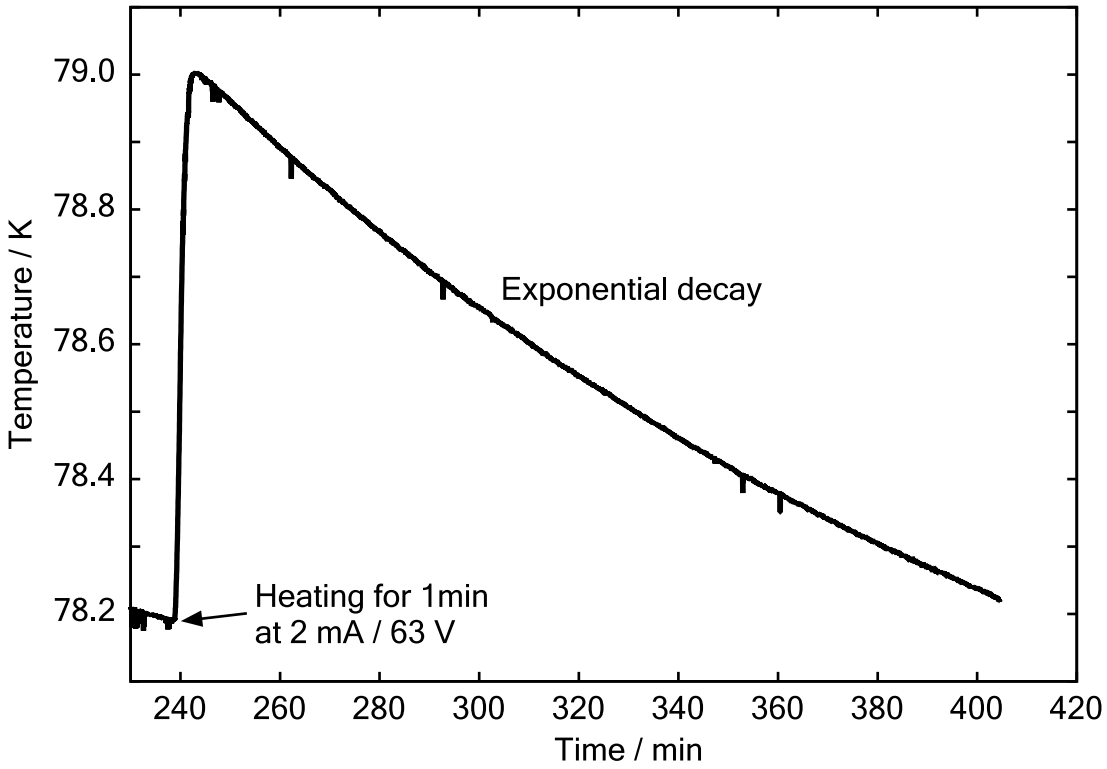

Figure 3.8: Temperature progression after heating for 1 min at 2 mA, 63 V. The decay is exponential with a time constant of 190 min. The spikes in the curve are due to spikes in the voltage measuring of the sensor.

The voltage at the diode happens to differ from 68 V, starting at around 57 V for low currents, going up to 82 V for higher currents. This is behavior is due to the temperature dependence of the avalanche process in the diode leading to the reverse-bias conductance. It is well known that this process takes place at higher voltages when the temperature is higher [45]. Therefore, the diode is conductive at lower voltages when it is cold, and the breakdown voltage increases as the diode warms up.

To theoretically derive the decay rate τ in (3.2), three different cooling processes have to be considered:

1. **Heat radiation.**
   The power P emitted by radiation is [46, 47]

   $$P_1 = \sigma\varepsilon F(T^4 - T_M^4) = -\frac{dQ}{dt},$$

   with $\sigma = 5.671 \cdot 10^{-8}\,\mathrm{W/(m^2K^4)}$ the Stefan-Boltzman constant, ε the emission coefficient of the surface, $F = 29\,\mathrm{cm}^2$ the surface area of the slider. Using the approximation (3.4), one gets approximately for the temperature range of 80 K to 120 K

   $$T = (T_0 - T_M)e^{-t/\tau_1} + T_M, \qquad \tau_1 = 1.1 \cdot 10^{-7}\,\mathrm{J/g} \cdot \frac{m}{\sigma\varepsilon F} = 7.7\,\mathrm{h}/\varepsilon.$$

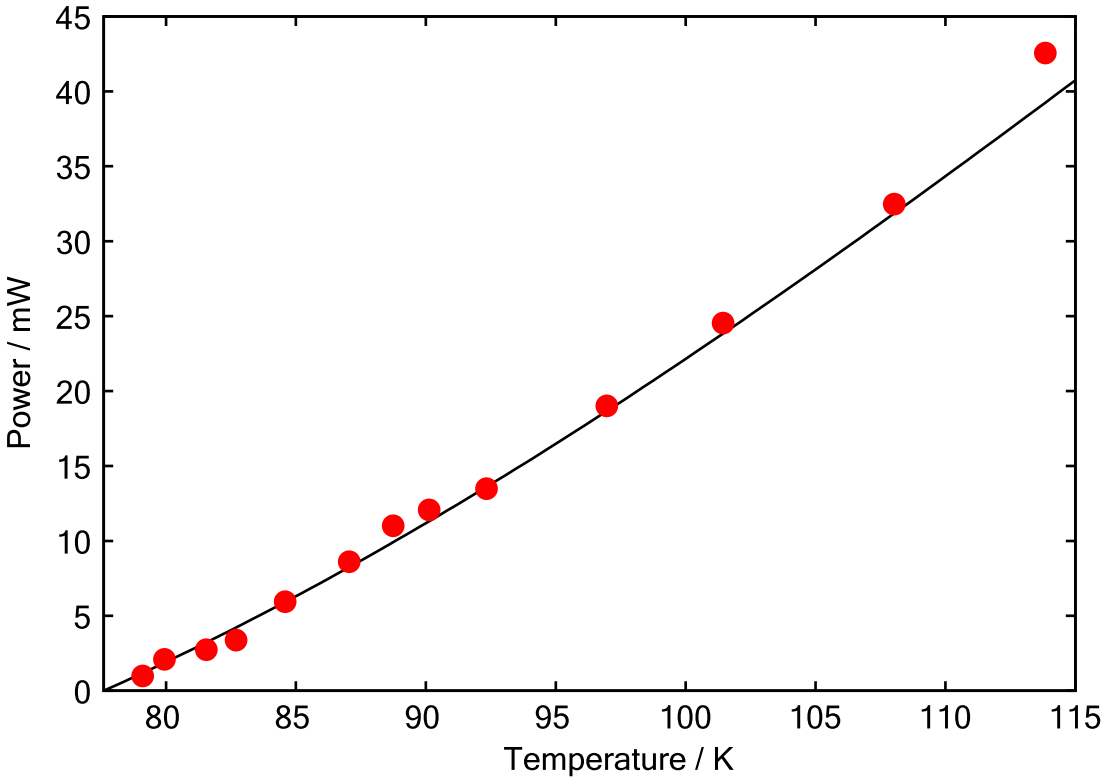

Figure 3.9: Power needed to get a stable temperature. circles: measurements; line: calculation (see Eq. (3.5))

ε is unknown, but will used as a fitting parameter later on.

2. **Heat transport through cables.**
The power P transported through a solid such as a cable or a rod with its ends at temperatures T_1 and T_2 is given by [47]

$$P_2 = \bar{\lambda} \cdot (T_1 - T_2) \frac{A}{\ell},$$

with A the cross section of the cable, ℓ its length and $\bar{\lambda}$ the integrated heat conductivity

$$\bar{\lambda} = \frac{1}{T_1 - T_2} \int_{T_1}^{T_2} \lambda(T)\, dT,$$

where λ is the temperature-dependent heat conductivity.

The six cables going to the slider have a diameter of 0.1 mm, that is $A = 7.9 \cdot 10^{-3}\,mm^2$ and the length $\ell \approx 10\,cm$, the heat conductivity of copper is taken from [48]. Using (3.4), one gets

$$\begin{aligned} -\frac{6A}{\ell \cdot m}\, dt &= \frac{c_1 (T - T_c)^2 + c_0}{(T - T_M) \cdot \bar{\lambda}}\, dT \\ &\approx \frac{c_3}{T - T_M}\, dT, \qquad c_3 = 0.53 \frac{mm \cdot s}{g}, \end{aligned}$$

giving

$$T = (T_0 - T_M)e^{-t/\tau_2} + T_M, \qquad \tau_2 = \frac{\ell \cdot m \cdot c_3}{6A} = 13\,\mathrm{h}.$$

3. **Heat transport through supporting titanium rings.**
   Although in principle the calculation for the titanium rings is the same as for the cables, it is much more demanding because of the varying heat transporting cross-sectional area of the rings. Furthermore, the heat transport from the slider to the rings cannot be modelled because data for the heat transport from sapphire to titanium and the supporting area are missing. To get an estimate of the process, the rings will be modelled as rods with the minimum cross section of the rings and taking the radius as their length. The varying cross section and the heat transport from sapphire to titanium are taken into account by a factor f. A value for it will be estimated from the experimental values shown in Fig. 3.9. Then, following the calculation described above with $A_R = 3.2\,\mathrm{mm}^2$, $\ell_R = 5\,\mathrm{mm}$ and taking λ_{Ti} from [48], one gets ($c_4 = 6\,\mathrm{mm{\cdot}s/g}$)

   $$T = (T_0 - T_M)e^{-t/\tau_3} + T_M, \qquad \tau_3 = \frac{\ell_R \cdot m \cdot c_4}{3A_R \cdot f} = 131\,\mathrm{s/f},$$

   where f is a factor that sums up the inhibited heat transport from the slider to the rings. f cannot be modelled, but will be used a fitting parameter in the following.

The decay rate of all three processes combined gives

$$\tau = \left(\frac{1}{\tau_1} + \frac{1}{\tau_2} + \frac{1}{\tau_3}\right)^{-1}. \tag{3.6}$$

There are still two unknown variables: ε from the heat radiation and f from the heat transport through the titanium rings. Their values can be determined by fitting the resulting power loss to the experimental data shown in Fig. 3.9 under the condition that the decay rate τ from (3.6) equals 177 min, as obtained from the evaluation of the temperature decay curves. The result is $\varepsilon = 1.9$, $f = 0.003$. The small value of f reflects small heat transport from the slider to the rings and a small supporting area of the slider on the rings. $\varepsilon > 1$ suggests that the surface of the slider is (microscopically) larger than used in the calculation. This can be explained by the fact that the slider has not been polished, i.e. that the surface is rough to some amount.

Now the power loss can be calculated for a larger temperature range and different ambient temperatures. The result is shown in Fig. 3.10. As is to be expected, the power rises strongly the larger the temperature difference due to heat radiation. At ambient temperatures of 55 K and 78 K, the heat transport through the cables and the rings does not play an important role, whereas at 9 K, where copper has its maximum in heat conductivity of 24 kW/(m·K) compared with 400 W/(m·K) at room temperature, the cables can transport a large

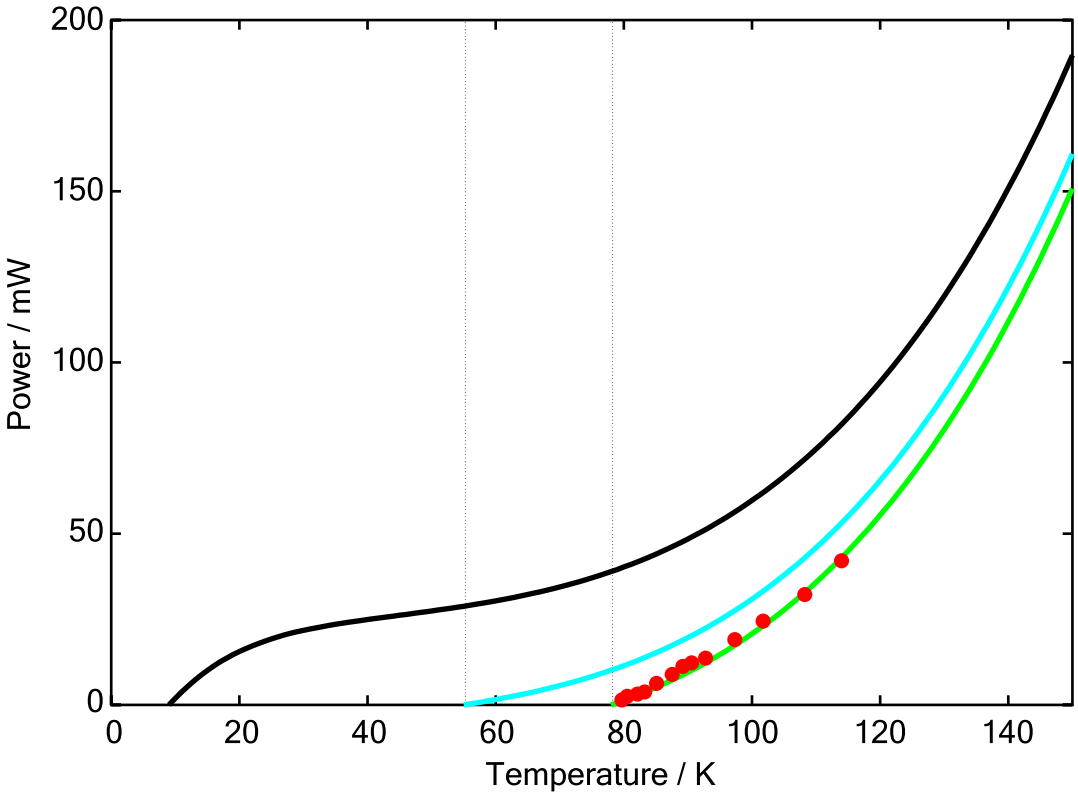

Figure 3.10: Result of numerical calculations for the powers needed to keep the temperature of the slider constant for different ambient temperatures. Black: T_M=9 K; blue: T_M=55 K; green: T_M=78 K; circles: measurements as shown in Fig. 3.9. The strong increase at the beginning of the curve for T_M=9 K is due to the large heat conductivity of copper at 9 K.

amount of energy, showing in the fast increase of the power at low temperature.

It should be mentioned that this calculation can only be considered a rough estimate as it is an extrapolation from the temperature range of 80 K to 120 K to the range of 9 K to 150 K.

3.4 Damping the Cryostat

Although the complete apparatus is vibration isolated by the vibration isolation mounts, and the STM is suspended on springs, there are still some vibrations reaching the STM. For this reason, an additional damping of the helium cryostat was built.

The design of the damping system, shown in Fig. 3.11, was inspired by the design at another STM in our group [49]. To the plate above the bellow, which is connected to the helium cryostat, a supporting plate with three arms is mounted. For security reasons, the plates are screwed together. The arms

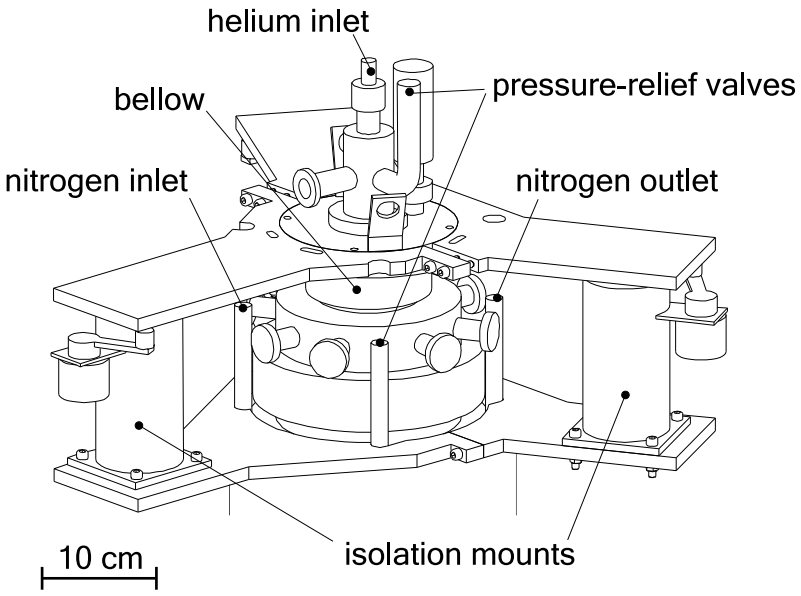

Figure 3.11: Assembly for damping the cryostat.

are sustained by vibration isolation mounts standing on the lower supporting plate which lies on the top of the nitrogen dewar.

The three vibration isolation mounts are from *Kinetic Systems, Inc.*, Boston, USA, model no. 1206-200-12, and have been chosen because they fit perfectly between the supporting plates. Their natural frequencies are 1.5 Hz (vertical) and 2.1 Hz (horizontal) at the maximum load of $5.5 \cdot 10^5$ Pa [50]. Above these frequencies, the isolation performance increases dramatically, depending on the load.

To determine the effect of the vibration isolation, the acceleration of the top plate due to vibration was measured once with the plate fixed and once with the vibration isolation system active, where the vibration isolation mounts are actuated with a load of $3 \cdot 10^5$ Pa. In both cases the turbo pumps at the preparation chamber and at the load lock were turned on. The result is shown in Fig. 3.12, where the amplitude of the acceleration is given in mg, g being the gravitational acceleration. The upper panel shows the vibrational spectrum on the top plate of the helium dewar with the plate fixed. The peak at 1500 Hz is due to the turbo pump at the load lock, the peak at 1000 Hz results from the turbo pump at the preparation chamber. Comparing this frequency spectrum with that one of the damped dewar (lower panels), one sees its large effect: The three highest peaks at 190 Hz, 380 Hz and 1500 Hz are damped by about 85%, the smaller peaks between 500 Hz and 2000 Hz vanish completely. The only exception is the peak at 1000 Hz originating from the the turbo pump at the preparation chamber. The vibration isolation is not as effective as specified by the manufacturer [50], because the inner cryostat is not mechanically disconnected from the outer cryostat: The two parts are connected by the bellow which can transmit vibrations. However, this is a soft coupling which does not

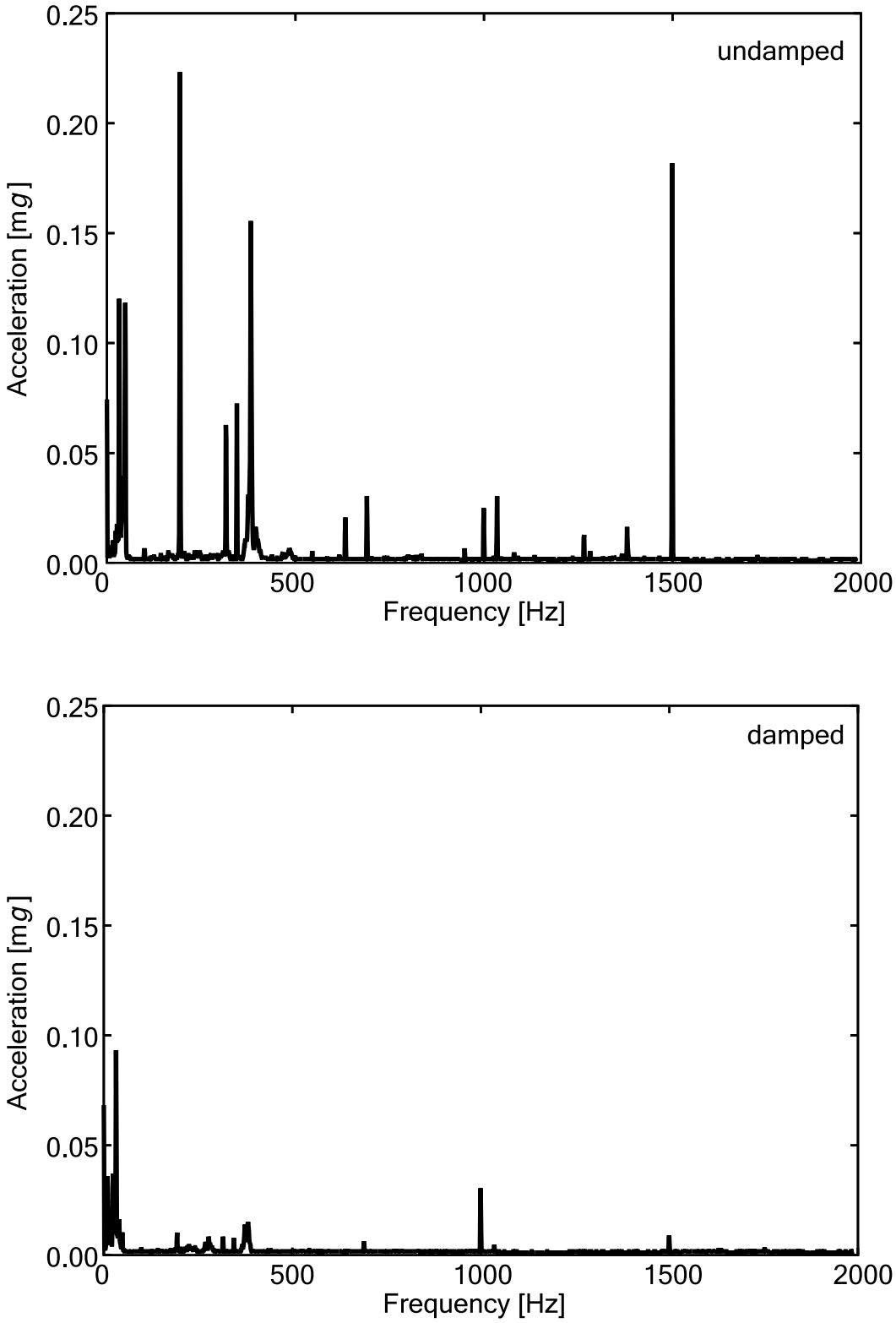

Figure 3.12: Frequencies measured on the undamped (upper panel) and damped cryostat (lower panel). All the large peaks are effectively damped.

transmit the vibration as effectively as the stiff coupling when the cryostat is fixed.

Together with the new isolation stage, there are five stages isolating the STM from vibrations:

1. The floor is cut around the apparatus to block vibrations of the building.
2. The vibration isolation carrying the supporting frame.
3. The vibration isolation of helium cryostat.
4. The springs on which the STM is hanging prevent vibrations of the helium cryostat from reaching the STM.
5. The eddy-current damping at the bottom of the STM deadens swinging of the STM at low frequencies. This stage isolates vibrations which the isolation mounts cannot isolate.

Chapter 4

Lifetimes of Electronic Excitations

When describing the electronic structure in crystalline bulk material, the crystal is assumed to be infinite, or, for simpler calculations, periodic. With these assumptions, all atom positions are equivalent, and the electron wave functions are periodic as well [43, 51]. This will change when a surface is taken into account, where the symmetry is broken and the atom positions are not equivalent any more. In this case, additional states appear which are localized at or near the surface [52, 53]. Of fundamental interest in surface science and nano technology is the lifetime of these states, because it determines the range of interaction of electrons in the states, can be determined easily by experiments, and gives profound information about interactions between electrons, phonons and adsorbates.

Different types of states localized at the surface are presented in Section 4.1, Section 4.2 discusses mechanisms which influence the lifetime of excited surface localized states.

4.1 Types of states localized at the surface

4.1.1 Surface states

Surface states were first predicted by Igor Tamm in 1932 [54, 55]. In 1939, William Shockley used another approach leading to surface states [56]. The easiest way to explain the existence of surface states is via the one-dimensional band theory [53, 57]:

The periodically ordered atoms in the bulk lead to a periodic potential. For simplicity, it can be modelled by

$$V(z) = -V_0 + 2V_g \cos(g \cdot z) \tag{4.1}$$

with V_0 the vacuum barrier, $V_g < 0$ the atomic corrugation potential and $g = 2\pi/a$ the reciprocal lattice vector, where a is the lattice constant of the

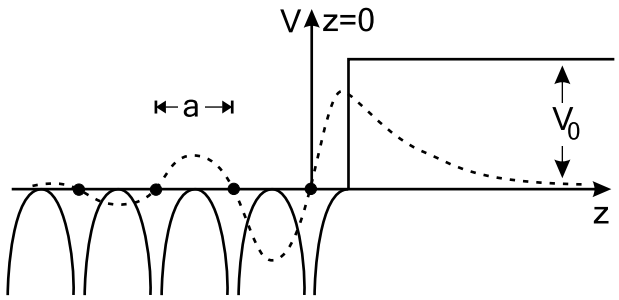

Figure 4.1: Localization of the surface state. The atoms (black dots) create a periodic potential (solid lines). The wave function of an electron is also periodic. While the function is undamped in an infinite bulk, damping is possible from the surface into the bulk. Since the wave function decays exponentially in the vacuum, the state is localized at the surface. (Since the surface atom is located at $z = 0$, the vacuum barrier starts at $z = a/2$.) (Adapted from [53].)

crystal (see Fig. 4.1). Notice that the potential depends only on the direction perpendicular to the surface z. This simplification can be done since we are interested in the effect on the wave function in z-direction, only. The solution of the Schrödinger equation, which reduces to

$$\left[-\frac{\hbar^2}{2m}\frac{d^2}{dz^2} + V(z)\right]\psi(z) = E\psi(z) \tag{4.2}$$

($\hbar$: Planck's constant divided by 2π, m: mass of the electron) has equally to be periodic. It can easily be shown that

$$\psi(z) = e^{i\kappa z}\cos\left(\frac{gz}{2} + \delta\right), \tag{4.3}$$

where $\sin(2\delta) = \hbar^2(2m)^{-1} \cdot \kappa g/V_g$, with the energies

$$E = -V_0 + \frac{\hbar^2}{2m}\left(\left(\frac{g}{2}\right)^2 + \kappa^2\right) \pm \sqrt{\left(\frac{\hbar^2 g\kappa}{2m}\right)^2 + V_g^2} \tag{4.4}$$

is a solution. From (4.4) can be directly seen that there is an energy gap of $2V_g$ for κ^2 negative, *i.e.* imaginary κ. However, an imaginary κ is not possible in the bulk: While the wave function goes to zero in one direction, the exponential term in (4.3) causes the wave function to diverge in the other direction. At surfaces, on the other hand, an imaginary κ is allowed: The amplitude of the oscillations of the wave function decays exponentially into the bulk; in the vacuum, the wave function is described by an exponential decay, so in total the wave function is

$$\begin{aligned} \psi(z) &= e^{\kappa' z}\cos\left(\tfrac{gz}{2} + \delta\right) && z < a/2 \\ \psi(z) &= e^{-qz} && z > a/2 \end{aligned} \tag{4.5}$$

with a the atomic distance (the surface atom is located at $z = 0$, the vacuum barrier starts therefore at $z = a/2$), $\kappa' = i\kappa$ and $q^2 = V_0 - E$, where κ has to

be chosen as to make the wave function continuous. The resulting function is sketched in Fig. 4.1. This state that lies in the projected bulk energy gap and is located at the surface, is called *Shockley* state.

Another approach for surface states that is more appropriate for semiconductor surfaces, uses the tight-binding-approach [52]:

The bulk potential V_L is modelled by a linear combination of atomic potentials V_a,

$$V_L = \sum_{n=1}^{N} V_a(\vec{r} - n\vec{a}), \tag{4.6}$$

where the Schrödinger equation of a single atom is solved by the (atomic) wave function φ,

$$\left[-\frac{\hbar^2}{2m}\nabla^2 + V_a(\vec{r})\right]\varphi(\vec{r}) = E_a\varphi(\vec{r}). \tag{4.7}$$

An ansatz for solving the Schrödinger equation of the bulk,

$$\left[-\frac{\hbar^2}{2m}\nabla^2 + V_a(\vec{r}) + [V_L(\vec{r}) - V_a(\vec{r})]\right]\Psi(\vec{r}) = E_L\Psi(\vec{r}), \tag{4.8}$$

is the linear combination of atomic wave functions:

$$\Psi(\vec{r}) = \sum_{n=1}^{N} c_n\varphi(\vec{r} - n\vec{a}). \tag{4.9}$$

When substituting (4.9) in (4.8), only on-site matrix elements α and nearest-neighbor interactions β are taken into account:

$$\langle l|\, V_L - V_a\,|m\rangle = -\alpha\delta_{l,m} - \beta\delta_{l,m\pm1}. \tag{4.10}$$

The result is a recursion relation for c_n:

$$c_n(E - E_a + \alpha) + (c_{n-1} + c_{n+1})\beta = 0, \tag{4.11}$$

which can be solved by $c_n = Ae^{ink a} + Be^{-ink a}$, giving the energies

$$E = E_a - \alpha + 2\beta\cos ka. \tag{4.12}$$

However, (4.11) is only true for all sites when using an infinite crystal (or periodic boundary conditions). At surfaces, where the periodicity is broken, the on-site matrix elements α have to be replaced by α'. Furthermore, c_n for the surface atoms (i.e. $n = 1$ and $n = N$) satisfy

$$\begin{aligned} c_1(E - E_a + \alpha') + c_2\beta &= 0, \\ c_N(E - E_a + \alpha') + c_{N-1}\beta &= 0. \end{aligned} \tag{4.13}$$

When solving (4.11) with these boundary conditions, one gets a transcendental equation with N roots for k. Most of them lead to waves with atomic periodicity. When

$$|\alpha' - \alpha| > |\beta|, \tag{4.14}$$

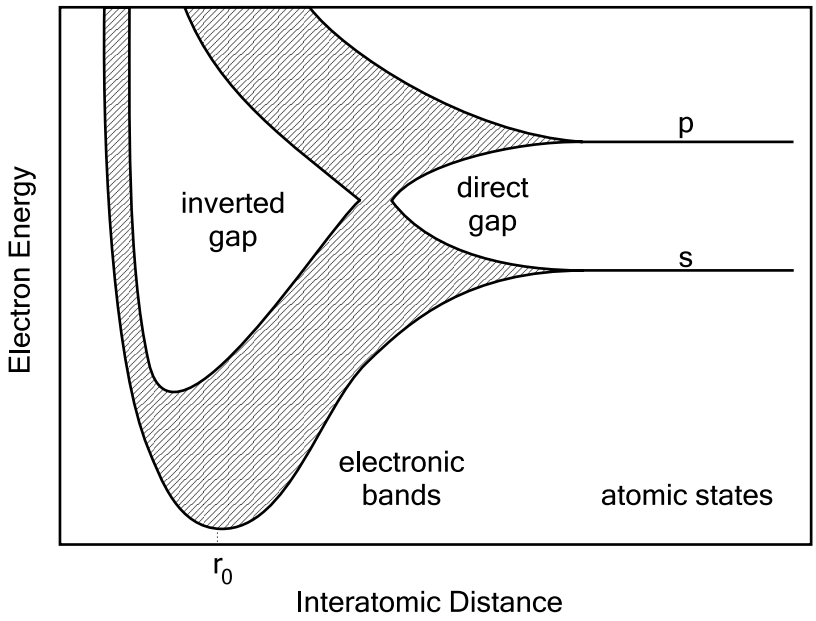

Figure 4.2: When atoms move together forming a solid, the atomic levels broaden to form energy bands. Eventually, these bands cross, forming hybrids. Band gaps occurring without a crossing of bands are called *direct band gaps*. Their upper bound is given be the p state, the lower bound by the s state. Band gaps occurring after a crossing of bands are called *inverted band gaps*, because the p state now defines the lower bound of the gap and the s state the upper bound – the states thus changed places. Surface states located in a direct band gap are of the Tamm-type, surface states located in an inverted band gap are of the Shockley-type. (Adapted from [60].)

two of the roots become complex, and the corresponding wave functions decay from the surface into the bulk. These states are therefore localized at the surface.

(4.14) reflects the amplitude of perturbation at the surface. Surface states of this type, which are called *Tamm* states, only occur when a strong perturbation takes place at the surface.

The distinction between Shockley and Tamm states is often unclear [58], a useful argument takes a look at the electronic band structure [56, 59]: The formation of electronic bands is often visualized by splitting of atomic energy levels when the atoms approach each other [43,51,56] as is sketched in Fig. 4.2. Eventually, bands originating from different atomic levels (s and p levels in Fig. 4.2) cross each other, and instead of overlapping, a band gap forms where the lower boundary is formed by the p band, while the upper limit is formed by the s band. Since in the atom, the s level is lower than the p level, such a band gap is called *inverted*. The band gap of the (111) surfaces of noble metals are of this kind. A band gap without a crossing is called *direct* [59]. The distinction of surface states now is as follows: Shockley states are located in inverted band gaps, Tamm states are located in direct band gaps.

4.1.2 Image potential states

The surface states discussed in the previous section are due to a break in the periodic potential of the bulk. Another type of surface localized states, the image potential states, has its origin in processes above the surface:

When an electron approaches a metallic surface, it induces an image charge in the bulk near the surface [61]. This image charge produces a Coulomb-potential outside the crystal:

$$V(z) = V_0 - \frac{1}{4\pi\varepsilon_0}\frac{e^2}{z}, \tag{4.15}$$

where V_0 is the vacuum barrier, e is the electron charge, ε_0 the vacuum permittivity, and z the distance of the electron from the surface. In 1978, P. Echenique and J. Pendry showed that this potential causes a Rydberg-like series of states above the surface [62]. The energies of these *image-potential states*, lying between the Fermi energy and the vacuum level in a surface band gap, have much in common with the energy levels in a hydrogen atom, yet the theoretical description is more difficult:

Since the divergence $V(z) \to \infty$ at the surface is physically unsatisfactory [63], the Coulomb potential is cut off at some distance z_{im} above the surface, and in the range between the cut-off and the surface continued appropriately:

$$V(z) = \begin{cases} V_0 - \frac{1}{4\pi\varepsilon_0}\frac{e^2}{z - z_0} & z > z_{im} \\ V_{cont}(z) & 0 < z < z_{im} \end{cases} \tag{4.16}$$

where z_0 denotes the image plane.Several continuations V_{cont} have been proposed [63–65], for example the truncation, where V_{cont} is set constant,

$$V_{cont} = V_0 - \frac{1}{4\pi\varepsilon_0}\frac{e^2}{z_{im} - z_0}, \tag{4.17}$$

or the linear continuation

$$V_{cont} = (\ell_1 \cdot z + \ell_2), \tag{4.18}$$

where ℓ_1 and ℓ_2 are chosen such as to make the resulting potential continuous differential. These two continuations are sketched in Fig. 4.3. However, the exact form is not important for a qualitative understanding.

The Schrödinger equation for the image potential, $z > z_{im}$, is

$$-\frac{\hbar^2}{2m}\frac{d^2\psi}{dz^2} + \left(V_0 - E - \frac{1}{4\pi\varepsilon_0}\frac{e}{z - z_0}\right)\psi = 0. \tag{4.19}$$

By substituting

$$E = V_0 - \frac{\hbar^2}{2ma_0^2\alpha^2}, \qquad \xi = \frac{2(z - z_0)}{\alpha a_0} \qquad \text{with } a_0 = \frac{4\pi\varepsilon_0\hbar^2}{me^2} \text{ the Bohr radius} \tag{4.20}$$

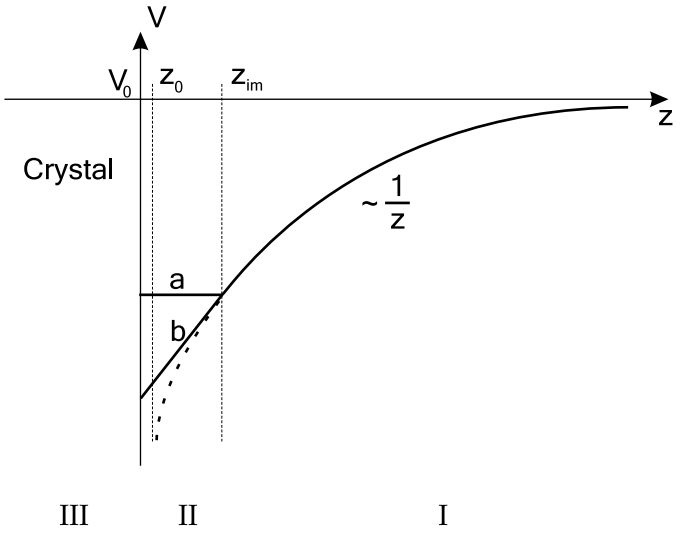

Figure 4.3: The image potential is divided in three areas: I: Coulombic potential due to the image charge. II: A cut-off of the image potential to avoid the divergence at the surface; a) truncation, b) linear continuation of the potential. III: Inside the crystal as discussed in Sec. 4.1.1.

and α a real number, (4.19) transforms to [52]

$$\frac{d^2\psi}{d\xi^2} - \frac{1}{4}\psi + \frac{\alpha}{\xi}\psi = 0, \tag{4.21}$$

whose solutions are the Whittaker functions [66], which are confluent hypergeometric functions.

From the substitution for the energy in (4.20) one can see that the series of energy states will be Rydberg-like, $E - V_0 \sim 1/\alpha^2$, but the deviation of the potential from the image potential for $z < z_{im}$ will lead to non-integral quantum numbers. It is convenient to define the *quantum defect* of a level as the difference between the integer quantum number n and the value α [67]:

$$\delta_n = \alpha - n \tag{4.22}$$

Inside the crystal, the situation is the same as discussed in Sec. 4.1.1 for surface states, the wave function is therefore given by (4.3).

By combining the wave functions of the different areas using the standard matching conditions, one gets the energy distribution

$$E_n = V_0 - \frac{E_1}{(n + \delta n)^2}, \tag{4.23}$$

where E_1 and δn result from the matching.

Since the wave function takes the form of the surface state inside the crystal, surface states and image potential states are strongly related, the surface state

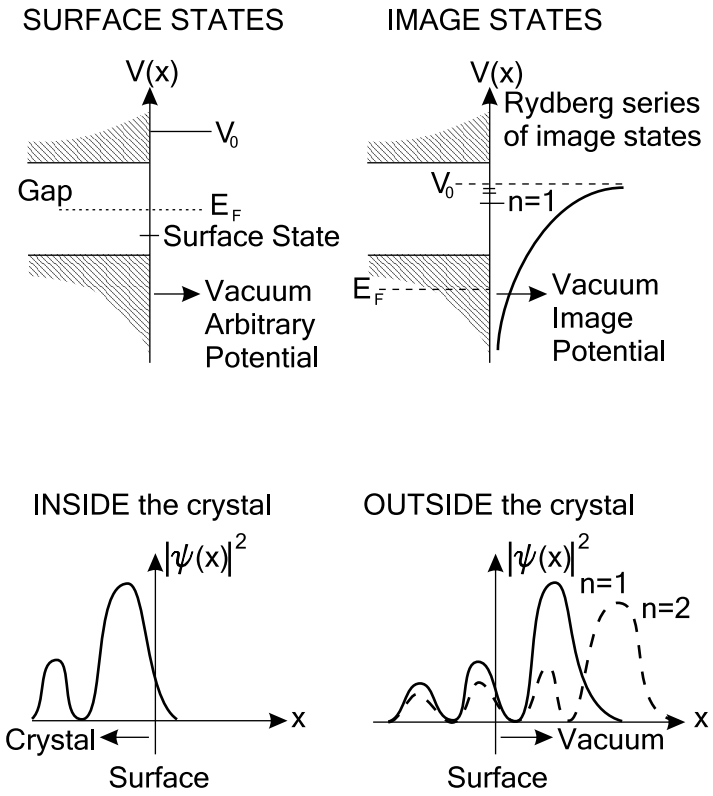

Figure 4.4: Comparison between surface states and image potential states. (Adapted from [52].)

is sometimes denoted as the zeroth image potential state [65], although $n = 0$ is not a valid choice for the image potential state.

Fig. 4.4 shows the similarities and the differences between surface states and image potential states: Both states lie in the surface band gap, but while for the surface state the vacuum potential is arbitrary, the image potential states form only in the image potential. There is only one surface state, but a series of image potential states whose energy approaches the vacuum energy with increasing state index. The surface state is localized *inside* the crystal, while the image potential states are localized *outside* the crystal, with the maximum of probability moving away from the surface with increasing state index.

4.1.3 Field-emission resonances

An process closely related to image potential states is the field emission. When a voltage is applied between the surface and an electrode (for example the tip), the Coulombic potential is extended linearly above the vacuum level, i.e. it does not approximate the vacuum level anymore but increases linearly to the electrode. For simplicity, the Coulombic part of the potential is neglected in the following discussion, but it has to be kept in mind that the states discussed in this section are basically image potential states in an extended potential.

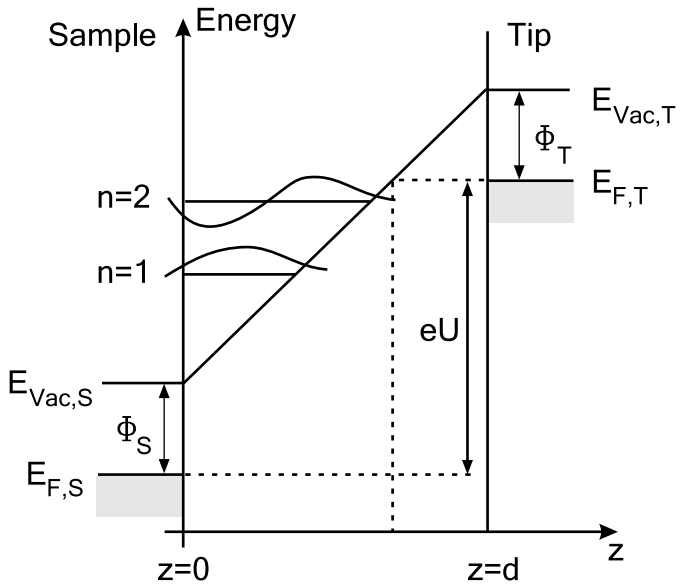

Figure 4.5: Energy diagram between tip and sample. The sample surface is located at $z = 0$, the tip surface is at $z = d$. The Fermi level $E_{F,T}$ of the tip is displaced from the Fermi level $E_{F,S}$ of the sample by eU, where e is the electron charge and U the applied voltage. Φ_S and Φ_T are the work function of the sample and tip, respectively. When $eU > \Phi_S$, the shown potential curve results. In this triangular potential so called field emission resonance states, labelled as $n = 1$ and $n = 2$, appear. (Adapted from [68].)

If the voltage applied between tip and sample during a tunneling experiment is larger than the work function Φ_S of the sample, the predominant process is not tunneling anymore but field emission, because the energy of the electrons is large enough to leave the bulk. The field induces a triangular potential well between tip and sample. This variable-size box hosts so-called *field emission resonance states*, as depicted in Fig. 4.5. The energy positions of the states are obtained by solving the Schrödinger equation, which for the area between tip and sample is [52]

$$-\frac{\hbar^2}{2m}\frac{d^2\psi}{dz^2} + (\Phi_S + F \cdot z - E)\,\psi = 0, \tag{4.24}$$

where $F = eU/d$ represents the electrical field, d being the distance between tip and sample. By substituting $\xi = \sqrt[3]{2m/(\hbar^2 F^2)} \cdot (\Phi_S + F \cdot z - E)$, (4.24) becomes

$$\frac{d^2\psi}{d\xi^2} - \xi\psi = 0, \tag{4.25}$$

the Airy-equation. The solution of (4.25) is the Airy-function[1]

$$\mathrm{Ai}(x) = \frac{1}{\pi}\int_0^\infty \cos\left(\frac{t^3}{3} + xt\right)\,dt \tag{4.26}$$

[1]Since (4.25) is a differential equation of second order, there is a second solution Bi(x), but this function diverges for $x \to \infty$ and is therefore omitted.

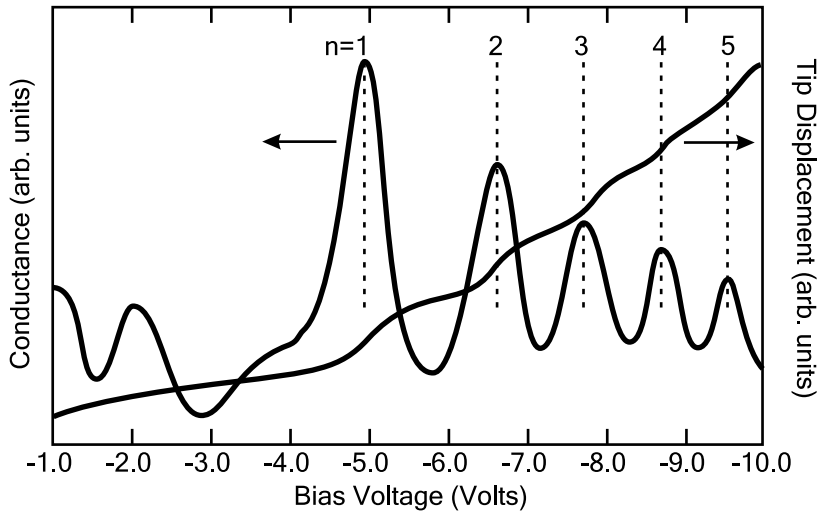

Figure 4.6: Field emission resonances of Si(111)-$(2\sqrt{3} \times 2\sqrt{3})$Sn detected by $z(U)$-spectroscopy, adapted from [70]. The features at voltages larger than 5.0 V, labelled as $n = 1, \ldots, 5$, are identified as field emission resonances. In the $z(U)$-curve, they appear as fairly clear onsets, in the simultaneously obtained dI/dU-spectrum they appear as explicit peaks.

with the energy eigenvalues [69,70]

$$E_n = \Phi_S + \left(\frac{\hbar^2}{2m}\right)^{1/3} \left(\frac{3\pi F}{2}\right)^{2/3} \left(n - \frac{1}{4}\right)^{2/3}, \quad n = 1, 2, 3, \ldots \tag{4.27}$$

As (4.27) shows, the states lie above the vacuum level of the surface, and the energy difference between adjacent states becomes smaller with increasing index. The states can easily be detected by $z(U)$-spectroscopy; an example obtained for Si(111)-$(2\sqrt{3} \times 2\sqrt{3})$Sn [70] is shown in Fig. 4.6. Kubby et al. [70] noted that the position of the field emission resonances seems to depend strongly on the structure of the tip when they obtained different spectra on the same sample and same parameters, but at different times. They attribute this to changes in the work function of the tip, which influences the tip–sample distance considerably.

4.1.4 Quantum well states

The surface localized state that is the most important for this work forms when a thin metal film is deposited on a surface which exhibits a band gap. An electron, whose energy falls in the energy band gap of the surface, is then trapped between the surface and the vacuum. This situation is depicted in Fig. 4.7. In principle, this is the situation of 'a particle in a box', a standard problem of quantum mechanics [10]. For a particle in a box with infinite potential barriers,

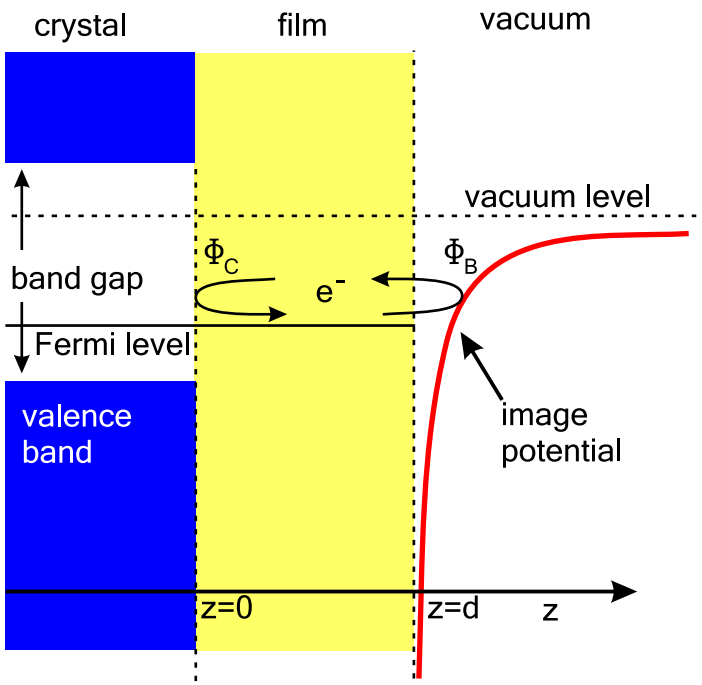

Figure 4.7: An electron in an adlayer is trapped between the surface and the vacuum barrier. It is reflected at the barrier formed by the energy gap at the surface and the vacuum barrier. With each reflection, the electron encounters a phase shift of Φ_B and Φ_C, respectively. Additionally, travelling through the layer gives a phase shift of $2kd$. When the sum of all phase shifts is $2n\pi$, a Quantum Well States forms. (Adapted from [71].)

the solution of the Schrödinger equation is given by

$$\psi_n(z) \propto \sin\left(\frac{n\pi z}{d}\right), \qquad E_n = \frac{\hbar^2}{2m}\left(\frac{n\pi}{d}\right)^2, \tag{4.28}$$

where d denotes the width of the box, m the mass of the particle, and n the index of the state. The energy of the states of the particle is proportional to n^2, in contrast to the image potential states, whose energy is proportional to $1/n^2$. This difference is due to the different potentials applied.

Although the model of the particle in a box leads to a first understanding of these so called Quantum Well States (QWS), reality is more complicated. The barrier defined by the crystal surface is finite, the wave function will therefore leak into the gap. The vacuum barrier, on the other hand, is not a wall, because of its Coulomb characteristics. It is possible to solve the problem with the techniques described in the previous two sections. Often, another way of solving the problem is used, the phase accumulation model [62], a variation of the Bohr-Sommerfeld quantization rule [72]. It is based on the idea of the electron being reflected at the barriers, each time encountering a phase shift upon reflection. The phase shift when reflected from the Coulomb potential,

Φ_B, is approximately [73,74]

$$\Phi_B = \pi\sqrt{3.4\,\mathrm{eV}/(E_V - E)} - \pi, \tag{4.29}$$

where E_V is the vacuum energy level, and E the energy of the electron. The phase shift at the crystal surface is given by the empirical formula [75]

$$\Phi_C = 2\arcsin\left\{\sqrt{\frac{E - E_L}{E_U - E_L}}\right\} - \pi, \tag{4.30}$$

with E_U and E_L the upper and lower boundaries of the band gap. Finally, when travelling through the layer (back and forth), the phase of the electron shifts by $2kd$, where k is the wave vector of the electron perpendicular to the surface. For a stable state to exist, the sum of these three phase shifts has to be an integer multiple of 2π:

$$\Phi_B + \Phi_C + 2kd = 2n\pi. \tag{4.31}$$

The solution will be similar to (4.28), but the deviations from the true particle-in-a-box problem with infinite walls at the boundaries will lead to corrections of the wave-function and the energies, as described for the image potential states, especially

$$E_n = \frac{\hbar^2}{2m}\left(\frac{\pi}{d}\right)^2 (n + \delta n)^2. \tag{4.32}$$

This way of solving the problem has first been introduced to describe image-potential states [62], as the system sketched in Fig. 4.7 reduces to the clean surface case where only the image-potential states are present for $d = 0$. Then $n = 1, 2, 3, \ldots$ denotes the image-potential states. And again, the Shockley state presents itself for $n = 0$ [75].

4.2 Influences on the lifetime of surface localized states

Since surface states, image potential states and quantum well states of metal surfaces as described in the previous section are localized at (or near) the surface, they are confined in two dimensions, and the electrons populating these states behave similar to a two-dimensional free electron gas. Their wave functions can therefore be written as a product of a part parallel and a part perpendicular to the surface:

$$\psi(\vec{r}) = \phi(z)e^{i\vec{k}_\parallel\cdot\vec{r}}, \quad \text{with the energy} \quad E = E_0 + \frac{\hbar^2\vec{k}_\parallel^2}{2m}, \tag{4.33}$$

where $\vec{k}_\parallel$ is the wave vector parallel to the surface, $\phi(z)$ the one-particle wave function describing the motion perpendicular to the surface, and E_0 the corresponding energy. The density of states of a two-dimensional free electron gas is given by surface localized states is [76]

$$\rho_{2D}(E) = \frac{m}{2\pi\hbar^2}\Theta(E - E_0), \tag{4.34}$$

where $\Theta(E)$ is the Heaviside function, i.e. the density of states shows a step at $E = E_0$. Since electrons in surface states can interact with electrons and phonons in the bulk, the model of a free electron gas is not completely correct. The interactions are taken into account by using the effective mass m^* and the self-energy, a complex function which sums all interactions [77]. The density of states becomes [58,76]

$$\rho_S(E) = \frac{m^*}{2\pi\hbar^2}\left\{\frac{1}{2} + \frac{1}{\pi}\arctan\left(\frac{E - E_0}{\Gamma/2}\right)\right\} \tag{4.35}$$

with $\Gamma = 2\Sigma$, where Σ is the imaginary part of the self-energy of the state.[2]

In equilibrium, the states are populated up to the Fermi energy E_F. When an electron is excited, it can occupy a state in the same band, but with energy higher than E_F, or it can be removed from the band, leaving a hole. (Both excitations are treated the same theoretically. In the following discussion, we will use the term 'electrons', keeping in mind that the conclusions are the same for holes.) The lifetime of such an excitation is [78]

$$\tau = \frac{\hbar}{\Gamma} = \frac{\hbar}{2\Sigma} \tag{4.36}$$

The linewidth Γ is influenced by various scattering processes, and the total linewidth is (to lowest order) the sum of all contributions:

$$\Gamma = \sum_i \Gamma_i \tag{4.37}$$

The different contributions are discussed in the following sections.

4.2.1 Electron-electron scattering

Electrons in a surface localized state can interact with electrons in a bulk state, as depicted in Fig. 4.8. The surface electron loses energy and momentum that are transferred to the bulk electron. The bulk electron is excited above the Fermi-level, thus an electron-hole pair is created. The surface state electron can be scattered into a lower unoccupied state of the same band (*intraband scattering*), or into an unoccupied state of another band (*interband scattering*).

The electron-electron contribution to the linewidth is calculated according to [79,80]

$$\Gamma_{e-e} = 2\sum_f \int d^3r \int d^3r'\ \psi_i^*(\vec{r})\,\psi_f^*(\vec{r}\,')\mathrm{Im}[-W(\vec{r},\vec{r}\,';|E_i - E_f|)]\psi_i(\vec{r}\,')\,\psi_f(\vec{r}), \tag{4.38}$$

where the integrals calculate the interaction of electrons in the initial state, described by ψ_i, and the final states ψ_f the electron can scatter into. The sum

[2] It has become customary to use Γ instead of Σ because it is the width of PES-signals, and this technique has long been the standard method to investigate lifetimes of surface states.

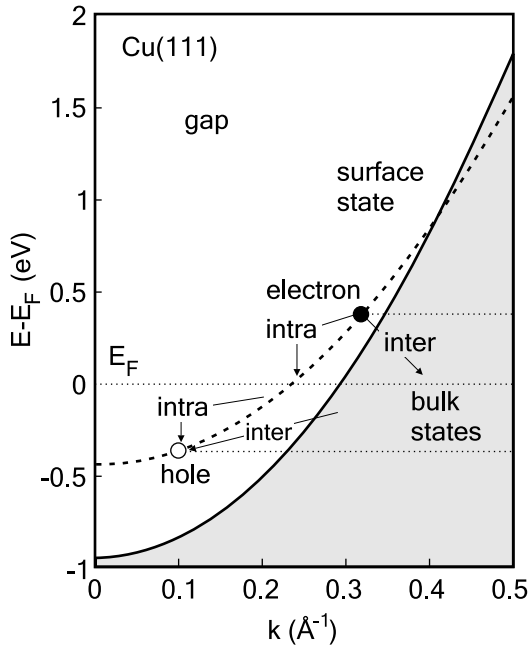

Figure 4.8: Electron-electron scattering processes of surface state electrons/holes, as illustrated for Cu(111). The shaded area marks the bulk states. Electrons/holes in the surface state band can be scattered into surface states of the same band, but at lower energy (intraband), or into bulk states (interband). (Adapted from [79].)

takes into account all possible final states, therefore every possible scattering channel is considered. $W(\vec{r},\vec{r}\,';|E_i-E_f|)$ is the dynamically screened interaction

$$W(\vec{r},\vec{r}\,';\hbar\omega) = v(\vec{r},\vec{r}\,') + \int d^3r_1 \int d^3r_2\, v(\vec{r},\vec{r}_1)\,\chi(\vec{r}_1,\vec{r}_2;\hbar\omega)\,v(\vec{r}_2,\vec{r}\,'). \qquad (4.39)$$

The term $v(\vec{r},\vec{r}\,')$ describes the Coulomb interaction between the electrons, the second term accounts the dynamical screening of excited electron, using the density-response function $\chi(\vec{r}_1,\vec{r}_2;\omega)$ of the system [79].

Performing first-principle calculations as described in Ref. [58], Echenique *et al.* showed that the screened interaction W is localized at the surface, leading to a strong influence of surface localized states on the linewidth (4.39). Γ_{e-e} becomes the largest when the initial as well as the final state are localized at the surface, that is intraband interactions will dominate over interband interactions [58]. The result was that intraband interactions contribute more than 70% of the complete linewidth arising from electron-electron scattering.

Since the electron-electron scattering process requires free electron states as final states, the scattering probability is larger for states with binding energies further away from the Fermi energy E_F [58]. For bulk electrons with energy just above the Fermi level, i.e. $E - E_F \ll E_F$, Quinn and Ferrell found the ap-

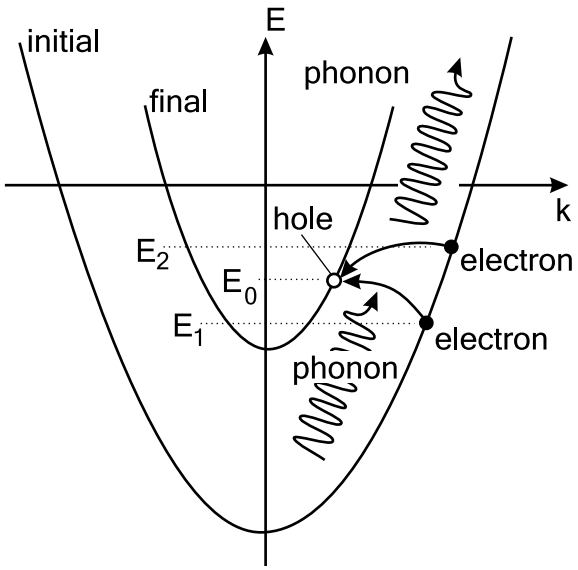

Figure 4.9: Process of electron-phonon scattering. Shown is the dispersion of two electron states. An electron is scattered from the initial state to the unoccupied final state, absorbing or emitting a phonon. The absorbed phonon has the energy $E_0 - E_1$, the emitted one the energy $E_2 - E_0$. The phonon carries the difference in wave vector. (Adapted from [83].)

proximation [81,82]

$$\tau = \frac{263}{r_S^{5/2}(E - E_F)^2}, \tag{4.40}$$

where r_S is the density parameter of the electron gas of density $n_0 = 3/4\pi r_S^2$. When r_S is given in units of the Bohr radius and the energy difference in eV, τ is given in fs. This approximation describes is good for *intra*band interactions, but *inter*band interactions lead to deviations of the experimental values from (4.40).

4.2.2 Electron-phonon scattering

Another process influencing the lifetime of surface states is electron-phonon scattering, sketched in Fig. 4.9. An electron in an initial state with energy E_1 can interact with an incoming phonon of energy $E_1 - E_0$ and change to the final state with energy E_0. The absorbed phonon provides also the difference in momentum. Moreover, an electron in an initial state with energy E_2 can change to the final state with energy E_0 and emit a phonon with energy $E_2 - E_0$ and the difference in momentum. For calculating the electron-phonon linewidth one has to take into account the phonon distribution $n(\varepsilon)$ and the electron distribution $f(\varepsilon)$ [58,80,83]:

$$\Gamma_{e-p}(E) = 2\pi \int_0^{\hbar\omega_m} \alpha^2 F_0(\varepsilon)\,[2n(\varepsilon) + f(E+\varepsilon) + 1 - f(E-\varepsilon)]\,d\varepsilon \tag{4.41}$$

Coverage [ML]	E [meV]	Γ_{e-e} [meV]	Γ_{e-p} [meV]	Γ [meV]
0.95	-42	4.0	8.5	12.5
1.0	-127	13	8.5	21.5

Table 4.1: Different contributions of electron-electron and electron-phonon scattering to the linewidth for different coverages and binding energies of the quantum well states in Na on Cu(111) overlayes. For states nearer to the Fermi energy, the contribution of electron-electron scattering is smaller. (From [80])

where ω_m is the maximum phonon frequency, and $\alpha^2F_0(\varepsilon)$, the Eliashberg function, describes the electron-phonon coupling strength. In the low-temperature limit, $T \to 0$, where $n(\varepsilon) = 0$, (4.41) reduces to

$$\Gamma_{e-p}(E) = 2\pi \int_0^{\hbar\omega_m} \alpha^2F_0(\varepsilon)\, d\varepsilon. \tag{4.42}$$

There are various representations of $\alpha^2F_0(\varepsilon)$, depending on the phonon-model used. However, a detailed analysis [84] showed that the precise form of $\alpha^2F_0(\varepsilon)$ has no large effect on the result.

As has been seen in (4.40), the contribution to the linewidth originating from electron-electron scattering is less dominant for states with energies close to the Fermi energy ($\Gamma_{e-e} \propto (E - E_F)^2$). Therefore, electron-phonon scattering is more important in these cases. Table 4.1 shows the different contributions for quantum well states in Na overlayers on Cu(111). While the electron-phonon contribution Γ_{e-p} is independent on the binding energy E, the electron-electron contribution Γ_{e-e} gets smaller the closer the binding energy gets to E_F, in accordance with (4.40).

4.2.3 Electron-defect scattering

A real surface contains defects such as impurities and steps, which cause electrons to scatter and have influence on the lifetime of states. In contrast to the two processes discussed in the previous sections, electron-defect scattering is elastic, i.e. the energy of the electrons is conserved. To determine the contribution of defects to the linewidth, the mean free path of the electrons is considered [85]. Due to the scattering, the mean free path is

$$\lambda = \Omega_0/c\sigma, \tag{4.43}$$

where Ω_0 is the unit-cell area, c the impurity concentration and σ the scattering cross section. The change of the momentum of the surface state electron is then $\Delta k = 1/\lambda$, leading to a linewidth of [86]

$$\Gamma_{e-d} = v_{\parallel}\Delta k = v_{\parallel}\frac{c\sigma}{\Omega_0}, \tag{4.44}$$

where $v_{\parallel} = \partial E/\partial k$.

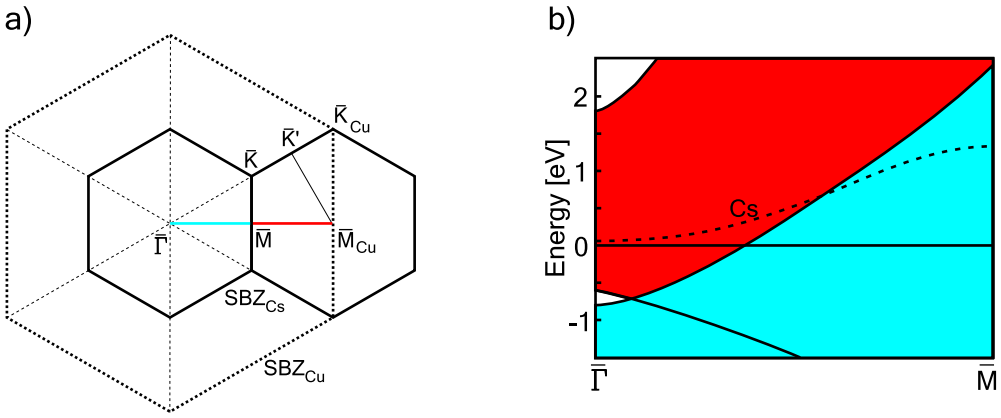

Figure 4.10: Back folding of the surface band structure for Cu(111)-p(2×2). a) Surface Brillouin zones (SBZs) of the Cu substrate (dashed heaxgon) and of the Cs overlayer (bold hexagon). Since the Cs SBZ has half the size of the Cu SBZ, translating it by one reciprocal lattice vector leads to coincidence of, for example, $\bar{\Gamma}$ of the Cs SBZ with $\bar{M}_{Cu}$ of the Cu SBZ. b) Dispersion relation of the quantum well state (dashed line) in the $\overline{\Gamma M}$ direction (blue line in a). Blue indicates the bulk Cu states in the $\overline{\Gamma M}$ direction, red indicates the bulk Cu states in the $\overline{M_{Cu}M}$ direction (red line in a), which are back folded onto the $\overline{\Gamma M}$ direction. (Adapted from [87].)

This approach is useful for PES studies, because in those experiments the average over a large area is taken. In STM studies, however, the *local* density of states is object of investigation. In this case, the impurity concentration does not make sense. Instead, one has to take care that no impurities are near the place where the measurement of the lifetime is done.

4.2.4 Brillouin zone back folding

Only recently, Corriol *et al.* [87] modelled a new scattering process called Brillouin zone back folding that is only present in commensurate overlayers. The basic principle is sketched in Fig. 4.10, taking the p(2×2) superstructure of Cs on Cu(111) as an example. Fig. 4.10 a) shows a sketch of the surface Brillouin zones (SBZs) of the Cu(111) surface (dashed hexagons) and of the adlayer (bold hexagons). The Cs SBZ has half the diameter of the SBZ of Cu. Considering a neighboring SBZ, one sees that the $\bar{\Gamma}$ point of this SBZ coincides with the $\bar{M}$ point at the boundary of the Cu SBZ ($\bar{M}_{Cu}$). This leads to overlapping of the quantum well state dispersion with two parts of the bulk Cu band structure, as depicted in Fig. 4.10 b): First, with the Cu bands in the $\overline{\Gamma M}$ direction (blue), and second with the Cu bands in the $\overline{M_{Cu}M}$ direction (red). This *back folding* from the $\overline{M_{Cu}M}$ direction leads to partial closing of the band gap at the $\bar{\Gamma}$ point. The interaction of the QWS with the back folded Cu states gives rise to new decay channels and therefore shortening of the lifetime.

Additionally to the back folding of the $\overline{M_{Cu}M}$ bands, the Cu bands in the

$\overline{M_{Cu}K'}$ direction are back folded onto the $\overline{\Gamma M}$ direction, as $\overline{K'}$ coincides with $\overline{M}$ (see Fig. 4.10 a). These bands are omitted in Fig. 4.10 b) for clarity.

Calculations of Corriol et al. [87] showed for the $p(2 \times 2)$ structure of Cs and Na on Cu(111) that the scattering due to back folding is responsible for approximately 50% of the total linewidth of 17 meV. Electron-phonon scattering provides another 50%, whereas electron-electron scattering without back folding is negligible for these systems.

Chapter 5

Evaluation of Measured Spectra

One aim in scanning tunneling spectroscopy is to examine the lifetime of surface and quantum well states. The model used to describe the local density of states contains the lifetime as a parameter (see Eq. 4.35):

$$\rho_S(E) = \frac{m}{2\pi\hbar^2}\left\{\frac{1}{2} + \frac{1}{\pi}\arctan\left(\frac{E - E_0}{\Gamma/2}\right)\right\}, \tag{5.1}$$

where $\Gamma = \hbar/\tau$, τ being the lifetime. $\rho_S(E)$ is related to dI/dU-spectroscopy (see Section 2.3). It would now be straightforward to fit an $\arctan(2x/\Gamma)$ to the measured spectrum and extract Γ. However, the spectra are not exact arctan-functions, since the model used to obtain (5.1) is valid only for a two-dimensional free gas of interacting electrons, but the electron gas examined here is located in thin films supported by a metallic substrate. Additionally, the shape and electronic structure of the tip influences the shape of the spectra, which is not taken into account by the model, and the spectrum is modified by the lock-in modulation. Section 5.1 explains the evaluation of the line shape, and Section 5.2 discusses the influence of the lock-in amplifier on the spectrum.

5.1 Line shape

Figure 5.1 shows a typical spectrum of the quantum well state for 0.25 ML Cs on Cu(111). It shows an onset at ≈40 mV, and is strictly horizontal before and after the onset. This horizontality makes the choice of the fitting interval vitally important, since the arctan function can be considered horizontal only far away from the onset. As examples, two fitted curves are included in Fig. 5.1. The green line shows the result of a fit where the interval [-57 mV:143 mV] is used. The curve agrees very well in the horizontal areas, but the slope of the curve deviates from the slope of the spectrum. The red curve, obtained using the interval [23 mV:63 mV], reproduces better the slope of the onset, but deviates from the spectrum outside the fitting interval. The difference of the curves in the area of the onset appears to be small, so it is suggestive to use large fitting intervals as they reproduce better the overall spectrum, but the influence

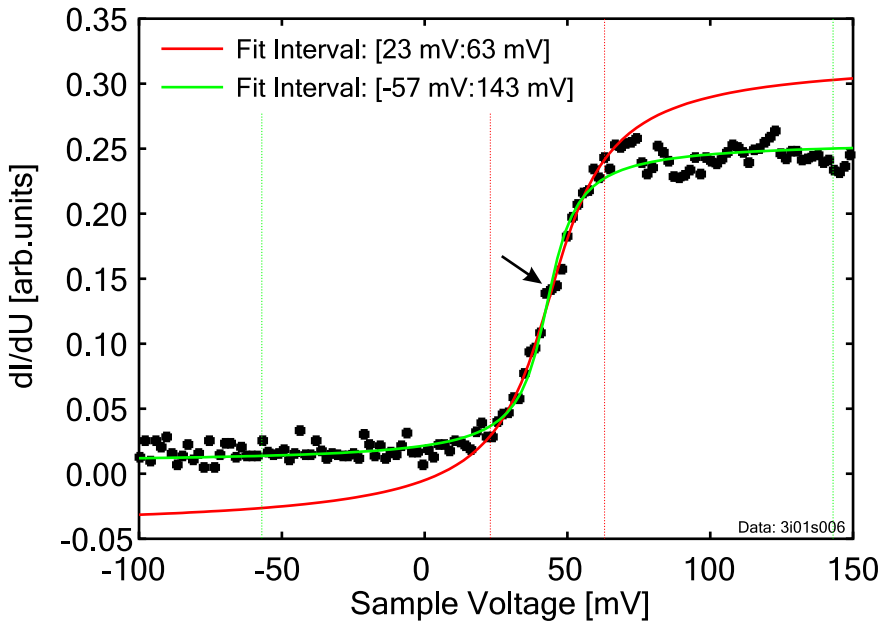

Figure 5.1: Measured spectrum of the quantum well state at a coverage of $\Theta = 0.25\,\mathrm{ML}$ and two fitted curves, based on $f(U) = \arctan(2(U - U_0)/\Gamma)$. The thin vertical lines mark the fitting intervals, which were chosen to be symmetric with respect to $U_0 = 43\,\mathrm{mV}$, the center of the onset. The green curve shows the result of a fit using a large interval, the red curve results from a fit with small interval. While matching the spectrum before and after the onset, the green curve does not reproduce the slope of the onset. The red curve reproduces the slope, but deviates outside the fitting interval. The arrow marks a kink in the middle of the onset which has a large effect on the result of the fitting as shown in Fig. 5.2.

of the fitting interval on the resulting width is large, as shown in Fig. 5.2. For large fitting intervals, where the resulting curve fits the horizontal areas of the spectrum, the resulting width of the onset is small, ≈16 meV. When the fitting interval gets smaller than 100 mV, the width increases, up to 31 meV for 40 mV fitting interval. The value of the width obtained by evaluating the slope of the onset is 27 meV, which is not reproduced by small fitting intervals because of the kink in the middle of the spectrum where three neighboring points form a flat terrace (marked by the arrow in Fig. 5.3). This shows how delicate the fitting procedure is.

Given that the spectrum is smooth around the middle of the onset, a small fitting interval is the best choice, since Γ determines the slope of the onset. However, when a small fitting interval is used, only few points contribute to the fitting, which lowers the accuracy.

Instead of fitting an arctan-function, an approach proposed by Li et al. [88] is used in this work. The experimental spectrum is approximated by three lines as sketched in Fig. 5.3: two lines render the spectrum before and after the

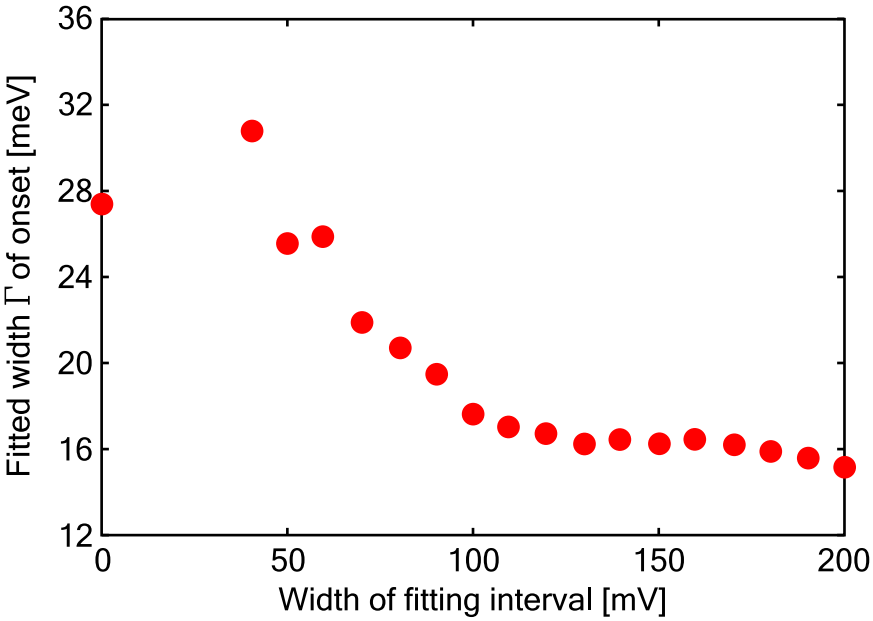

Figure 5.2: Result of the $\arctan(2U/\Gamma)$-fit to the data in Fig. 5.1 in dependence on the used fit interval. The fitting intervals were chosen to be symmetric with respect to $U_0 = 43\,\mathrm{mV}$, the middle of the onset. For large fitting intervals, the resulting width is smaller than the value of 27 meV obtained by evaluating the slope of the onset, for small fitting intervals it gets larger than the real value. This exceptional behavior is due to the kink in the middle of the spectrum and shows how delicate the fitting procedure is.

onset, one reproduces the slope in the middle of the onset. The crossing points of the lines mark the width Δ of the onset. Simple geometric considerations lead to

$$\Delta = \frac{\pi}{2}\Gamma. \tag{5.2}$$

The binding energy E_0 of the state lies in the middle of the crossing points of the approximation lines.

5.2 Broadening by lock-in modulation

To obtain a spectrum, a lock-in technique is used: A sinusoidal modulation voltage of small amplitude U_m and frequency f_m is added to the tunneling voltage, and a lock-in amplifier measures the contribution to the current with frequency f_m. The lock-in signal is proportional to the conductance and is given by [89]

$$\left[\frac{dI}{dU}(U)\right]_{\mathrm{lock-in}} = \int_{-\infty}^{+\infty} \left[\frac{dI}{dU}(U')\right] \chi_{\mathrm{lock-in}}(U' - U)\, dU' \tag{5.3}$$

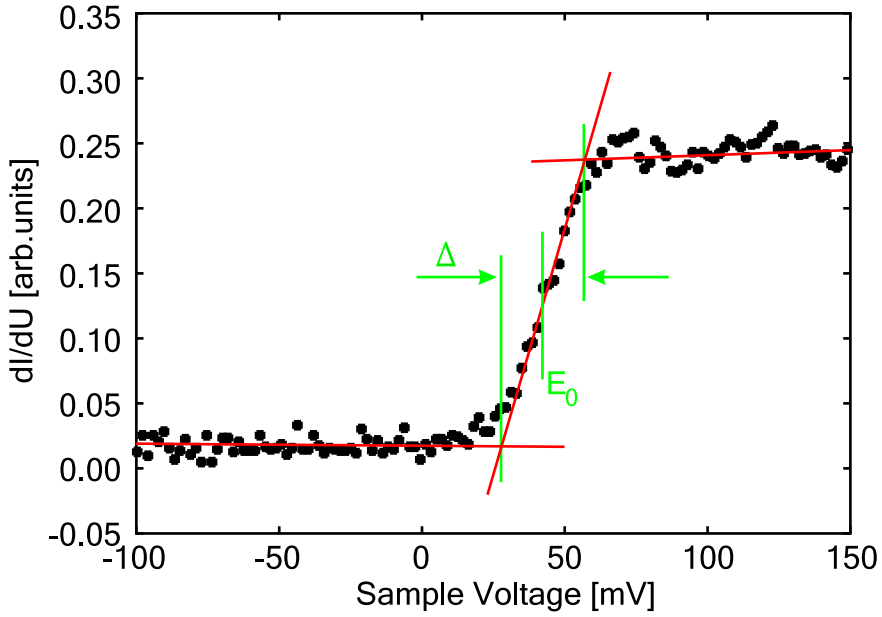

Figure 5.3: To determine the linewidth and the binding energy of the state, the spectrum is approximated by three lines. The crossing points determine the width $\Delta = (\pi/2)\Gamma$, the binding energy E_0 lies in the middle of the crossing points.

where $[dI/dU(U)]$ is the real conductance, and $\chi_{lock-in}(U)$ the lock-in instrumental function

$$\chi_{lock-in}(U) = \begin{cases} \frac{2}{\pi}\frac{\sqrt{U_m^2 - U^2}}{U_m^2}, & |U| \le U_m \\ 0, & |U| > U_m \end{cases} \tag{5.4}$$

Thus, the measured conductance is the convolution of the real conductance and the lock-in instrumental function. The convolution replaces $[dI/dU]$ with the average of its values in the range of U_m. In effect, the lock-in technique leads to broadend spectra. The effect is larger for larger modulation amplitudes U_m

A quantification of the broadening was found by Li et al. [88]:

$$\frac{\Delta}{\Delta_0} = \frac{1}{2}\left\{\sqrt{1 + \pi^2\left(\frac{U_m}{\Delta_0}\right)^2} + 1\right\} \tag{5.5}$$

The function is plotted in Fig. 5.4. If the modulation U_m is small compared to the natural width Δ_0, the effect of broadening is negligible, whereas it gets almost linear with larger modulation. Since Δ_0 is cannot be obtained by experiment, it is convenient to rewrite (5.5) as

$$\frac{\Delta_0}{\Delta} = 1 - \frac{\pi^2}{4}\left(\frac{U_m}{\Delta}\right)^2, \tag{5.6}$$

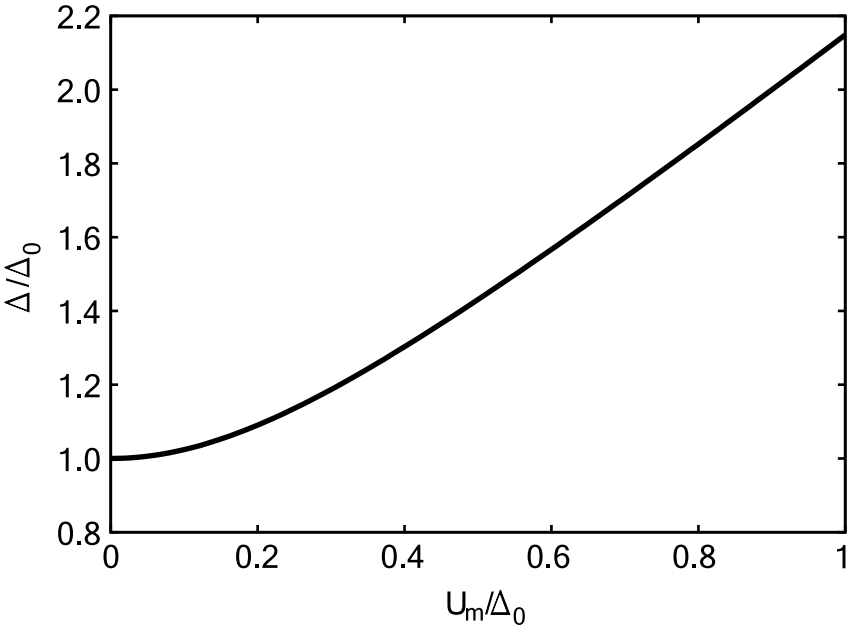

Figure 5.4: The natural width Δ_0 of the onset is broadend by the lock-in amplifier to the experimental width Δ as described by Eq. 5.5. U_m denotes the amplitude of the voltage modulation.

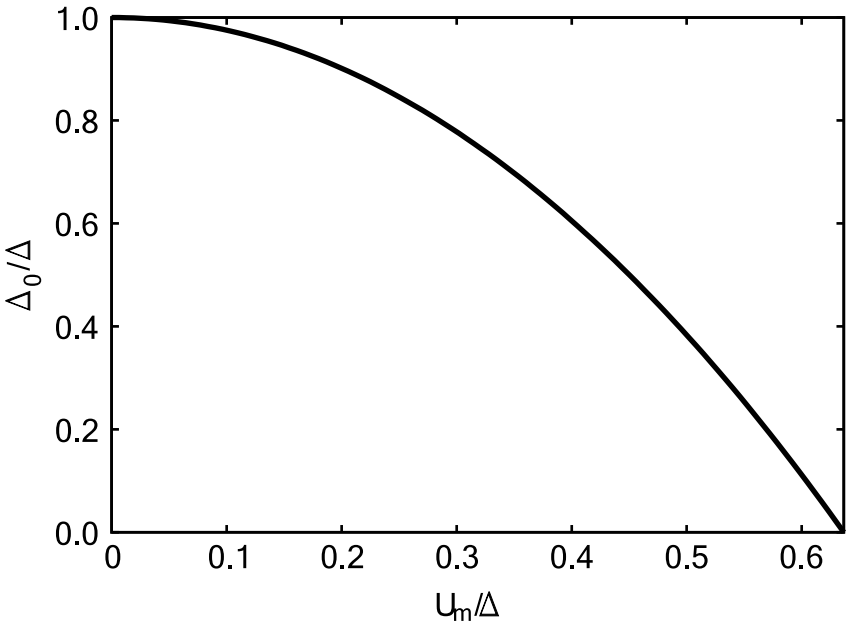

Figure 5.5: Factor to correct the measured width Δ of a state in dependence on the modulation amplitude U_m. (See Eq. 5.6) For very large U_m, U_m/Δ becomes $2/\pi$ independent of U_m. Then, the Δ is so large that the correction factor becomes zero.

plotted in Fig. 5.5. This formula gives the factor to correct the experimental width Δ to get the natural width Δ_0 for the used modulation amplitude U_m. For example, when an experimental width of $\Delta = 43\,\mathrm{meV}$ is measured using a modulation of $U_{rms} = 2\,\mathrm{mV}$, that is $U_m = 2.8\,\mathrm{mV}$, the correction factor is $\Delta_0/\Delta = 0.99$, the natural width is therefore 42.5 meV; the difference is negligible. For the same experimental width, but a modulation of $U_{rms} = 5\,\mathrm{mV}$, the correction factor is 0.93, resulting in a natural width of $\Delta_0 = 40\,\mathrm{meV}$, which is considerably smaller than the experimental value.

When the modulation amplitude is very high compared to the natural width, the experimental width becomes independent from the natural width:

$$\left(\frac{U_m}{\Delta}\right) = \frac{2}{\pi}\sqrt{1 - \left(\frac{\Delta_0}{\Delta}\right)} \leq \frac{2}{\pi} \approx 0.6366 \tag{5.7}$$

In this case, the linear area of Fig. 5.4 is reached. No correction is possible.

Extending the evaluation of the spectra by fitting an arctan-function, it has been proposed to take into account the lock-in broadening by using a Gaussian as a model for the lock-in broadening [90]. Besides, the derivative of the spectrum is used, because the derivative of the theoretical description of the spectrum (4.35,5.1) is a Lorentzian. To evaluate the spectra, the convolution of a Lorentzian and a Gaussian, the Voigt-function, is used. While the influence of the wrong weighting using the Gaussian to describe the lock-in broadening results in an error of about 1.2% and may be negligible, to fit a Lorentzian to the numerical derivative of the experimental spectrum has some drawbacks. First, the measured spectra do not follow arctan-functions as described in the previous section. Therefore, the derivative of a spectrum will not be a true Lorentzian, and the fitting problems remain. Second, taking the numerical derivative of an experimental spectrum enhances noise. One can take care of this problem by smoothing the spectrum or its derivative, but since smoothing is done by averaging neighboring data points, this process can introduce broadening itself.

Chapter 6

Cesium on Copper(111)

6.1 Introduction

The study of the adsorption of alkali metals on single-crystal metal surfaces has a long tradition in surface science. This is partly due to potential technological applications like the promotion of catalytic reactions [91], an enhanced oxidation [92–95], and an increase in electron emission rates [96, 97]. From a scientific point of view alkali-metal atoms are, due to their simple electronic structure, ideal candidates for model chemisorption studies [98, 99].

Structural characterization of alkali adsorbate systems has been a central issue during the last decades. From this research the following general picture of alkali adsorption on metal surfaces can be inferred. Due to charge transfer from the adsorbed alkali atom to the substrate, the alkali adatoms become partially charged [100]. The induced dipoles then cause the atoms to repel from each other leading to homogeneous adatom arrangements. As a result, at very low coverages low-energy electron diffraction (LEED) patterns reveal rings around the (0,0) spot [101–105]. The formation of rings in LEED patterns indicates a superstructure of randomly distributed adsorbed atoms with a prevailing mutual distance. In contrast, higher coverages usually lead to sharp diffraction spots indicating a superstructure with long-range-order periodicity. At room temperature, superstructures were observed only for commensurate phases, as for Co(10$\bar{1}$0)-K [106], Au(100)-K [107] and Ni(111)-K [108]. Below room-temperature, incommensurate phases are reported that are aligned with the substrate, for instance Ag(111)-K, -Rb, -Cs, [105] and Ni(100)-K [109]. Also, rotation of an incommensurate phase with respect to the substrate, where the rotation angle depends continuously on the coverage, was observed for various systems, namely C(0001)-Cs [110], Pt(111)-Na [102], Pt(111)-K [111], Ru(0001)-Li [112], Ru(0001)-Na [113], Ag(111)-K, -Rb, -Cs [105], Cu(100)-K and Ni(100)-K [109], and Rh(100)-Cs [114]. Models which describe the rotational behavior base on domain walls aligning with a symmetry direction of the substrate [115], higher-order commensurate phases [116], response of an elastic overlayer to a small-amplitude corrugation of the substrate po-tential [117,118] or domain walls aligning to the substrate up to a critical misfit of

adlayer and substrate [119,120].

For substrate surfaces with square or rectangular symmetry the alkali atoms occupy adsorption sites which maximize the coordination number to the substrate [121–127]. The on-top adsorption site is frequently observed for hexagonally close-packed substrate surfaces, for instance Cu(111)-p(2×2)Cs [128], Al(111)-$(\sqrt{3}\times\sqrt{3})$Rb [129], and Ni(111)-p(2×2)K [130] to name only a few, and bridge site for Rh(111)-p(2×2)Rb [131]. For the systems with top-site adsorption, LEED studies showed that the adatoms push their supporting atom into the surface, leading to surface rumpling and an increase of the coordination number [132].

Two publications report on the geometrical structure of Cs adsorbed on Cu(111). Lindgren *et al.* found by LEED investigations [128] that Cs saturates with the first monolayer on Cu(111) at room temperature. The structure of this layer is a p(2×2) structure, i. e. one Cs atom on every second Cu atom, which reflects the ratio of atomic radii of 2:1 of Cs and Cu atoms. They also found that Cs adsorbs on top of Cu atoms in this structure, which was the first time that an adsorption site other than hollow was reported. For lower coverages they observed the ring formation described above. More extensive studies of the system were carried out by Fan *et al.* [133] They examined adsorption structures in the temperature range between 80 K and 500 K. They found that the saturation coverage increases to 0.28 ML at 80 K, where 1 ML is defined as one Cs atom per Cu atom. They did not find any commensurate phases down to 80 K except the already known p(2×2) phase. However, they reported on orientationally ordered incommensurate phases for coverages $\Theta > 0.12$ ML at 80 K.

Adsorption of alkali metal atoms on metal surfaces is not only interesting in terms of geometric structure, but leads to many new electronic phenomena. The first extensive study of alkali adsorption on metal surfaces was performed by Langmuir and Taylor [96,134]. They found that the work function changes significantly with the coverage. This is explained by polarization of the alkali atoms upon adsorption [99,100,135] and has been observed for many systems, for example Ni(110)-Na, K, Cs [136], Fe(100)-K [137], Pt(111)-K [138], Cu(111)-Na [139] and Cu(111)-Cs [140].

When alkali atoms adsorb on a surface, new states can be detected by photoemission-experiments [141]. For low coverages, they are attributed to atomic alkali levels [142, 143]. At higher coverages, when the atom orbitals overlap and the adlayers become metallic, these states evolve into quantum-well states [141, 144]. The binding energy of the atomic states and the quantum-well states (QWS) depend on the coverage as well, as has been shown for Cu(111)-Na [139, 145], Be(0001)-Li [146], and Al(111)-K, Na, Cs [147]. Of fundamental interest is the lifetime of QWS, because it is influenced by several processes as described in Chapter 4.2. Standard techniques to measure the lifetime are inverse photoemission spectroscopy and two-photon photoemission spectroscopy [58, 148], and scanning tunneling spectroscopy doing a line shape analysis [84, 149] as described in Chapter 5.1, or by recording standing

wave patterns [150, 151].

The following two sections deal with Cs adsorbed on Cu(111). Sec. 6.2 shows structural properties of the system and Sec. 6.3 addresses its electronic properties.

The samples were prepared as follows: A clean copper surface was prepared by repeated ion bombardment and anneal cycles. After cooling the copper sample to room temperature, Cs was dosed on the surface from a Cs dispenser from *SAES Getters* [152]. The evaporation rate was monitored with a quartz balance. For atomically resolved images, the coverage was determined by measuring the interatomic distances of the Cs atoms. These data were also used to calibrate the quartz balance. The coverage of layers for which atomic resolution was not obtained was determined using the calibrated quartz balance rate. After the preparation at room temperature, the sample was transferred into the STM and cooled to 9 K. STS was performed using a lock-in technique with modulation voltages of 1-3 mV_{rms}=2.8-8.5 mV_{pp} amplitude.

6.2 Geometric Structure

The orientation of the substrate lattice has been deduced from the LEED image shown in Fig. 6.1a. The diffraction spots in LEED are rotated by 17° counterclockwise with respect to the sample holder. Since the diffraction pattern is rotated by 90° with respect to the lattice, the lattice is rotated by 47° counterclockwise (or, equivalently, 13° clockwise) with respect to the sample holder. When the sample is transferred into the STM, its orientation does not change, i.e. the indicated orientation of the directions of close-packing in Fig. 6.1b is the orientation as it would be observed in STM images.

Typical constant-current STM images of Cu(111)-Cs acquired at room temperature (not shown) do not reveal any adsorbate superstructure. The presence of the adsorbate was inferred from a noisy tunneling current, which is usually not observe on clean metal surfaces. Further, step edges were not imaged as straight lines. Rather, step edges appear frayed in constant-current STM images. We attribute these observations to mobility and to tip-induced movements of the Cs adatoms. Due to the instability of the tunneling junction, tunneling spectroscopy measurements were difficult to perform in a reproducible manner at room temperature. As a consequence the experiments were performed at 9 K. The data to be presented in the following were acquired at low temperature.

6.2.1 Low Coverage: $\Theta = 0.05$ ML

Figure 6.2a shows a representative constant-current STM image of Cu(111) covered with 0.05 ML Cs revealing an area of more than 2500 nm^2 with a step crossing in the lower right. Hexagonally ordered white circular protrusions cover the whole image. We observed this superstructure for many different

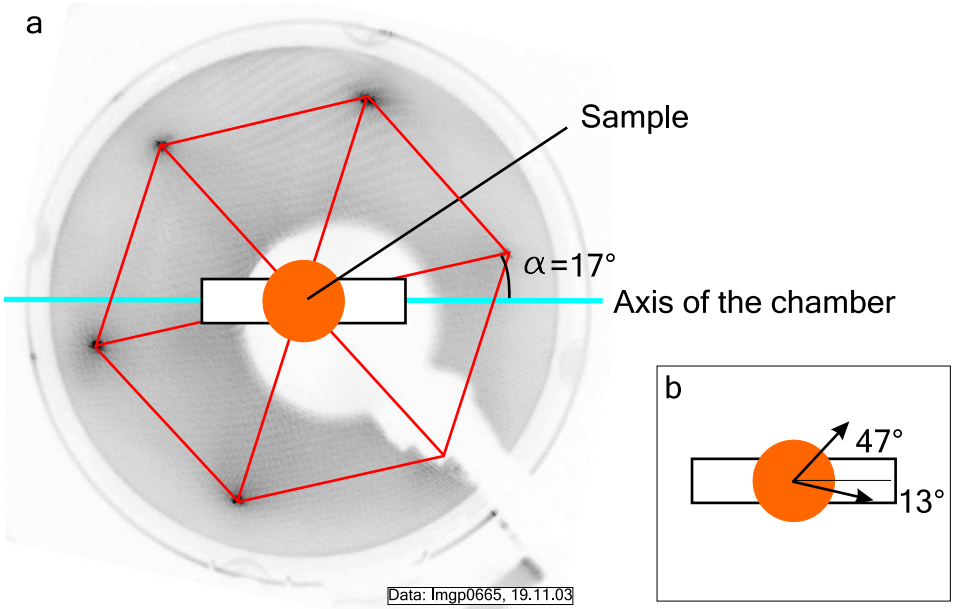

Figure 6.1: a) LEED image of clean Cu(111). The hexagonally ordered spots (one is covered by the retainer of the diffractometer) show the ordering of the Cu(111) surface. The blue line indicates the axis of the preparation chamber. The position and orientation of the sample is sketched. The hexagon of the LEED spots are rotated by 17° with respect to the sample. b) The directions of close-packing with respect to the sample. The sample is oriented in the STM as shown.

areas of the sample. The close-up view in Fig. 6.2b shows the hexagonal Cs superlattice in more detail. From this image an interatomic distance of 1.1 nm can be determined. The corrugation of the superlattice is ≈0.03 nm. The arrows indicate directions of close packing of the Cu(111) substrate ($[01\bar{1}]$) and of the adlayer. Evidently the Cs layer is rotated by ≈23° with respect to the Cu(111) surface. On the right side of Fig. 6.2a defects of the adsorption layer are observed. We attribute these defects to imperfections of the Cs layer, i.e., to missing Cs adatoms. To corroborate this assumption a close-up view of the defect in the upper right corner of Fig. 6.2a is shown in Fig. 6.2c. The black circles indicate the positions of Cs atoms in the layer, while the white circles continue the hexagonal lattice inside the defect structure. From this image we infer that the dark area corresponds to missing Cs atoms.

The hexagonal order of the adatoms extends over large areas. In some regions, atomic resolution of the adsorbate layer is lost during scanning. These regions appear as blurred stripes in the fast scanning direction (from top to bottom in Fig. 6.2d). In ≈40 % of the cases where the blurred stripes appear, adjacent Cs-covered areas are shifted with respect to each other by half a superlattice constant as indicated by white lines in Fig. 6.2d. We attribute this observation to adjacent Cs adsorption domains. In both domains Cs atoms reside at stable adsorption sites, while in the region between the domains no such stable

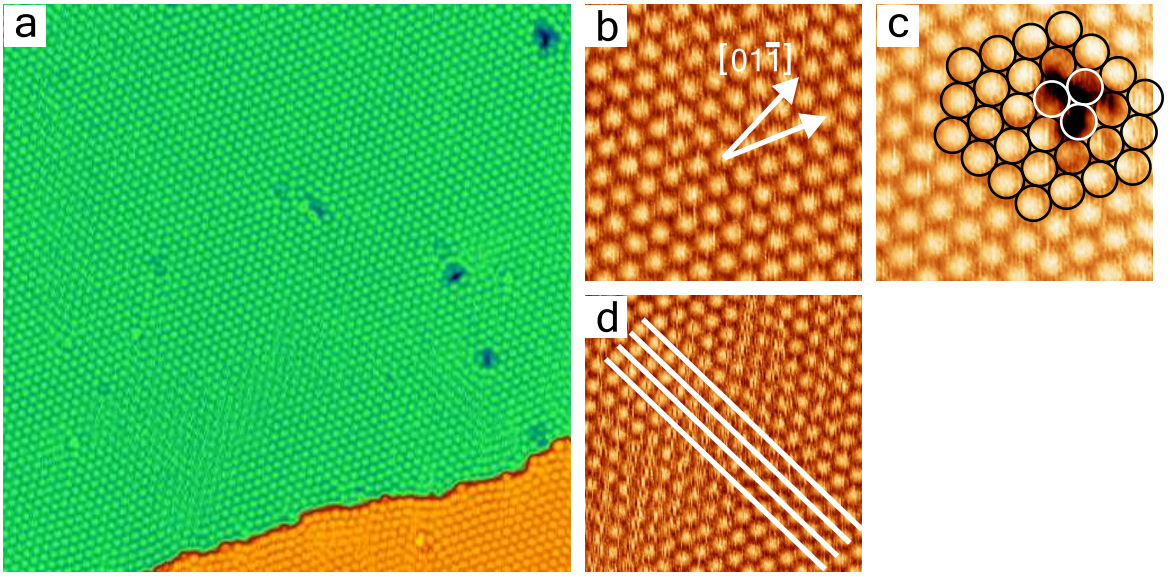

Figure 6.2: a) Constant-current STM image of the Cu(111)-Cs surface at 0.05 ML. The white circular protrusions are assigned to single Cs atoms. (58 nm×58 nm, tunneling parameters: $V = -600$ mV, $I = 0.1$ nA; fast scan direction is from top to bottom.) b) Close-up view of an area of 10 nm×10 nm. The indicated $[01\bar{1}]$ direction corresponds to a close packing direction of the substrate ($V = -600$ mV, $I = 0.1$ nA). c) Close-up view (9 nm×9 nm) comprising a defect in the top right corner of the image. The black circles indicate the position of adjacent Cs atoms, while the white circles continue this hexagonal lattice also inside the defect structure. d) Close-up view (14 nm×14 nm) indicating that two adjacent Cs domains (upper left and lower right quarter) are mutually shifted by half an adatom row.

adsorption site is available. As a consequence, Cs atoms in these regions are prone to be moved by the tip leading to the observed loss of atomic resolution.

The measured interatomic distance of 1.1 nm and the rotation angle of 23° match well a $(\sqrt{19} \times \sqrt{19})\,\mathrm{R}\,23.4°$ commensurate phase. Stabilization of this commensurate superstructure may arise from long-range adsorbate-adsorbate interactions mediated by substrate electrons. Lau and Kohn [153] predicted that adsorbates may interact via Friedel oscillations [154] through the fact that the binding energy of one adsorbate depends on the substrate electron density, which oscillates around the other adsorbate. Lau and Kohn later found for a two-dimensional electron gas that these interactions depend on distance, r, as $r^{-2}\cos(2\,k_F\,r)$ where k_F is the Fermi vector [155]. The Cu(111) surface hosts an electronic surface state which is a model system for a two-dimensional free electron gas. The Fermi vector of this surface state is $k_F \approx 0.022\,\mathrm{nm}^{-1}$ [156] giving rise to Friedel oscillations with the Fermi wavelength $\lambda_F = 2\pi k_F^{-1} \approx 2.9$ nm. Indications of such a long-range interaction between strongly bonded sulfur atoms on a Cu(111) surface have been first reported in [157]. The first quantitative study of a long-range interaction mediated by a

two-dimensional nearly free electron gas was reported by Repp et al. [158] for Cu(111)-Cu and later for Cu(111)-Cu, Cu(111)-Co, and Ag(111)-Co by Knorr et al. [159] The closest separation between two Cu adatoms was 1.25 nm corresponding roughly to $\lambda_F/2$ of the Cu(111) surface state. An atomic superlattice was also observed for adsorbed Ce atoms on a Ag(111) surface [160]. The observed 3.2 nm periodicity of the superlattice was assigned to the interaction of surface-state electrons with the Ce adatoms.

The interaction energy between adsorbates as mediated by surface state electrons was found to be [156]

$$\Delta E_{int}(r) \simeq -E_F \left(\frac{2\sin\delta}{\pi}\right)^2 \frac{\sin(2k_F r + 2\delta)}{(k_F r)^2} \tag{6.1}$$

where E_F denotes the Fermi energy measured from the bottom of the surface-state band and δ is the phase shift, which depends on the scatterer. Inserting the experimentally observed mutual Cs distance of (1.1 ± 0.1) nm into Eq. (6.1) leads to a phase shift of $\delta = (0.43 \pm 0.08)\pi$. This is close to the value of $\delta = (0.50 \pm 0.07)\pi$ for Cu and Co on Cu(111) [159], and $\delta = (0.37 \pm 0.05)\pi$ for Ce on Ag(111) [160,161]. The similarity of these values indicates that the phase shift does not vary appreciably among these scatterers with different chemical nature. We notice, however, that Hörmandinger and Pendry [162] investigated the interaction of Cu, Fe, S, and C atoms with the Cu(111) surface state. As a result of their calculations, the probabilities of surface state electrons being reflected, transmitted, or scattered into bulk states differ depending upon the individual scatterer. Since the value of δ in our case, i.e., Cu(111)-Cs, is similar to the phase shifts obtained from the systems above, we have additional evidence that the interaction between Cs adatoms at low coverages is mediated by the Cu(111) surface state.

6.2.2 Intermediate coverage: $\Theta = 0.15 - 0.20$ ML

Higher Cs coverages led to an increase of the radius of the ring structure in the LEED pattern at room temperature pointing to a decrease of the average separation between Cs atoms [128]. A typical constant-current STM image of Cu(111) covered with 0.18 ML Cs is shown in Fig. 6.3a. An almost closed Cs layer, which is disrupted by small and irregularly shaped indentations is observed. Occasionally, these structures occur within a closed Cs layer, but most frequently they are observed at step edges. The apparent depth of the indentations depends on the applied voltage. Atomic resolution of flat areas of the Cs layer is presented in Fig. 6.3b. Again, the white protrusions are identified as Cs atoms. Distances between nearest neighbors are 0.60 nm for this coverage. The corrugation of the superlattice is 0.003 nm which is considerably smaller than for $\Theta = 0.05$ ML. This observation is attributed to the Cs adatoms being more densely packed at higher coverage. Comparing with the Cu(111) substrate lattice the rotation angle of the adsorbate layer is 4°. The same values for the interatomic distance, the rotation angle, and the corrugation were obtained at various areas on the sample.

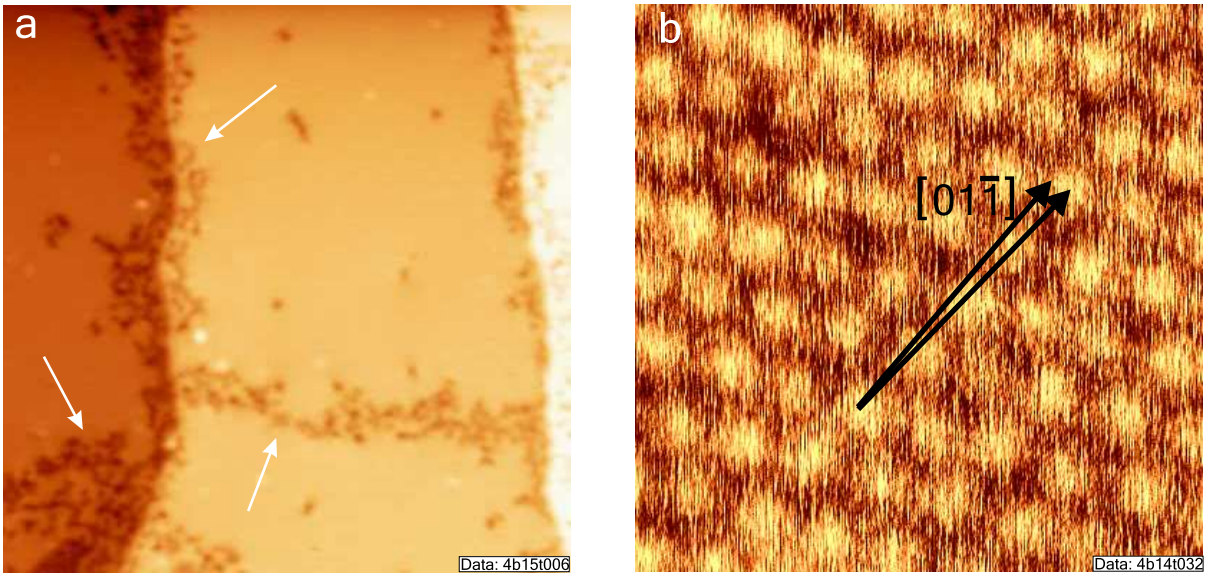

Figure 6.3: a) Constant-current STM image of Cu(111)-Cs at 0.18 ML. The Cs layer is almost closed, only at step edges and occasionally inside the layer, irregularly formed patterns (marked by arrows) are observed (62 nm × 62 nm, $V = 200$ mV, $I = 0.1$ nA). b) Close-up view of a scan area inside the closed Cs layer displayed in a. The white circular protrusions are assigned to single Cs atoms. Crystallographic orientation of Cu(111) is indicated (4.5 nm × 4.5 nm, $V = 50$ mV, $I = 0.1$ nA).

For Cs coverages of 0.15 ML and 0.20 ML Cs-Cs distances of 0.66 nm and 0.57 nm occur, respectively. The adsorbate layers are rotated with respect to the substrate lattice by 17° and 0°, respectively. Upon increasing the coverage the Cs adlayer becomes more and more disrupted. Instead of a closed adsorption layer numerous small Cs islands are observed (see the results for saturation coverage).

For the Cs superlattices observed at intermediate coverages, no coincidence of the substrate and adsorbate lattice was found. Consequently, on the basis of the STM investigation, the adsorption layers in the intermediate coverage regime are proposed to be incommensurate. The rotation angle of the incommensurate Cs adsorbate layers on Cu(111) as a function of the misfit $(d_{Cs} - d_{2\times2})/d_{2\times2}$ is shown in Fig. 6.4 (circles). Here d_{Cs} denotes the nearest-neighbor distance of the Cs adsorption layer and $d_{2\times2}$ the distance of the Cs atoms in the p(2 × 2) superstructure. The Cu(111) substrate surface has a lattice constant of $d_{Cu} \approx 0.255$ nm at room temperature [43], leading to a nearest-neighbor distance of Cs adatoms in the p(2 × 2) superstructure of $d_{2\times2} \approx 0.51$ nm. (Since the linear thermal expansion coefficient is $\alpha = 1.65{\cdot}10^{-5}$/K at room temperature and smaller for lower temperatures [48], the nearest-neighbor distance contracts by less 0.5 %, which can be neglected.) Data adapted from Ref. [105] displaying the rotation angles for incommensurate phases of Ag(111)-Cs at 35 K obtained by LEED (triangles), are added.

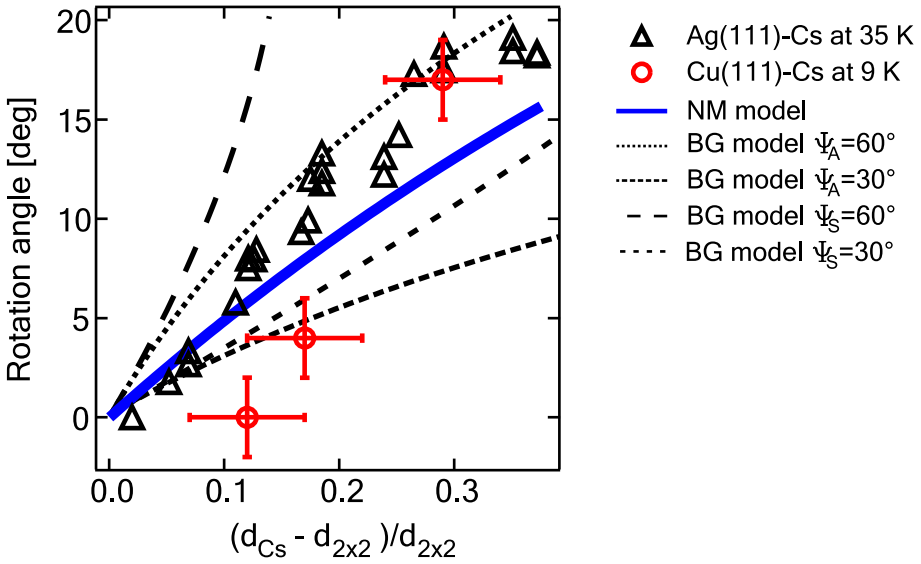

Figure 6.4: Rotation angle of a Cs adlayer on Cu(111) and Ag(111) versus misfit, misfit being defined as $(d_{Cs} - d_{2\times2})/d_{2\times2}$ where d_{Cs} is the atomic distance in the layer and $d_{2\times2}$ the atomic distance in the (2×2)-superstructure. Circles: Rotation angle of Cs adlayer on Cu(111); Triangles: Rotation angle of Cs adlayer on Ag(111) as adapted from Ref. [105]; Dashed lines: Calculation according to the model by Bohr and Grey; Solid line: Calculation according to the model by Novaco and McTague. The models are described in the text.

While the general trend of increasing rotation angle with increasing misfit (decreasing coverage) is observed for the two adsorbate systems, the rotation of adsorbate layers starts at larger misfits in the case of Cu(111)-Cs.

The rotation of adsorbed overlayers relative to the substrate has been observed before for many adsorption systems [115, 163]. As a consequence, several attempts arose to theoretically explain the rotational behavior of adlayers [105]. A simple geometrical model first applied by Doering [116] proposes that the overlayer forms a higher-order commensurate phase, where the superstructure unit cell is much larger than the unit cell of the substrate surface. This leads to a large number of possible rotation angles for each misfit. It remains unclear why a specific orientation of the higher-order commensurate phase arises. Another geometrical model by Bohr and Grey [115] makes use of domain formation. The domains in question are the result of a Moiré pattern: Because the adlayer has larger interatomic spacings than the substrate there are domains where the adatoms are nearly in phase with substrate atoms; the separating areas, where the displacement is larger, are called domain walls [163]. The assumption of the model is that the layer aligns to the substrate in such a way that the domain walls are oriented in a high-symmetry direction of the substrate or of the layer to minimize energy. When denoting the angle by which the domains walls are rotated with respect to the substrate by Ψ_S, the

rotational angle θ of the layer with respect to the substrate is calculated by

$$\cos\theta = r_{AS}\sin^2\Psi_S + \cos\Psi_S\sqrt{1 - r_{AS}^2\sin^2\Psi_S}, \qquad r_{AS} = \frac{d_{Cs}}{d_{2\times2}}, \tag{6.2}$$

where d_{Cs} denotes the interatomic distance in the Cs layer and $d_{2\times2}$ the lattice constant of the 2×2 superstructure. A similar formula is obtained when regarding the angle of rotation Ψ_A of the domain walls with respect to the adlayer. The angles Ψ_S and Ψ_A, i.e. the high-symmetry directions, can be 30° and 60° for the hexagonal lattice. The four resulting curves for the angle of rotation θ are added in Fig. 6.4 as dashed lines. The curves for $\Psi_S = 60°$ and $\Psi_A = 60°$ reproduce the experimental data the best, but it remains unclear which high-symmetry direction is realized by the system.

Instead, the model by Novaco and McTague [117,118] was applied. Within this model the rotation angle of the adsorbate layer with respect to the substrate lattice is determined on the basis of a weak adsorbate-substrate interaction. Within a semiclassical approximation Novaco and McTague found the rotation angle to depend on the ratio of the longitudinal and transverse speed of sound in the adsorbate layer, c_L and c_T, respectively, and upon the ratio of the lattice constants of the substrate, $d_{2\times2}$, and the adsorbate layer, d_{Cs}:

$$\cos\theta = \frac{1 + z^2(1 + 2\eta)}{z\,[2 + \eta(1 + z^2)]} \tag{6.3}$$

with $\eta = (c_L/c_T)^2 - 1$ and $z = d_{2\times2}/d_{Cs}$. While the lattice constants are known, little is known about the sound velocities in thin films. For alkali metals on noble metal surfaces, phonon dispersion curves were measured for Na, K and Cs on Cu(001) [164–166]. From the phonon dispersion relations of Cs on Cu(001) [166], we know that $c_L/c_T = 1.2$, which does not lead to rotation according to Eq. (6.3). Therefore, the ratio of sound velocities of the Cs adsorption layer is calculated by solving the two-dimensional dynamical equation

$$M\,\frac{d^2\vec{x}_n}{dt^2} + \sum_m \Phi_n^m\,\vec{x}_m = 0, \tag{6.4}$$

where $\vec{x}_n$ denotes the excursion the atom in unit cell n from equilibrium, M is the adatom mass, and

$$\Phi_n^m = \frac{\partial^2\Phi}{\partial\vec{x}_n\,\partial\vec{x}_m} \tag{6.5}$$

are the coupling constants, which are calculated as the second derivative of the interaction potential. Using the ansatz of plane waves,

$$\vec{x}_n = \frac{1}{\sqrt{M}}\vec{u}(\vec{q})e^{i(\vec{q}\cdot\vec{r}_n - \omega t)}, \tag{6.6}$$

(6.4) transforms to

$$-\omega^2\vec{u}(\vec{q}) + D(\vec{q})\vec{u}(\vec{q}) = 0, \tag{6.7}$$

where $D(\vec{q})$ is the dynamical matrix which is defined as

$$D(\vec{q}) = \frac{1}{M} \sum_{m} \Phi_n^m e^{i\vec{q}\cdot(\vec{r}_m - \vec{r}_n)}. \tag{6.8}$$

$D(\vec{q})$ depends only on the difference $\vec{r}_m - \vec{r}_n$, therefore the choice of the point of reference $\vec{r}_n$ is not relevant, and the index n is omitted. Eq. 6.7 has a solution only if its characteristic determinant vanishes:

$$\det\left\{D(\vec{q}) - \omega^2\right\} = 0. \tag{6.9}$$

Since (6.4) is 2-dimensional, (6.9) results in two dispersion relations $\omega_L(\vec{q})$ (longitudinal mode) and $\omega_T(\vec{q})$ (transverse mode). From these, the sound velocities are obtained by

$$c_i = \left.\frac{\partial \omega_i}{\partial \vec{q}}\right|_{\vec{q}=\vec{0}}. \tag{6.10}$$

In the limit of low frequencies, $\vec{q} \to \vec{0}$, where $\omega_i \to 0$, the ratio of c_L and c_T can be written as

$$\begin{aligned}
\frac{c_L}{c_T} &= \frac{\left.\frac{\partial \omega_L}{\partial \vec{q}}\right|_{\vec{q}=\vec{0}}}{\left.\frac{\partial \omega_T}{\partial \vec{q}}\right|_{\vec{q}=\vec{0}}} = \left.\frac{\lim_{\Delta\vec{q}\to\vec{0}} \frac{\Delta\omega_L}{\Delta\vec{q}}}{\lim_{\Delta\vec{q}\to\vec{0}} \frac{\Delta\omega_T}{\Delta\vec{q}}}\right|_{\vec{q}=\vec{0}} \\
&= \left.\lim_{\Delta\vec{q}\to\vec{0}} \frac{\frac{\Delta\omega_L}{\Delta\vec{q}}}{\frac{\Delta\omega_T}{\Delta\vec{q}}}\right|_{\vec{q}=\vec{0}} = \left.\lim_{\Delta\vec{q}\to\vec{0}} \frac{\Delta\omega_L}{\Delta\omega_L}\right|_{\vec{q}=\vec{0}} \\
&= \lim_{\vec{q}\to\vec{0}} \frac{\omega_L(\vec{q})}{\omega_T(\vec{q})}.
\end{aligned} \tag{6.11}$$

Since Cs polarizes upon adsorption, the interaction potential may be modelled as a dipole potential:

$$\Phi = \frac{1}{4\pi\varepsilon_0} \sum_{k\neq\ell} \frac{p^2}{|\vec{r}_k - \vec{r}_\ell|^3}, \tag{6.12}$$

where p is the dipole of the adsorbed Cs adatoms. The coupling constants are

$$\begin{aligned}
\frac{\partial^2\Phi}{\partial\vec{r}_m\partial\vec{r}_n} &= \frac{3p^2}{4\pi\varepsilon_0} \sum_{k\neq\ell} \left(\frac{5}{|\vec{r}_k - \vec{r}_\ell|^7}(\vec{r}_k - \vec{r}_\ell)\otimes(\vec{r}_k - \vec{r}_\ell) - \frac{1}{|\vec{r}_k - \vec{r}_\ell|^5} 1\otimes 1\right)\times \\
&\quad \times(\delta_{kn} - \delta_{\ell n})(\delta_{km} - \delta_{\ell m})
\end{aligned} \tag{6.13}$$

where $\vec{a}\otimes\vec{b}$ denotes the dyadic product of $\vec{a}$ and $\vec{b}$[1] and $1\otimes 1$ the unity matrix. To calculate the dynamical matrix D, it is convenient to choose the atom with $\vec{r}_{n=0} = \vec{0}$ as the point of reference. Evaluating the sums in (6.13) and (6.8), one obtains

$$D = \frac{3p^2}{2\pi\varepsilon_0 M} \sum_{\ell\neq 0} \left\{5\frac{\vec{r}_\ell\otimes\vec{r}_\ell}{|\vec{r}_\ell|^7} - \frac{1\otimes 1}{|\vec{r}_\ell|^5}\right\}\left(1 - e^{i\vec{q}\cdot\vec{r}_\ell}\right) \tag{6.14}$$

[1] $\vec{a}\otimes\vec{b}$ results in a matrix with $(\vec{a}\otimes\vec{b})_{ij} = a_i b_j$.

Choosing the numbering of the atoms such that $\vec{r}_{-\ell} = -\vec{r}_\ell$, (6.14) transforms to

$$D = \frac{3p^2}{\pi\varepsilon_0 M} \sum_{\ell>0} \left\{ 5\frac{\vec{r}_\ell \otimes \vec{r}_\ell}{|\vec{r}_\ell|^7} - \frac{1 \otimes 1}{|\vec{r}_\ell|^5} \right\} (1 - \cos(\vec{q} \cdot \vec{r}_\ell)) \tag{6.15}$$

Since the dynamical matrix (6.15) is two-dimensional, its eigenvalues ω_i^2 can be expressed by its trace[2] and its determinant:

$$\omega_{1,2}^2 = \frac{1}{2} \mathrm{tr}\, D(\vec{q}) \pm \sqrt{\frac{1}{4}(\mathrm{tr}\, D(\vec{q}))^2 - \det D(\vec{q})} \tag{6.16}$$

$$= \frac{1}{2} \mathrm{tr}\, D(\vec{q}) \left\{ 1 \pm \sqrt{1 - 4\frac{\det D(\vec{q})}{(\mathrm{tr}\, D(\vec{q}))^2}} \right\}. \tag{6.17}$$

c_L/c_T is therefore (see (6.11))

$$\frac{c_L}{c_T} = \frac{\sqrt{1 + \sqrt{1 - 4\frac{\det D(\vec{q})}{(\mathrm{tr}\, D(\vec{q}))^2}}}}{\sqrt{1 - \sqrt{1 - 4\frac{\det D(\vec{q})}{(\mathrm{tr}\, D(\vec{q}))^2}}}} \tag{6.18}$$

Taking into account only nearest-neighbor–interactions, trace and determinant become for a hexagonal ordering of atoms

$$\mathrm{tr}\, D(\vec{q}) = \frac{3p^2}{\pi\varepsilon_0 M d^5} \sum_{\ell>0} 3(1 - \cos(\vec{q} \cdot \vec{r}_\ell)) \tag{6.19}$$

$$\det D(\vec{q}) = \left(\frac{3p^2}{\pi\varepsilon_0 M d^5} \right)^2 \left\{ -4 \sum_{\ell>0} (1 - \cos(\vec{q} \cdot \vec{r}_\ell))^2 + \right.$$
$$\left. + \frac{43}{8} \sum_{\ell \neq m} (1 - \cos(\vec{q} \cdot \vec{r}_\ell))(1 - \cos(\vec{q} \cdot \vec{r}_m)) \right\} \tag{6.20}$$

where d is the nearest-neighbor–distance. It can be shown that for small $\vec{q}$, $\det D/(\mathrm{tr}\, D)^2 = 11/144$, independent of the direction of $\vec{q}$. With (6.18) and (6.17), this results in $c_L/c_T = \sqrt{11}$. Both c_L and c_T depend on the dipole moment p and the nearest-neighbor-distance d, but since in (6.3) only the ratio of c_L and c_T is important, the actual values for p and d of Cs atoms on Cu(111) are not required. Additionally, numerical calculations showed that including interactions ranging further than the nearest neighbor do not change the result significantly.

θ is plotted according to Eq. (6.3) in Fig. 6.4 as a full line. Although the trend is reproduced correctly (the larger the misfit, the larger the angle of rotation), the model is not able to account for our experimental observation that rotation starts not until a certain misfit is exceeded. This shortcoming of the model close to commensurate phases is known. A similar effect was reported for

[2] $\mathrm{tr}(D_{ij}) = \sum D_{ii}$

Figure 6.5: Constant-current STM image of Cu(111)-p(2×2)Cs at 9 K. (124 nm× 124 nm, V = 250 mV, I = 0.2 nA).

K and Rb adsorbed on Ag(111) [105] and is attributed to the fact that near commensurate phases, where the misfit is small, the domains become larger and more adatoms are nearly in phase with substrate atoms. This leads to a stronger interaction of substrate and adlayer, locking the adlayer to the substrate orientation. A theoretical model developed by Shiba [119,120] takes this into account and predicts that for a small misfit the domain walls of the layer remain aligned to a symmetry direction of the layer up to a critical misfit. For larger misfits, the domain walls become too weak to keep the alignment, and the layer is rotated versus the substrate.

6.2.3 Saturation coverage: $\Theta = 0.25$ ML

At 0.25 ML the room temperature LEED pattern reveals a clear (2×2) superstructure. A typical constant-current STM image of this surface at 9 K is displayed in Fig. 6.5. The adsorption layer is characterized by a Cs film revealing an increased number of imperfections compared to lower coverages. These imperfections, which appear as dark indentations at the given tunneling voltage exhibit a variety of sizes and shapes. The peculiar structure of the Cs adsorbate film as seen in constant-current STM images of Cu(111)-p(2×2)Cs can be explained in terms of island growth. As mentioned in the introduction alkali metal adsorption on metal surfaces goes hand in hand with the creation of dipole moments due to charge transfer processes. At low coverages the dipole-dipole interaction leads to a repulsive Cs-Cs interaction. With increasing coverage, the Cs adatoms depolarize and the repulsion decreases [100]. Reaching a sufficiently high coverage the interatomic distance is small enough to favor metallic bonds [140] and small islands are formed. With increasing size the islands eventually come close to each other and coalesce, thereby leaving behind unoccupied substrate areas.

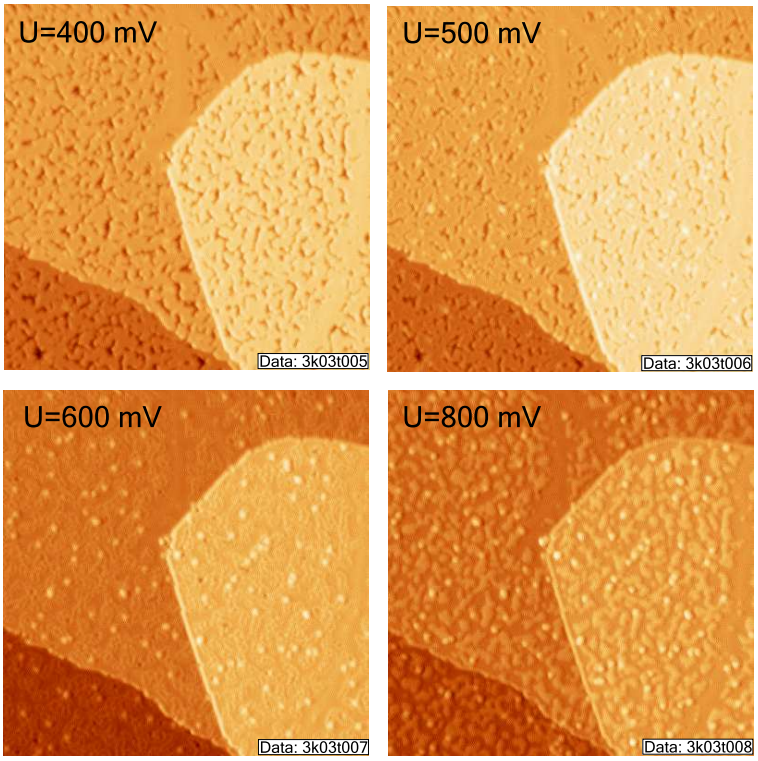

Figure 6.6: Series of constant-current STM images of Cu(111)-p(2 × 2)Cs acquired at the indicated voltages (116 nm × 116 nm, 200 pA).

Interestingly, using tunneling voltages higher than 500 mV the indentations change their apparent height and are imaged as protrusions. In Fig. 6.6 a series of constant-current STM images of the same scan area, acquired at the indicated voltages, is presented. At 400 mV the appearance of the surface is similar to the one shown in Fig. 6.5. Starting from 500 mV protrusions occur at some of the boundaries of the indentations. At 600 mV most of the structures formerly imaged as indentations now appear at the same apparent height as the terraces they are embedded in. Additionally, all of the structures are surrounded by a narrow line, which reveals an increased apparent height. Tunneling voltages greater than 800 mV give rise to constant-current STM images like the one shown at the bottom of Fig. 6.6. Nearly all of the imperfections are now imaged as protrusions. Compared to the top constant-current STM image of Fig. 6.6 the contrast is reversed.

To understand the contrast reversal of the defect structures in the (2×2) Cs superlattice we performed tunneling spectroscopy in the center of the defect structures and on the closed Cs layer. The results are shown in Fig. 6.7. The common feature in both spectra is the spectroscopic signature of the quantum well state which appears as a sharp onset of the dI/dV signal close to zero sample voltage. While the spectrum on the Cs layer decays for energies higher than the quantum well state binding energy, the spectrum acquired inside the defect increases monotonically. As a consequence, for energies greater than the

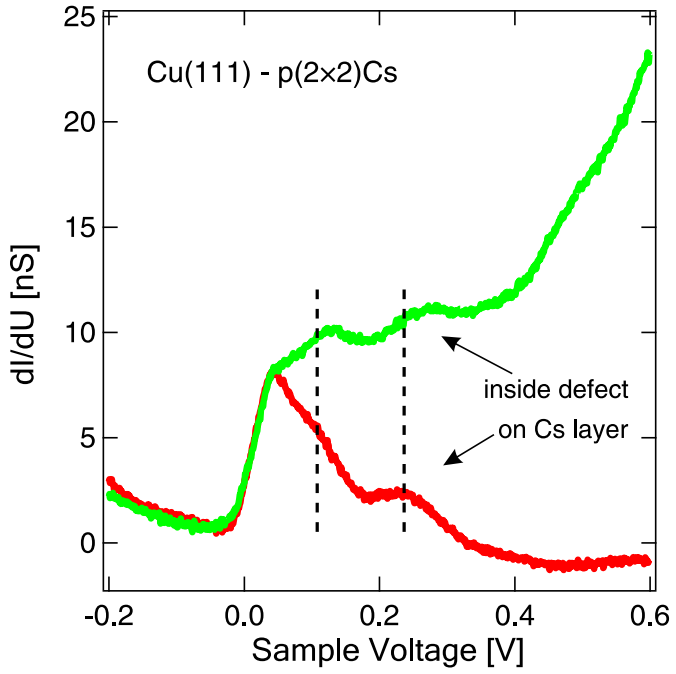

Figure 6.7: Spectra of the differential conductivity inside the defect structures and on the Cs layer of Cu(111)-p(2×2)Cs. Dashed lines indicate additional spectroscopic features, which are tentatively ascribed to backfolded Cu states. The tunneling gaps for both spectra were set at $V = -0.6\,V$ and $I = 0.5\,nA$.

quantum well state binding energy, the defect structures reveal a higher local density of states than the adjacent Cs film. We attribute the contrast reversal to this difference in the local density of states. Two questions arise: (i) Why does the spectroscopic signature of the quantum well state appear both on the Cs layer and inside the defect structures and (ii) what is the origin of the additional local density of states inside the defect structure? Definitive answers to these questions are not available at present. A potential reason explaining these phenomena is given below. The quantum well state wave function is confined to the Cs layer. It is reasonable to assume that the boundaries of the Cs layer, which surround the defect structures do not act as hard walls with regard to the reflection of the quantum well state wave function. Consequently, parts of the wave function are transmitted from the Cs layer into the defect structures. Tunneling spectroscopy inside the defect structures would then be able to detect the quantum well state, as observed experimentally. Further, additional local density of states can be expected when the quantum well state wave function is confined to the defect structures. Comparable experiments were performed on Ag(111) where the electronic surface state which is hosted by this surface was confined to Ag adatom islands [88] and vacancy islands [167]. Here the islands are quantum boxes confining the Ag(111) surface state giving rise to quantized energy levels, which appear as additional local density of states in spectra of the differential conductivity.

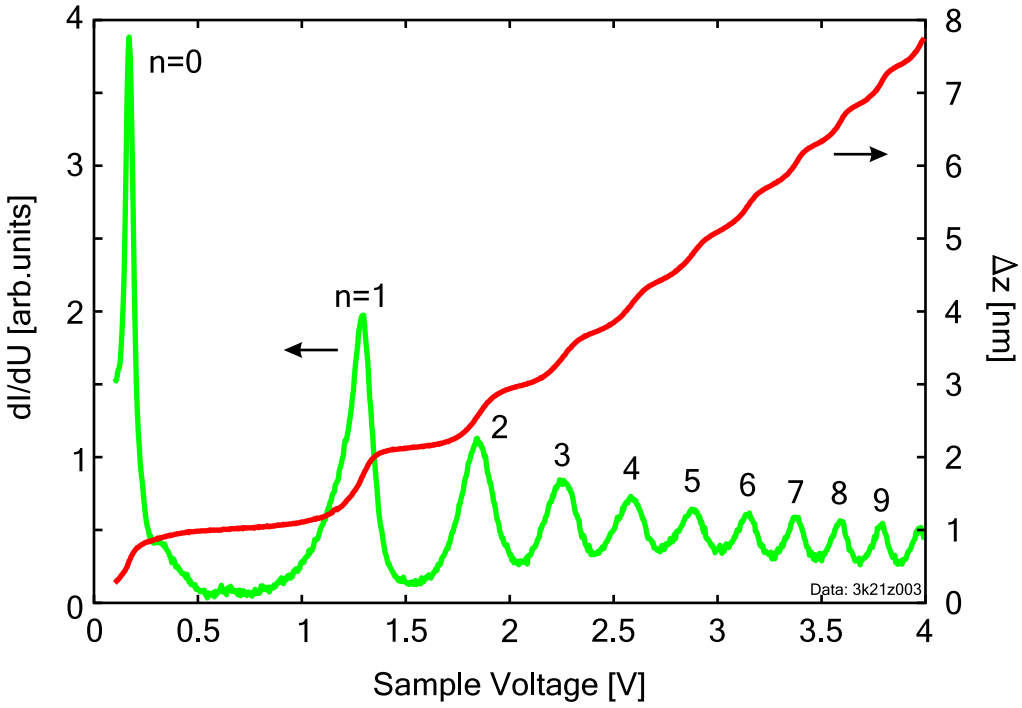

Figure 6.8: $z(U)$-spectroscopy on Cu(111)-Cs at a coverage of ≈0.23 ML. The $z(U)$-spectrum and the dI/dU-spectrum were recorded simultaneously at a constant current of $I = 0.2$ nA. The peaks of the dI/dU-spectrum concur approximately with the points of maximum slope of the $z(U)$-spectrum. The peaks/onsets are attributed to new states appearing at the corresponding energies.

6.3 Electronic Properties

6.3.1 $z(U)$-characteristics

Different types of spectroscopy were carried out to examine the electronic structure of Cu(111)-Cs. Fig. 6.8 shows a typical $z(U)$-spectrum along with a simultaneously acquired dI/dU-spectrum for a coverage of 0.18 ML. The $z(U)$-spectrum shows distinct step-like onsets. Between these onsets, there are flat areas whose slope increases gradually with voltage. The dI/dU-spectrum clearly shows peaks at the voltages where the onsets appear in the $z(U)$-spectrum. The peaks in the dI/dU-spectrum are approximately at the same position as the maximum slope of the onsets of the $z(U)$-curve. Since $z(U)$-spectra are acquired in constant-current–mode, and the current is the integral of the density of states (see Chapter 2.3), the onsets mark the appearance of new states in the LDOS, which lead to a strong increase in the current. To keep the current constant, the tip is retracted, resulting in the onsets.

To identify the nature of the states, their binding energies are plotted in Fig. 6.9 in dependence on the index number as labelled in 6.8. The states with index

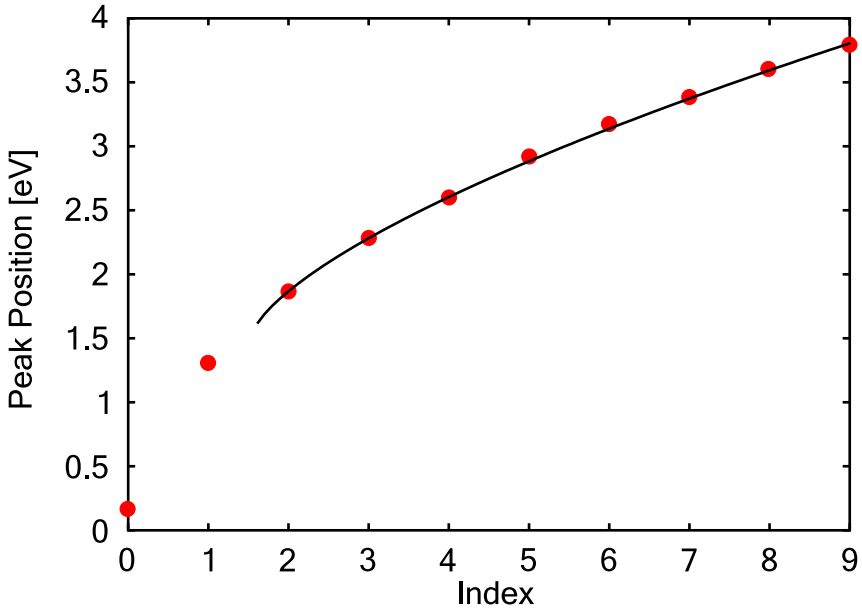

Figure 6.9: Distribution of the binding energies of the states detected by $z(U)$-spectroscopy in Fig. 6.8. The binding energies of the states labelled $n = 2 \ldots 9$ show a dependence on the index that is typical for field-emission resonances (solid line), they are therefore identified as such. The states with index $n = 0, 1$ do not fit in this dependence, they are therefore identified as quantum well states.

$n = 2 \ldots 9$ show a $n^{2/3}$-dependence, which is typical for field-emission resonances. The appearance of these features in the $z(U)$-spectrum is therefore attributed to field-emission resonances. The states with index $n = 0, 1$ do not fit into this scheme and are identified as quantum well states.

In summary it is easy to detect the energetic position and the origin of states using $z(U)$-spectroscopy.

6.3.2 dI/dU-spectroscopy

Scanning tunneling spectroscopy was performed at different places on samples with coverages ranging from 0.05 ML to 0.25 ML. After identifying the quantum well states, spectroscopy was focussed on their examination. Examples of spectra at different coverages are shown in Fig. 6.10. The evaluation of the line shape leads to the observation that with increasing coverage the binding energy of the QWS decreases and the width of the onset gets smaller. The binding energies in dependence on the coverage are plotted in Fig. 6.11 along with data obtained in two-photon photoemission (2PPE) experiments by Bauer et al. [168, 169] and by inverse photoemission spectroscopy (IPES) by Arena et al. [143]. Both photoemission experiments were done at room temperature. The photoemission data and the STS data match to give a continuous curve, as indicated by the dashed line, showing a monotonic de-

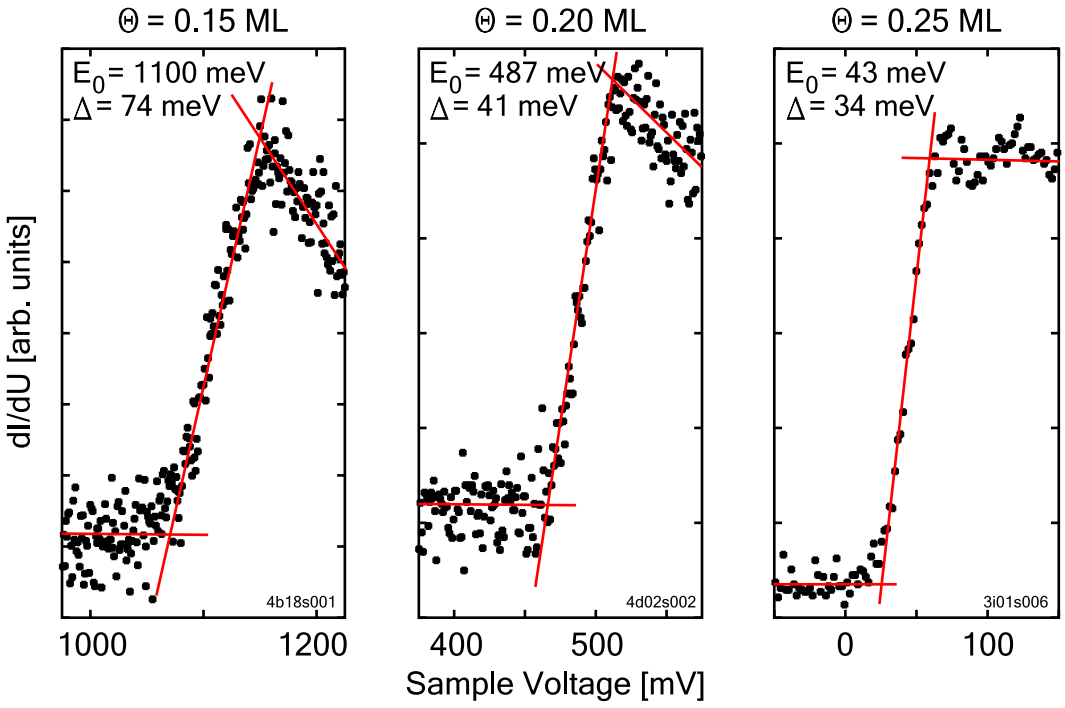

Figure 6.10: Scanning tunneling spectra of the QWS obtained on Cu(111)-Cs at different coverages. The evaluation is done using the line shape analysis described in Chapter 5.1. Two trends are visible: with increasing coverage, the binding energy decreases, and the width Δ of the onset gets smaller.

crease of binding energy with increasing coverage. At the point where the two data sets touch, which is near the coverage corresponding to the $(\sqrt{7} \times \sqrt{7})$-superstructure, there appears to be a bend. However, since there are no error bars for the photoemission data, it can not be decided whether this bend is significant or not.

The decrease of the binding energy is in accordance with measurements on other systems as Cu(111)-Na [139, 145], Be(0001)-Li [146], and Al(111)-Cs, Na, K [147] and can be explained with the following model: For low coverages, the atoms are well separated, and the atomic orbitals do not overlap. The features observed in photoemission experiments are therefore attributed to unoccupied atomic orbitals of the Cs, namely the 5d-orbitals [143], or a hybrid of 6s- and $6p_z$-orbitals, or of $5d_z^2$- and $6p_z$-orbitals [168]. The influence of the dipole potential of neighboring atoms leads to the reduction of the energy of the adsorbate levels [170], which leads to an almost linear decrease of the binding energy for small coverages. With increasing coverage, the atomic orbitals overlap, the layer becomes gradually more metallic [140, 170], and the atomic orbitals transform into the QWS. Because of the metallic character of the layer, the influence of the dipole potential becomes weaker, and the binding energy becomes almost independent of the coverage [170].

In Fig. 6.12, the experimental width of the onset is shown in dependence on the

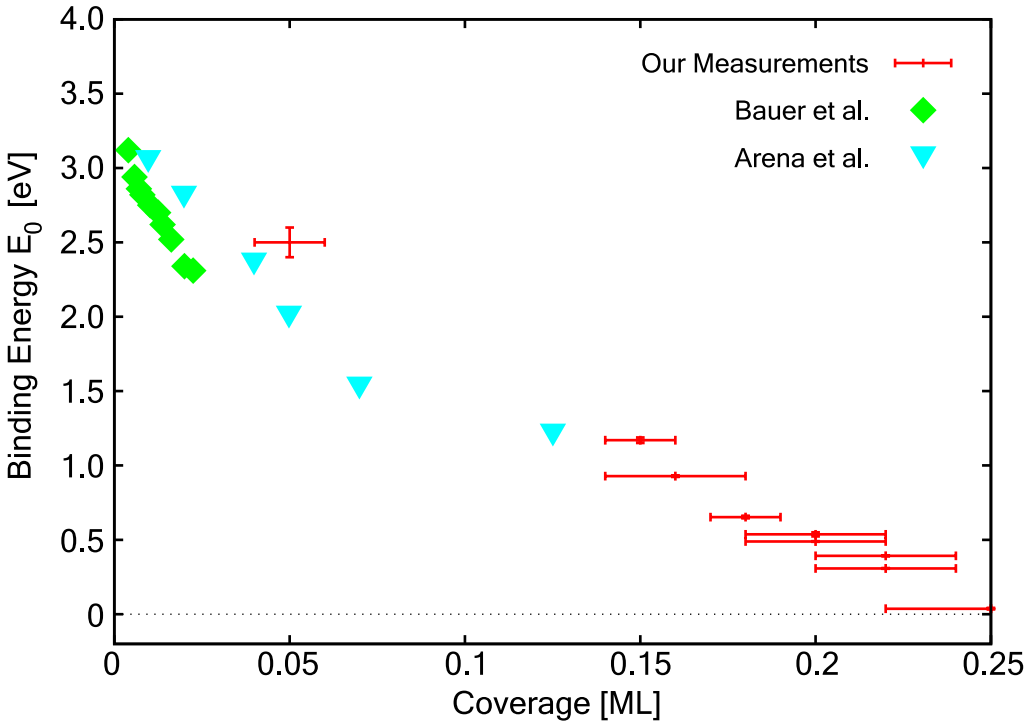

Figure 6.11: Binding energy of the QWS of Cu(111)-Cs depending on the coverage. Included in the graph are: Data obtained by own measurements at 9 K (with error bars), data by M. Bauer et al. obtained by 2PPE (diamonds) [169], and by D. Arena et al. obtained by IPES (triangles) [143] (both at room temperature). The error bars of the binding energy is the standard deviation of more than 10 spectra in each case; the error bars of the coverage consists of the uncertainty of the piezo constants (for atomically resolved films), and uncertainties of the deposition rate measured with the quartz balance. For the value at 0.05 ML only one $z(V)$-spectrum could be evaluated, the error bar of the binding energy is therefore an estimation. The dashed line serves to guide the eye.

coverage. The experimental width increases with increasing binding energy, which can be explained as follows: For an excited electron to decay, there have to be unoccupied final states. For larger excitation energies, there are more unoccupied states, and therefore the probability for the electron to decay is larger. The fact that the experimental width of $\Delta \approx 28$ meV for the lowest binding energy of 40 meV is comparable to the experimental width at a binding energy of 400 meV in the case of Cu(111)-p(2×2)Na [49] leads to the conclusion that the contribution of electron–electron coupling to the lifetime is not large, since $\Gamma_{e-e} \propto (E - E_F)^2$ for $E \approx E_F$ (see (4.40)). A recent calculation [87] indeed revealed a large influence of electron–phonon coupling and of electrons coupling to SBZ back folded states, but only a small influence of electron–electron coupling with SBZ back folding for the QWS in the p(2×2)-superstructure.

For the saturation coverage (Θ=0.25 ML), an additional occupied state has

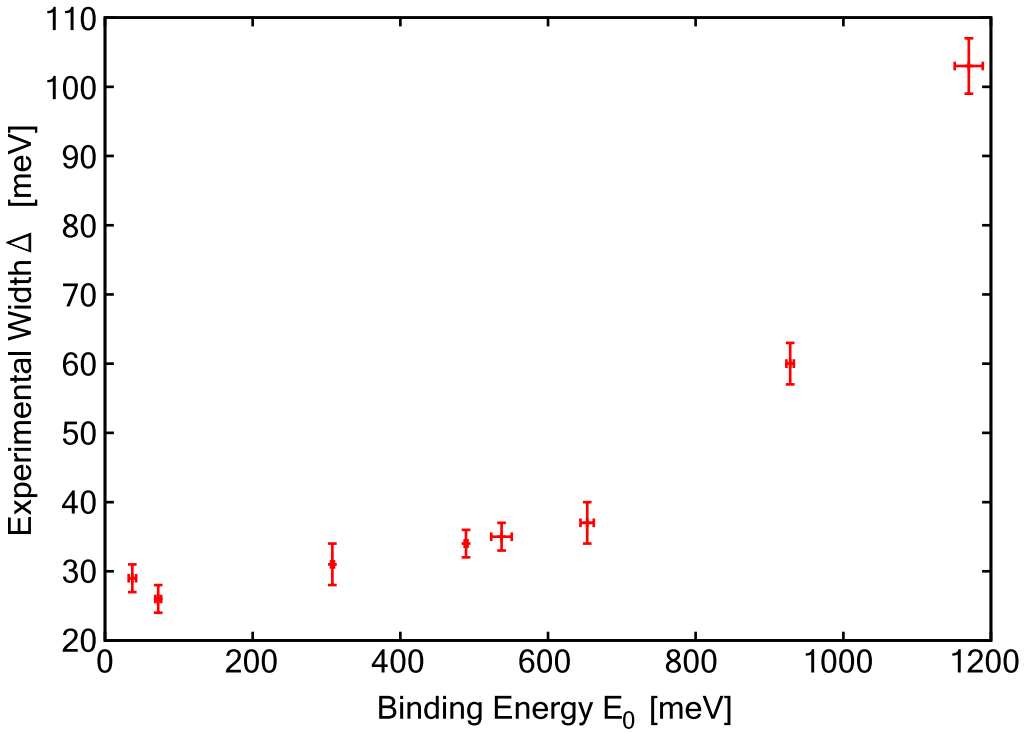

Figure 6.12: Experimental width in dependence on the binding energy for Cu(111)-Cs. Error bars are the standard deviation obtained from more than 10 spectra in each case. The dashed line is a parabolic fit according to Eq. 4.40.

been detected. Fig. 6.13 shows a typical spectrum containing the QWS at $E = 15\,\mathrm{meV}$ and the additional state, labelled *SS*, at $E_{SS} = -440\,\mathrm{meV}$ with a width of $\Delta_{SS} = 63\,\mathrm{meV}$. The binding energy of the state detected fits well the binding energy of the surface state of the clean Cu(111) surface, which is located at $E_0 = -445\,\mathrm{meV}$ with an experimental width of $\Delta_0 = 30\,\mathrm{meV}$ [84]. However, the observation that the binding energy of the surface state does not shift significantly with Cs coverage is in contrast to findings by Lindgren et al. [171], who report on a shift of the binding energy of the surface state with coverage and find that it is located at $\approx -800\,\mathrm{meV}$ for the saturation coverage.

6.3.3 Dispersion relations

Dispersion relations were obtained for coverages of $\Theta = 0.15\,\mathrm{ML}$, $0.20\,\mathrm{ML}$ and $0.23\,\mathrm{ML}$ by recording dI/dU-maps of standing wave patterns of electrons scattered at point defects. Fig. 6.14 shows examples for the coverage of $0.15\,\mathrm{ML}$. In the constant-current images, the defect appears as an indentation with a diameter of $\approx 1\,\mathrm{nm}$, the surrounding area does not show any pattern. In the dI/dU-maps, scattered electron waves form rings around the defect. The ring structure is demonstrated for the case of $U = 1.4\,\mathrm{V}$ by two sketched circles. Since there is no structure in the constant-current images visible, a correction of the dI/dU-maps for the different tip-sample distance according to

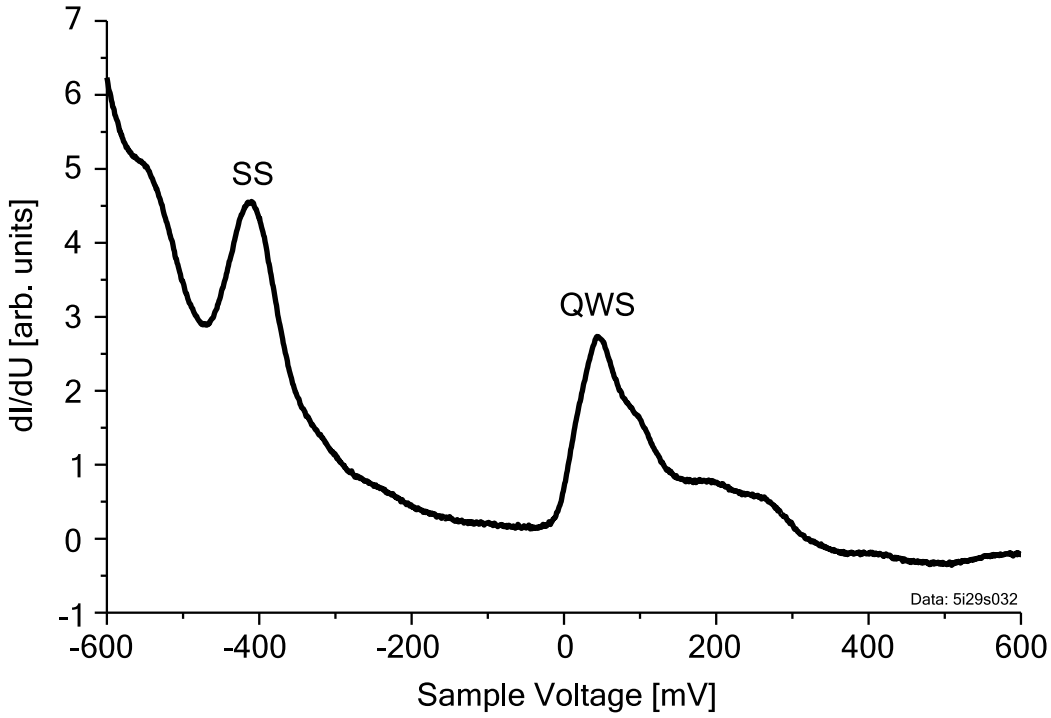

Figure 6.13: dI/dU-spectrum of the QWS and an additional occupied state, labelled *SS* on Cu(111)-Cs. The binding energy of the state SS is $E_{SS} = -440\,\text{meV}$, its width is $\Delta_{SS} = 63\,\text{meV}$.

(2.13) is not necessary.

The periodicity of the rings is the smaller the larger the tunneling voltage. The scattering of electron waves at a point defect is described by [29]

$$\rho(k_{\parallel}, r) \propto 1 + \frac{2}{\pi k_{\parallel} r}\left[\cos^2\left(k_{\parallel} r - \frac{\pi}{4} + \eta_0\right) - \cos^2\left(k_{\parallel} r - \frac{\pi}{4}\right)\right], \tag{6.21}$$

where $k_{\parallel}$ is the component parallel to the surface of the wave vector, η_0 a scattering phase shift depending on the scatterer, and r the distance from the scatterer. (6.21) can be transformed into

$$\rho(k_{\parallel}, r) \propto 1 + \frac{2}{\pi k_{\parallel} r}\cos(2k_{\parallel} r + \eta_0)\sin\eta_0. \tag{6.22}$$

The wave vector $k_{\parallel}$ is therefore

$$k_{\parallel} = \frac{2\pi}{2\Delta r} = \frac{2\pi}{\Delta d}, \tag{6.23}$$

where Δd is the difference in the diameter of two adjacent rings in the wave pattern. Therefore, by measuring the diameters of the rings in the wave pattern, the wave vector corresponding to the scanning voltage, i.e. the energy of the electrons, can easily be obtained. For example, the diameters of the two innermost circles observed at $U = 1.4\,\text{V}$ are $3.98 \pm 0.1\,\text{nm}$ and $5.97 \pm 0.1\,\text{nm}$,

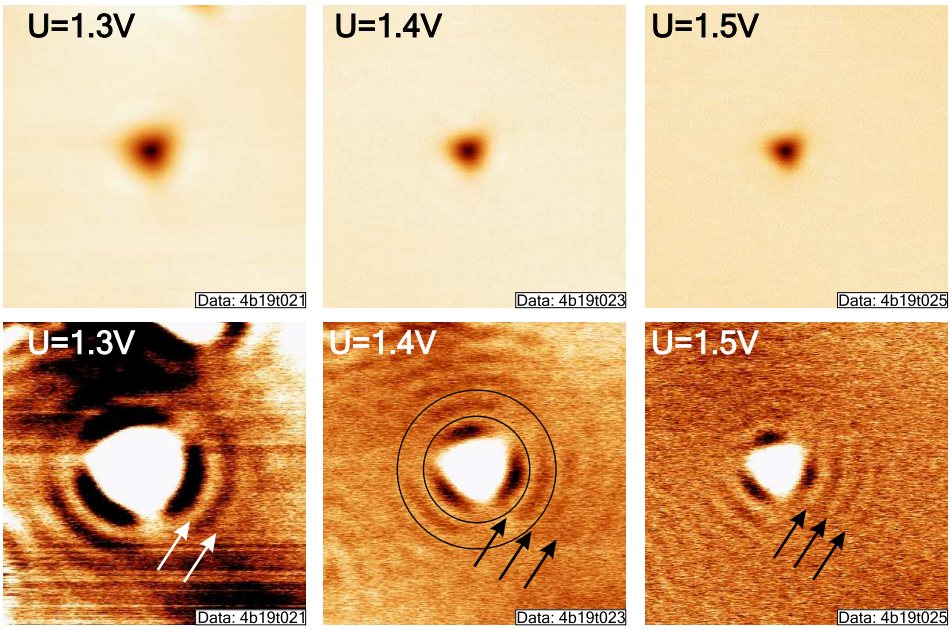

Figure 6.14: Constant-current images and dI/dU-maps of scattering of the QWS at a point defect for different voltages. In the constant-current images, the defect appears as an indentation with a diameter of $\approx$1 nm. In the dI/dU-maps, the contrast has been increased to enhance the visibility of the circular pattern originating from the scattered electron waves; the defect therefore appears to be larger than in the constant-current images. In the dI/dU-map for $U = 1.4\,V$, the sketched circles indicate that the scattered wave forms rings. The periodicity of the rings (marked by arrows) is decreasing with increasing voltage. From this periodicity, the wave vector can be obtained (see text).(Tunneling parameters: I=1 nA, 11.6 nm$\times$11.6 nm)

leading to $k_{\parallel} = (0.32 \pm 0.03)\,\text{Å}^{-1}$. A fit of (6.21) to a line profile taken from the same map leads to the same result, as shown in Fig. 6.15. Since the oscillations are not always clearly visible in the line profiles, the maps were evaluated by measuring the ring diameters.

The resulting dispersion relations for the three coverages examined are shown in Fig. 6.16 together with the binding energies E_0 and effective masses m^* obtained by fitting the dispersion relation $E = E_0 + \hbar^2 k_{\parallel}^2/2m^*$, where m^* is given in electron masses. The error $\Delta k_{\parallel} = 0.02\,\text{Å}^{-1}$ for every data point. The energy value for $k_{\parallel} = 0$ is the binding energy of the QWS as obtained by dI/dU-spectroscopy. The increase of the effective mass with increasing coverage has also been observed in the case of Cu(111)-Na [172]. The tendency suggests that the effective mass depends on the binding energy of the QWS [49].

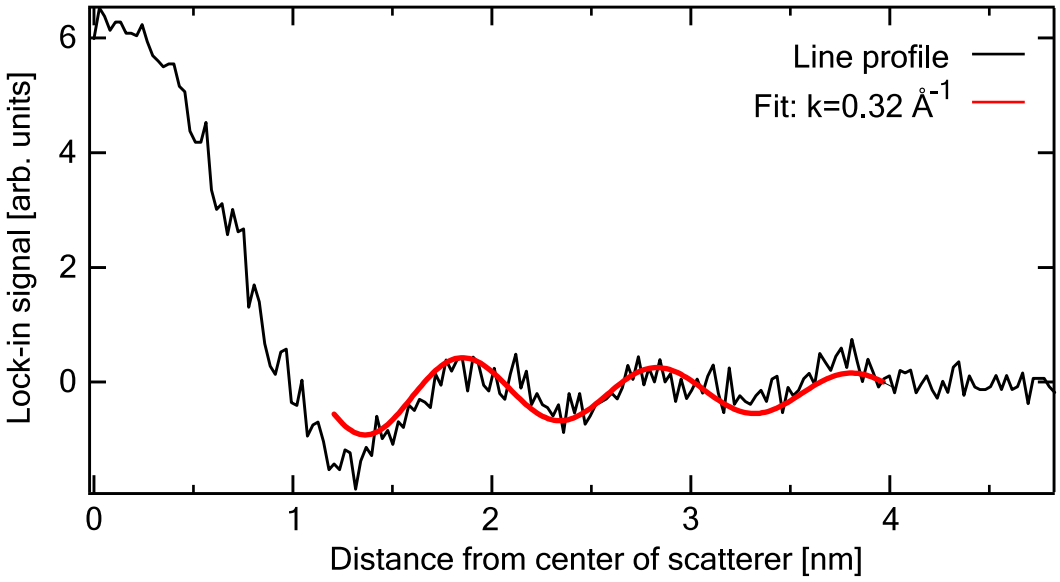

Figure 6.15: Line profile from a scattered QWS with a fit according to (6.21). The result of the fit is $k_{\parallel} = 0.32 Å^{-1}$.

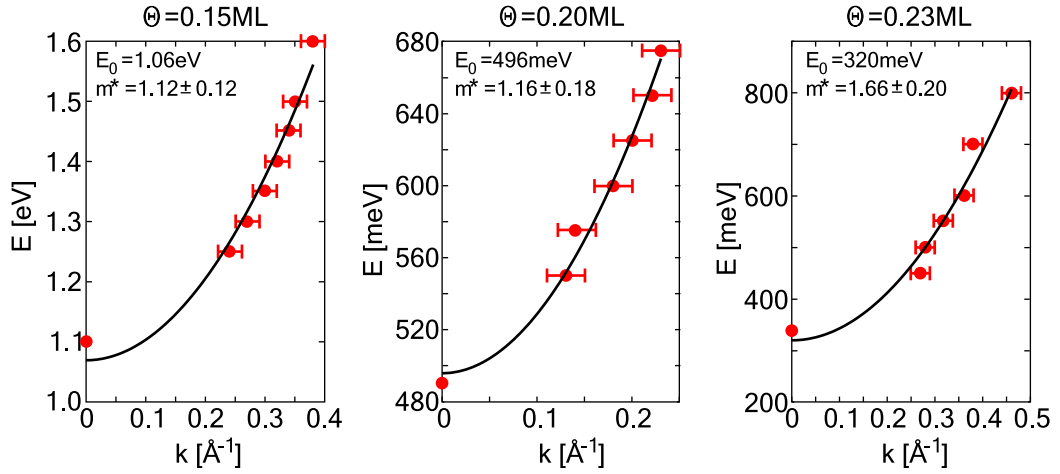

Figure 6.16: Dispersion relations of Cu(111)-Cs for different coverages. The solid lines are parabolic fits according to the model of the free electron gas. The specified values for the binding energy E_0 and the effective mass m^* result from the fits.

Chapter 7

Summary

In this work, an ultra-high vacuum scanning tunneling microscope which can be operated at low temperatures (9 K, 55 K and 80 K) and room temperature has been assembled. The system was extended by three parts: A PC based controller for bake out was developed which is used for every bake out. The STM was modified to allow heating of the sample. This has been tested so far only for sample temperatures in the range of 80 K to 120 K with a base temperature of 80 K. Calculations to predict the heating power to attain elevated temperatures for different base temperatures were performed. Additionally, a new vibration isolation stage for the cryostat was designed, mounted and set into operation successfully.

The first system examined here is Cesium on Copper(111) at different coverages. At the coverage of $\Theta = 0.05\,\mathrm{ML}$, the layer forms a $\sqrt{19} \times \sqrt{19}\mathrm{R}23.4^\circ$ superstructure. The ordering extends over large areas of more than $60\,\mathrm{nm} \times 60\,\mathrm{nm}$, which is attributed to stabilization of the layer by surface-state mediated interactions. For coverages $\Theta = 0.15 - 0.25\,\mathrm{ML}$, ordered but incommensurate overlayers were observed. The layer is rotated with respect to the substrate, the angle of rotation depends on the coverage. The dependence is similar to the one found for Ag(111)-Cs [105]. At $\Theta = 0.25\,\mathrm{ML}$, which is the saturation coverage at room temperature, the layer reveals many defects. This is attributed to an island-growth mechanism of the layer where the defects remain when the islands come into contact. The electronic properties of the quantum well state (QWS) in the Cs layer are similar to the properties of the QWS in Na on Cu(111) [49]. The binding energy of the QWS decreases with increasing coverage. The QWS is an unoccupied state even for the saturation coverage of $\Theta = 0.25\,\mathrm{ML}$. The lifetime of excitations of the state increases with increasing coverage, i.e. with decreasing binding energy. The comparatively short lifetime for Cu(111)-p(2×2)Cs and Cu(111)-p(2×2)Na [49] led to the introduction of Brillouin Zone Backfolding as a new lifetime-limiting process [87]. By acquiring $\mathrm{d}I/\mathrm{d}U$-maps, dispersion relations of the QWS for different coverages were obtained. The effective mass increases with increasing coverage as has been reported for Cu(111)-Na [49].

Preliminary results were obtained for Ag(111)-Cs and Si(111)-(7×7)In which are presented in the appendices.

The following two chapters present first experimental data for Ag(111)-Cs and Si(111)-7×7-In. Due to lack of time, these results are *preliminary*.

Appendix A

Cesium on Silver(111)

Clean Ag(111) surfaces were prepared by repeated ion bombardment and anneal cycles. Cleanliness was checked with LEED. Cs was evaporated from a standard Cs dispenser from *SAES Getters*, Italy. The evaporation rate was monitored with a quartz balance. The rate of the quartz balance was later calibrated using atomically resolved STM images. After the preparation at room temperature, the sample was transferred into the STM and cooled to 9 K.

At room temperature, the saturation coverage was found to be near, but smaller than 1/3 ML [105, 173]. In accordance with this, no $\sqrt{3} \times \sqrt{3}$-superstructure of Cs on Ag(111), corresponding to a coverage of 1/3 ML, was observed in our experiments. Fig. A.1 shows a LEED image of the saturation coverage obtained. The hexagonal symmetry of the Ag(111) surface is revealed by intense reflection spots, marked yellow. In the middle between the spots originating from the Ag(111) surface, there are two spots close to each other (red). These spots originate from the Cs adlayer and form a line with the nearest Ag(111) spots. Leatherman et al. concluded from a similar finding for the same system that the structure of the Cs layer is incommensurate, but aligned with the substrate [105]. From the distances of the spots as marked in Fig. A.1b, the coverage can be calculated as follows: Using a printout of Fig. A.1, the distances have been maesured to $R = (6.49 \pm 0.04)$ cm, $r_1 = (3.57 \pm 0.04)$ cm and $r_2 = (3.57 \pm 0.04)$ cm. Since the spots in LEED show the distances in reciprocal space, R corresponds to the reciprocal value of the interatomic distance $d_{Ag-Ag} = 2.89$ Åof adjacent Ag atoms: $R = A/d_{Ag-Ag}$, where is A is a constant that takes the instrumental data into account. Accordingly, $r_1 = A/d_{Cs-Ag,1}$ and $r_2 = A/d_{Cs-Ag,2}$. Combining these equations, one obtains

$$d_i = d \cdot \frac{R}{r_1}. \tag{A.1}$$

From this, we obtain for the coverage ($\Theta_i = (d_{Ag-Ag}/d_{rmCs-Ag,2})^2$)

$$\Theta_1 = (0.20 \pm 0.01)\,\text{ML}, \qquad \Theta_2 = (0.30 \pm 0.01)\,\text{ML} \tag{A.2}$$

It is not possible to decide which of these coverage is the saturation coverage using only the LEED image. Other coverages were determined by calibrating

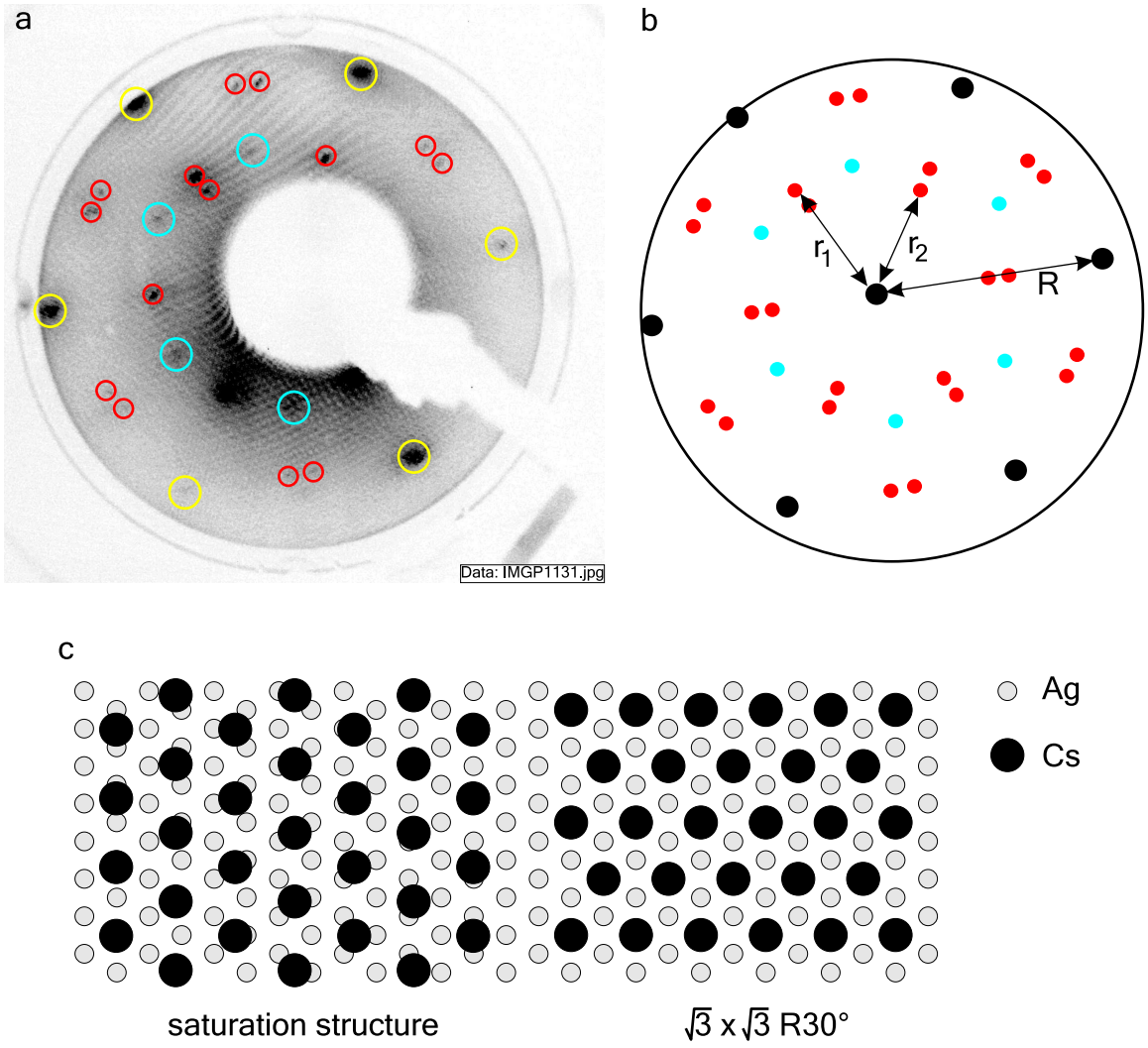

Figure A.1: a) LEED of Ag(111)-Cs at saturation coverage. The yellow circles mark the reflection spots from the Ag(111) surface. The red circles mark the split 2×2 spots. The blue circle marks an additional weak $\sqrt{3} \times \sqrt{3}$ spot. (Electron energy: 56 eV) b) Sketch of the LEED pattern in a). The colors correspond to the colors in a), except that yellow has been changed to black for visibility. The split spots are located where the diffraction spots of a $p(2 \times 2)$ structure would be. The splitting of the spots indicates that the interatomic distance of Cs atoms changed compared to the $p(2 \times 2)$ structure. The marked distances are used to calculate the coverage as described in the text. The result is $\Theta = (0.30 \pm 0.01)$ ML. c) Left: Real-space model of the saturation coverage. The adlayer is aligned with the substrate, but incommensurate. The additional weak spots (blue in a) may indicate the existence of a $(\sqrt{3} \times \sqrt{3})$ structure, sketched on the right.

the quartz balance rate using atomically resolved constant-current images. The highest coverage obtained this way was $\Theta = (0.25 \pm 0.01)$ ML. Therefore it can be concluded that the saturation coverage is $\Theta = (0.30 \pm 0.01)$ ML. This value is in good agreement with $\Theta_{max} = 0.32$ ML for temperatures below room temperature by Leatherman et al. [105].

In the LEED pattern, there are also weak $(\sqrt{3} \times \sqrt{3})$ spots visible, which suggests that domains with a $(\sqrt{3} \times \sqrt{3})$ may also exist. Figure A.1c shows a real-space model of the incommensurate aligned structure at saturation coverage and the $(\sqrt{3} \times \sqrt{3})$ structure.

The development of the structure of Cs on Ag(111) in dependence on the coverage is similar to that of Cs on Cu(111). Fig. A.2 shows constant-current images of Ag(111)-Cs for different coverages. At the coverages 0.12 ML and 0.19 ML, regularly arranged white protrusions can be seen with mutual distances of (8.22±0.08) Åand (6.63±0.07) Å, resectively. The ordering is present even across step edges. In the case of $\Theta = 0.19$ ML, triangular defects are visible which originate from missing protrusions. The protrusions are therefore identified as Cs atoms. With the interatomic distances obtained from these images, the quartz balance was calibrated. The coverage of 0.19 ML is in the range where Leatherman et al. examined the rotational behavior of the adlayer [105]. The value of $14° \pm 2°$ found here corresponds to a coverage of 0.18 ML in their findings, which is in good agreement with the coverage of 0.19 ML obtained from the atomic distances.

In the constant-current images of the layer with $\Theta = 0.19$ ML round defects and circles around the defects can be seen. These defects are located in the Ag(111) surface. Wahlström et al. [157] attributed the occurrence of similar defects on Cu(111) to sulphur from the Cu bulk which diffuse to the surface when annealing the sample too hot. They found similar rings around the defects which they attribute to scattering of the Cu(111) surface state. We therefore conclude that the defects visible in constant-current images of the layer with $\Theta = 0.19$ ML originate from sulphur atoms in the Ag(111) surface, and the rings around them arise from the scattered Ag(111) surface state.

At the coverage of $\Theta = 0.25$ ML, there are many irregularly shaped defects. At saturation coverage, the defects are smaller and round, about a third of the defects is elongated. Atomic resolution was not obtained for these two coverages.

The properties of the QWS were examined in the same way as described in Chapter 6 for the case of Cu(111)-Cs (for details, see there): Using $z(U)$-spectroscopy, the approximate position of the QWS was identified, and then determined more precisely using dI/dU-spectroscopy. Fig. A.3 shows the result for the coverage-dependence of the binding energy of the QWS., which is similar to the dependence found for Cu(111)-Cs. The binding energy decreases as the coverage increases, a dependence that has been found for other systems as Cu(111)-Na [49] and Cu(111)-Cs. The origin of this dependence has been discussed in Chpater 6.

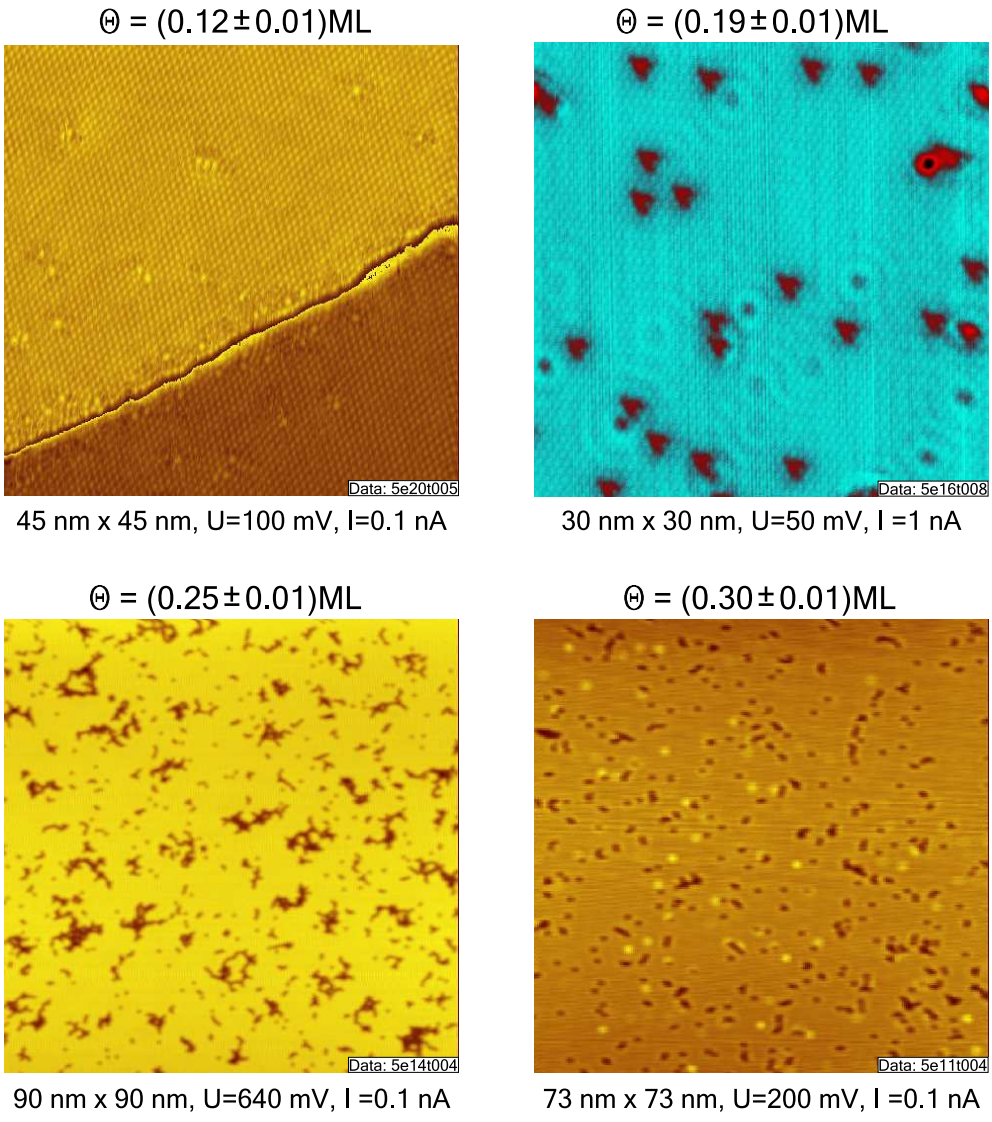

Figure A.2: Constant-current images of Ag(111)-Cs for different coverages.

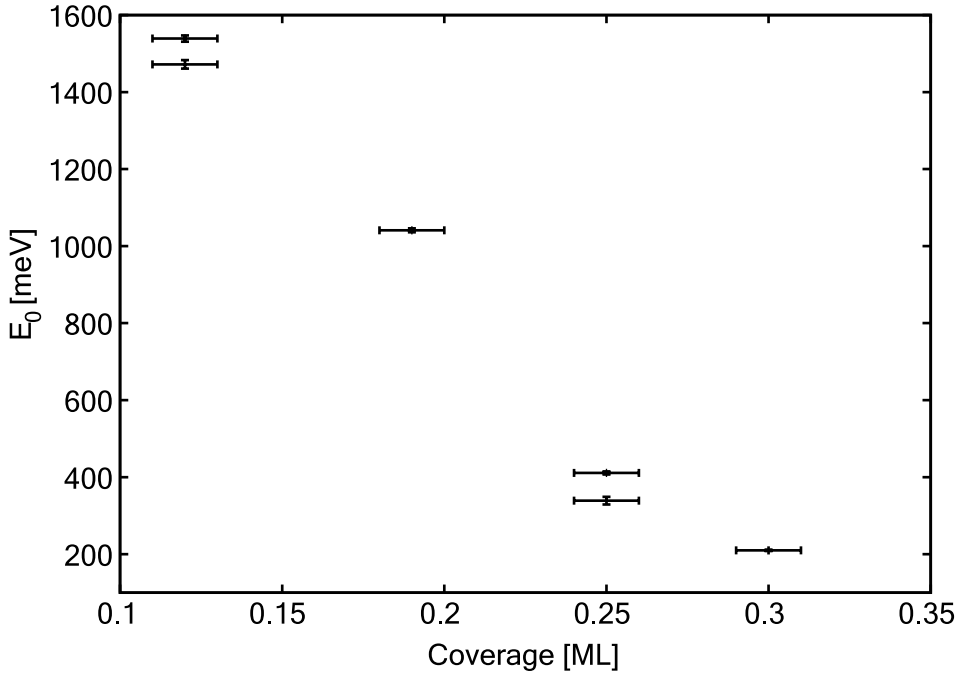

Figure A.3: Binding energy of the quantum well state in dependence on the coverage. The dependence is similar to the one found for Cu(111)-Cs and Cu(111)-Na [49].

Appendix B

Low-Temperature STM on Silicon

Since silicon is the basis of semiconductor industries, its properties are of great interest. In recent years, thin films of Indium on the Si(111)-(7 × 7) surface have been examined to a great extent [174–177]. The superstructures forming depend strongly on coverage and substrate temperature during deposition [176]. For coverages between 0.1 ML and 0.5 ML, a $(\sqrt{3} \times \sqrt{3})$R30° and a $(\sqrt{31} \times \sqrt{31})$ structure form. For larger coverages, a (4×1) structure forms, and for coverages larger than 0.8 ML a (1×1), a $(\sqrt{7} \times \sqrt{3})$ and a (4×4) superstructure arise [176]. While the low-coverage phases are semiconducting, the high-coverage phases are metallic [177]. We examined a superstructure at very low coverage, where no closed film has formed yet.

In the following section, the preparation of Si(111)-(7 × 7) and characterization are described. Then, our results on Indium on Si(111) are presented.

B.1 Silicon(111)-7×7

B.1.1 Preparation of Si(111)-7×7

The preparation of Si(111)-7 × 7 differs considerably from the preparation of Cu or Ag samples. The sample does not need to be sputtered, but is prepared by resistive heating only. The sample was cut from a Si(111) wafer by *Siegert Consulting e.K.*, Aachen, by courtesy of F. Ossendorf, University of Osnabrück. The data of the sample are listed in Tab. B.1. To provide the electrical contacts to the sample, a sample holder was used, which is sketched in Fig. B.1. The sample holder consists of two L-shaped pieces, which are held together by screws and electrically isolated by ceramic spacers. To avoid a connection of the Si sample to the middle part of the holder, there are stacks of 3-4 pieces of Mo spot-welded to the ends of the holder. Clamps which are bent out of Mo foil and spot-welded to the back of the sample holder press the sample onto the Mo sheets.

Dimensions	20 mm×5 mm
Thickness	500-550 µm
Type of doping	p
Dopant	B
Resistivity	5-11 Ω·cm

Table B.1: Data of the Si(111) sample, taken from the data sheet by *Siegert Consulting*, Aachen.

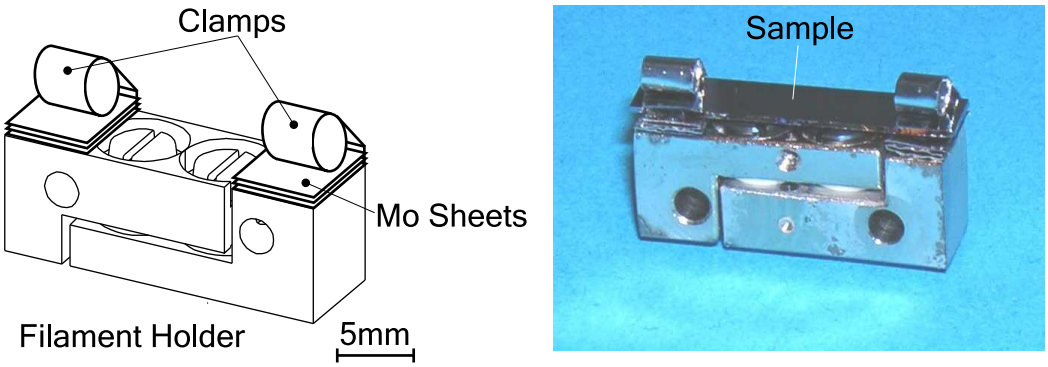

Figure B.1: Sample holder for Si-samples. To two L-shaped parts of the holder are electrically isolated by ceramic spacers. A stack of molybdenum sheets carry the sample and two clamps hold the sample. The mounted sample is shown on the right.

The sheets and clamps of the sample holder are made out of Mo to ensure that the Si sample does not come in contact with any steel parts, since steel contains nickel which contaminates the sample [178]. To avoid any possible contact between the sample and the sample holder, the sample holder was made out of Mo as well. The spot-welding of Mo on Mo turned out to be fairly difficult. In the following, some hints are given for this task.

- The electrode has to be out of tungsten. The point of contact of the electrode has to be very clean, otherwise the electrode will stick to the molybdenum. Since the spot-welding leaves white marks, supposedly of tungsten oxide, on the electrode, the electrode has to be cleaned by filing after every use. [179]

- The voltage leading to good spot-welding results was 8 V. The current was chosen as high as possible.

- The foil sticks best to the bulk Mo when the surface of the bulk is rough. This can be achieved by filing the surface.

- Welding spots must not be put on top of each other. This is important for the stack of Mo sheets: If the welding spot for the last sheet is above a welding spot of a sheet below, the lower spot will break.

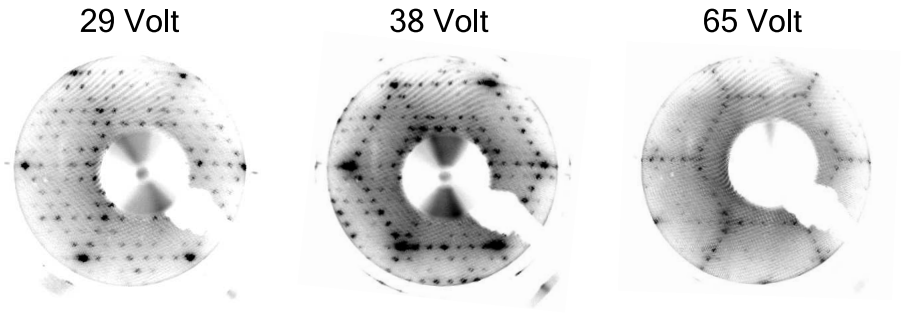

Figure B.2: LEED images of Si(111)-7×7 at different voltages.

Although it is possible to spot weld Mo on Mo, the connection is not very stable. Pieces can fall off the sample holder quite easily when touched. On this account, the main parts of the sample holder were made out of steel in the end. When using one of these sample holders, one must take care that the sample does not touch the steel parts because this will lead to carbon contamination. For the same reason, plastic tweezers must be used when mounting a sample.

The sample holder is degassed by mounting a sample (an old one is sufficient) and applying 3.0 A for several hours.

Below are the instructions to prepare the Si(111)-7×7 reconstruction [180, 181].

- New samples are degassed by heating them to ~650-700°C for 2 h. For our samples, a current of 0.5 A was used.
- To clean the sample, it has to be heated to 1200°C. To avoid a strong increase of the pressure, the temperature is increased by a procedure called 'flashing': Choose and preset a current which is some 0.1 A higher than before. Then increase the voltage rapidly till the preset current is reached. Keep the current up for 5 s, then turn it off fast. If the current stays below 10^{-7} Pa during this flash, the current can be increased, otherwise it has to be used once more. This procedure is repeated until the sample reaches a temperature of 1200°C.

  For the samples used here, a current of ~6 A was sufficient for this.
- After flashing the sample to 1200°C one last time, reduce the current so that the sample has a temperature of 900°C. (Check the current needed before!) Now decrease the current slowly so that the sample is cooled to 700°C within two minutes. This produces the 7 × 7-reconstruction.
- When reaching 700°C, turn off the current and let the sample cool to room temperature.

If the sample preparation was successful, LEED shows a typical, voltage dependent pattern, which is shown in Fig. B.2.

A sample can be used several times, but has to be changed when the surface gets a white shine or a lot of defects become visible.

B.1.2 Scanning Tunneling Spectroscopy on Si(111)

A typical constant-current image of the Si(111)-7×7 surface is shown in Fig. B.3. The sample shows the characteristic reconstruction with only few

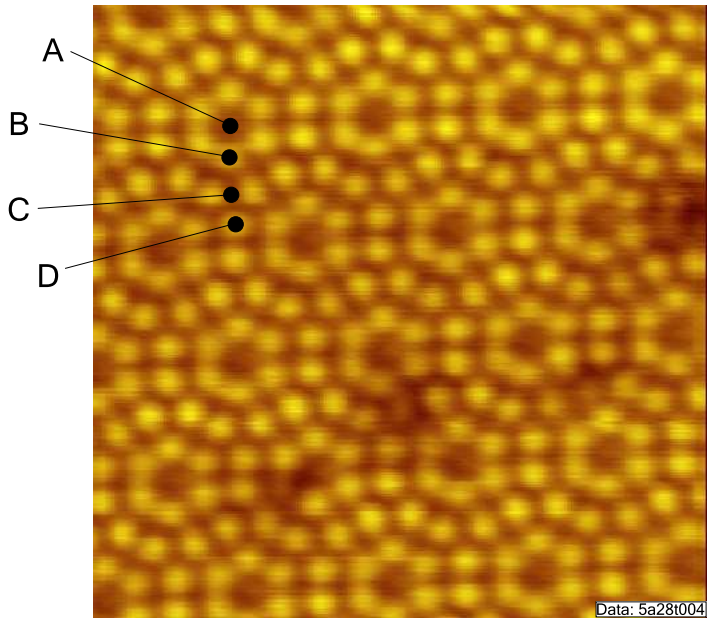

Figure B.3: The 7×7-reconstruction of Si(111). The labels A, B, C, D mark the positions where spectra were acquired. The spectra are shown in Fig. B.4. (10 nm×10 nm; $U = 4.0$ V, $I = 0.1$ nA)

defects originating from missing atoms. Spectra were recorded on this surface at different atomic positions, label as A, B, C, D in Fig. B.3. A set of spectra obtained at these positions with the same parameters is shown in Fig. B.4. The $I(U)$- as well as the dI/dU-spectra do not depend on the position they were acquired. Furthermore, the $I(U)$-spectra show the behavior the $I - V$- characteristics of a diode. In accordance with the vanishing conductivity in the $I(U)$-curve is the observation that when using sample voltages below ~1 V, the tip is moved towards the sample by several Å, and the surface is destroyed afterwards, thus leading to the conclusion that the tip is in contact with the surface.

The behavior of the $I(U)$-curves has been observed by Avouris and co-workers [182] and can be explained by means of a Schottky-barrier. The band structure of the Schottky-barrier is sketched in Fig. B.5. When the metallic tip and the p-doped semiconductor sample are separated, their vacuum levels are the same, but their Fermi levels differ by ΔE (Fig. B.5a). When metal and semiconductor come in contact, this difference is retained at the junction while the Fermi levels equalize at the same time. The valence and the conduction band of the semiconductor will bend to fulfill both requirements (Fig. B.5b). When a positive voltage is applied to the semiconductor, its Fermi level is lowered and electrons can move from the metal to the semiconductor, and the junction

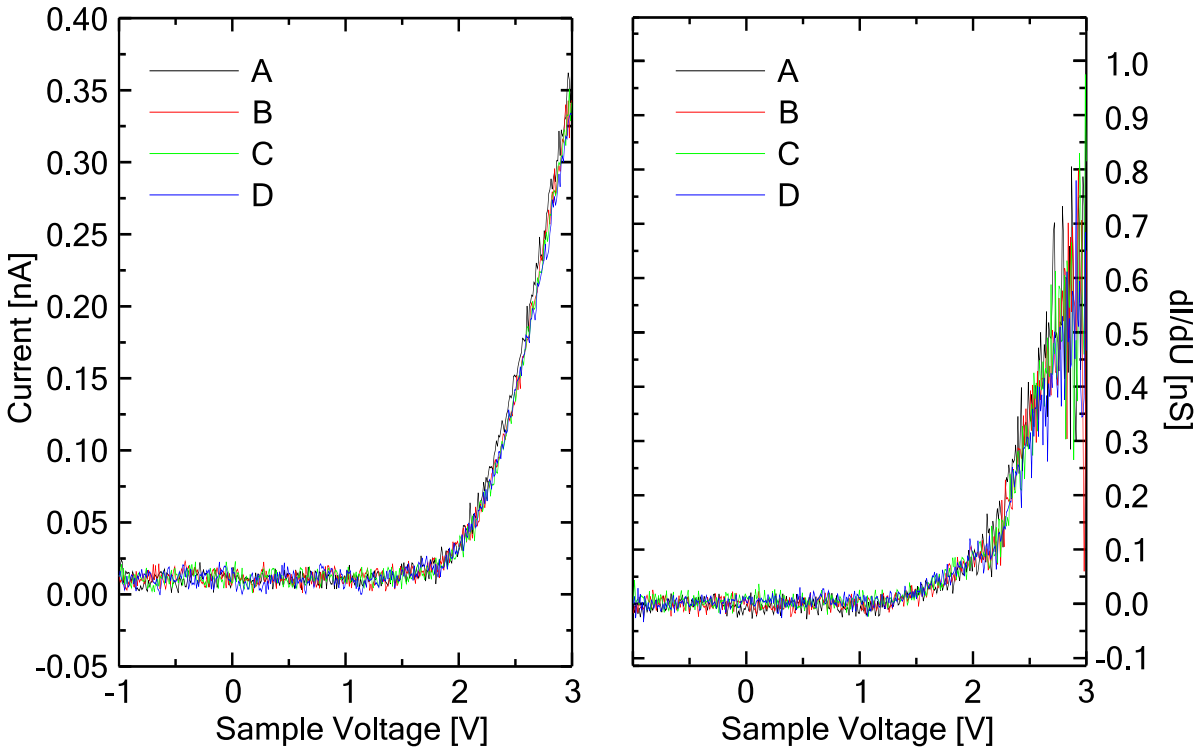

Figure B.4: Spectra acquired on Si(111) at 9 K. a) I(U)-spectra, b) dI/dU-spectra. A, B, C, D refer to the positions marked in Fig. B.3. The feedback loop was frozen at U=3.0 V, I=0.1 nA, and the tip was moved towards the sample by Δz=7 Å before acquiring the spectra to obtain a larger signal.

is conductive (Fig. B.5c). When the bias is reversed (negative voltage to the semiconductor), the Fermi level is raised, and electrons cannot move from the metal to the semiconductor, the junction is insulating (Fig. B.5d).

B.2 Indium on Silicon(111)

Indium was evaporated onto the Si(111)-7 $\times$ 7 surface from a ceramic crucible which was heated and supported by a tungsten filament. The evaporator is shown in Fig. B.6. The sample was at room temperature during deposition. A large-scale constant-current image of Si(111)-In after an exposition of the the sample to In for 15 s is shown in Fig. B.7a. On the surface, triangular protrusions are visible which are ordered hexagonally. The close-up view in Fig. B.7b shows that each triangle consists of three protrusions which lie on top of Si atoms. These protrusions are identified as In atoms. The model in Fig. B.7c shows the adsorption geometry in more detail: In each unit cell of the Si(111) surface, marked by the solid line, there are three In atoms (blue, dark) which are adsorbed on top of Si(111) atoms (red, bright). This adsorption behavior is similar to the behavior of NH_3 on Si(111) as observed by Wolkow et al. [183].

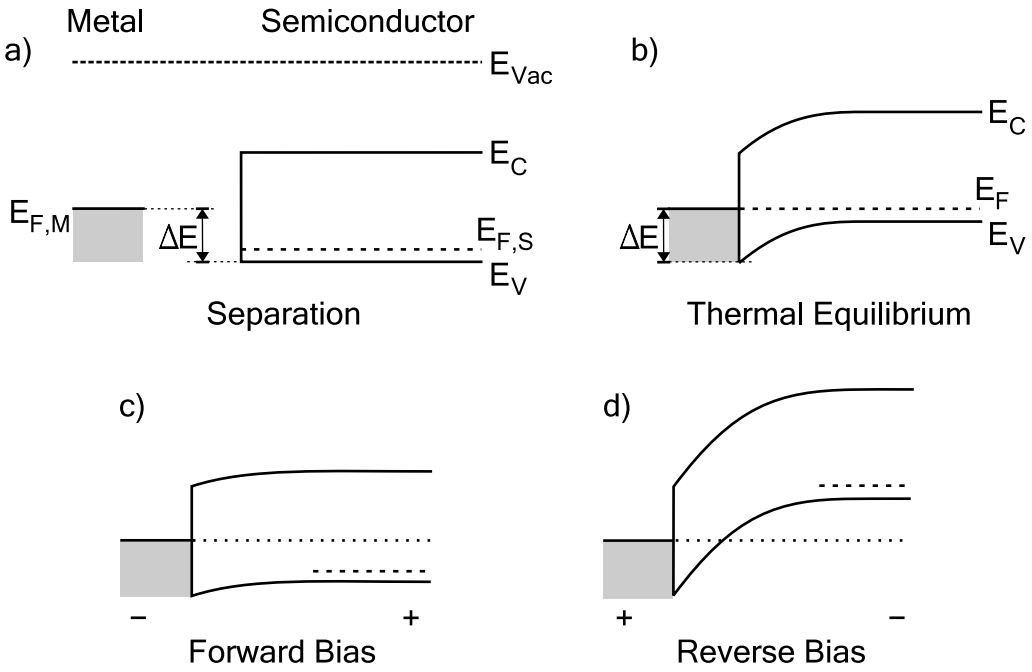

Figure B.5: Band structure in a junction of a metal (tip) and a p-doped semiconductor. E_{Vac}: Vacuum level; $E_{F,M}$: Fermi-level of the metal; $E_{F,S}$: Fermi-level of the semiconductor; E_V, E_C: Valence band edge and conduction band edge of the semiconductor.
a) When the metal (tip) and the semiconductor are separated, the energy difference ΔE arises between $E_{F,M}$ and E_V because the vacuum levels of metal and tip are the same. b) When in contact, the Fermi levels of metal and semiconductor adjust. Because ΔE is fixed, the band structure of the semiconductor has to bend. c) When applying a positive voltage to the semiconductor, its Fermi level is lowered and electrons can move from the metal to the semiconductor, the junction is conductive. d) When applying a negative voltage to the semiconductor, its Fermi level is raised, electrons are blocked. The junction is insulating. (Adapted from [45].)

They observed that NH_3, after dissociating to NH_2 and H, adsorbs preferentially on top of Si so called *center atoms* which are the six atoms in the unit cell that do not lie at the corners. Using STS, they found that the dangling bond states of the center atoms are less occupied than the corresponding states of the corner atoms, leading to a larger reactivity. This observation also explains the preferred adsorption of In atoms on the center atoms of the Si(111)-(7×7) surface.

The observed arrangement of In atoms appears to be a preliminary stage to the Si(111)-($\sqrt{31} \times \sqrt{31}$)In superstructure as observed by Kraft et al. [176]. Imaging the unoccupied states of this system, they found diamond shaped unit cells of In consisting of two triangles with 6 resp. 10 In atoms. It is possible that this structure develops from the structure observed here. However, it has to be mentioned that imaging the *occupied* states did not reveal atomic resolution,

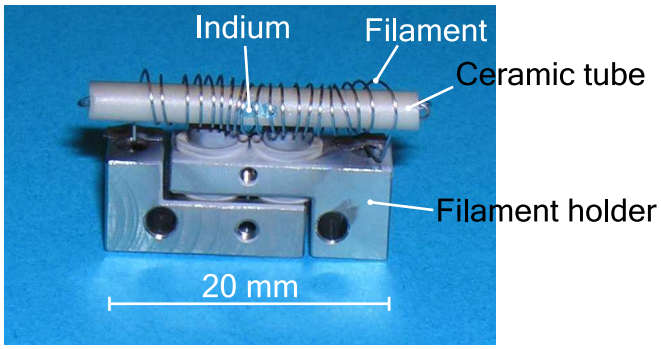

Figure B.6: The In-evaporator. Chunks of In are in the ceramics tube, which is heated and supported by the coil. The holder is a standard filament holder. The evaporation parameters are $I = 2.7\,A$, $U = 10.2\,V$.

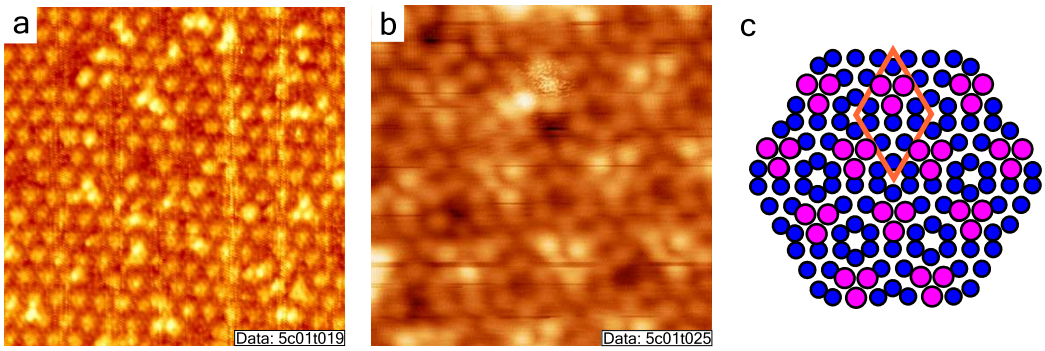

Figure B.7: a) Large-scale view of Si(111)-In. Hexagonally ordered bright triangles are visible on the surface. ($35\,nm \times 35\,nm$; Tunneling parameters: $U = 2.0\,V$, $I = 0.1\,nA$) b) Close-up view of the superstructure. Si atoms of the surface are visible. The triangles consist of three bright protrusions. ($8.0\,nm \times 8.0\,nm$; Tunneling parameters: $U = 2.0\,V$, $I = 0.1\,nA$) c) Model of Si(111)-(7×7)In. Red (bright): Si atoms; Blue (dark): In atoms; Solid line: Si(111) unit cell. In each unit cell, there are three In atoms which are adsorbed on top of Si atoms.

therefore the authors doubted that a simple geometric model could be applied [176].

Constant-current imaging and dI/dU-mapping at different voltages, shown in Fig. B.8, reveals the electronic properties. At voltages below 1.8 V, the In atoms are not visible in constant-current images, only the reconstructed Si(111) surface can be seen. At 1.8 V, the In atoms slowly appear, and are clearly visible at larger voltages. In dI/dU-maps, the density of states of the In atoms become gradually brighter at voltages larger than 1.6 V.

The density of states of In on Si(111) has been studied for different superstructures with IPES by Hill et al. [177] They examined the (4×1) single-domain as well as the three-domain structure and the $(\sqrt{3} \times \sqrt{3})$ structure. For each of these structures they found that the DOS vanishes near the Fermi level. For

the ($\sqrt{3} \times \sqrt{3}$) structure, which is closest in coverage to the structure examined here, the DOS has its first maximum at $\approx$1 eV and stays large for higher energies. Taking into account that the tunneling current is the integral of the LDOS, this can explain the invisibility of single In atoms on Si(111)-7×7.

The invisibility of In atoms raises the question if the tip might touch the atoms during scanning since it is not retracted when moving over them. Indium atoms have a diameter of 4 Å, the covalent diameter is 3 Å [184]. Since the tunneling current was rather small (0.1 nA), the tip-sample distance is large enough ($>$ 5 Å) so that the tip does not touch the atoms.

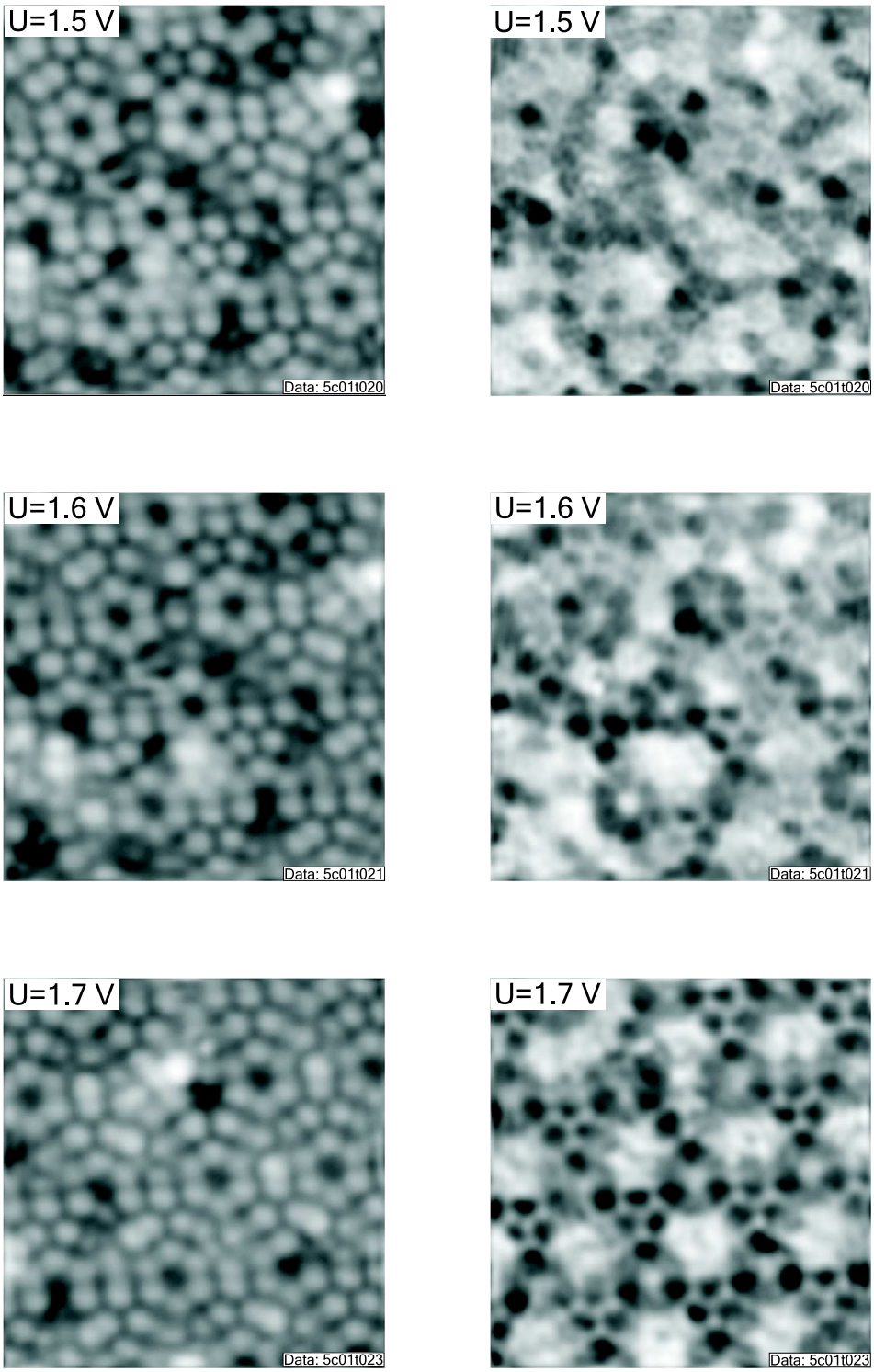

Figure B.8: Constant-current images (left) and $\mathrm{dI/dU}$ maps (right) of Si(111)-In at different voltages. ($8.0\,\mathrm{nm}\times 8.0\,\mathrm{nm}$; Tunneling current: $\mathrm{I} = 0.1\,\mathrm{nA}$; filtered)

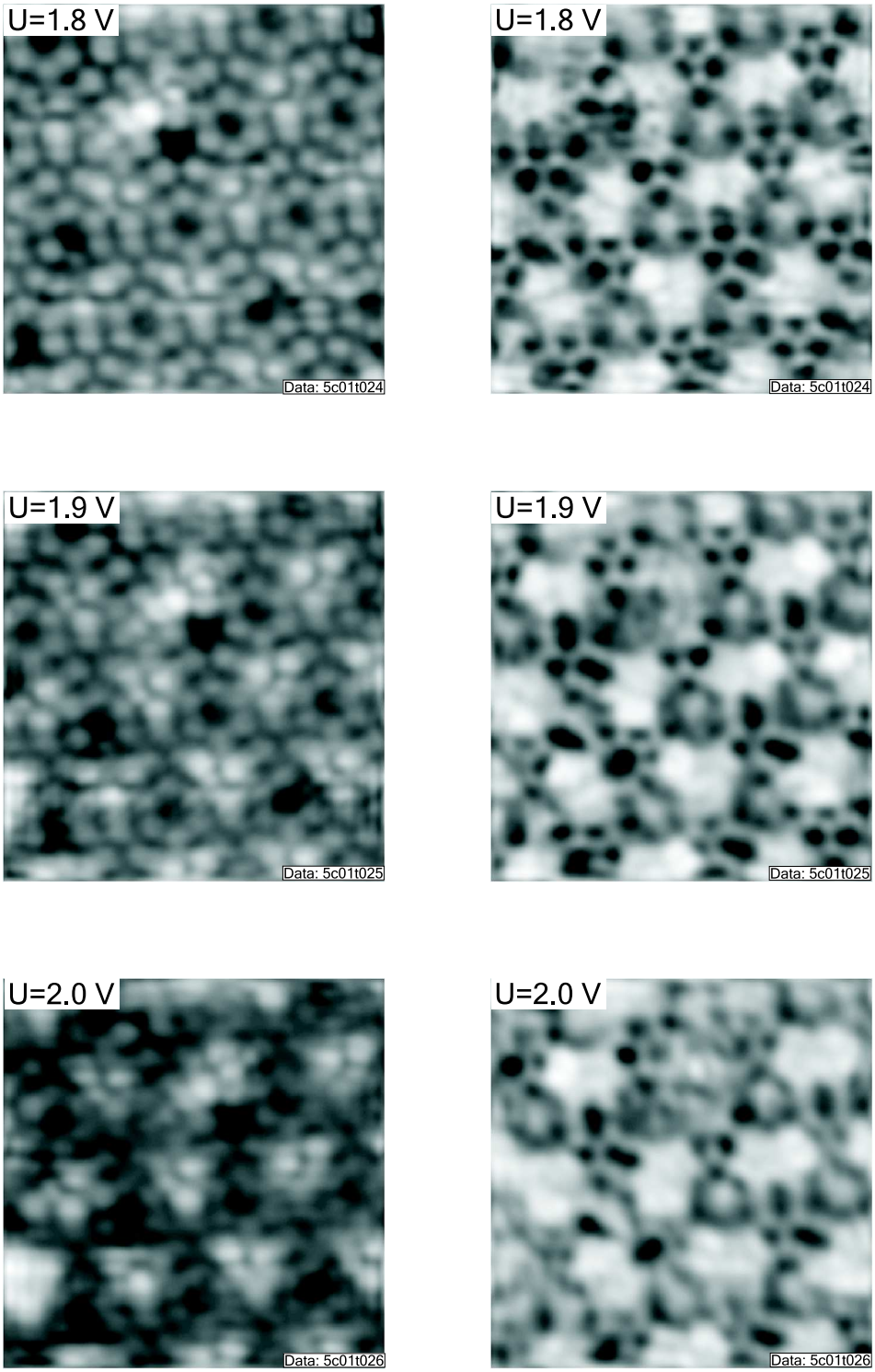

Figure B.8 (continued): Constant-current images (left) and dI/dU maps (right) of Si(111)-In at different voltages. (8.0 nm×8.0 nm; Tunneling current: $I = 0.1$ nA; filtered)

Acknowledgments

A work like this can not be accomplished without a lot of help. I thank

Prof. Dr. Richard Berndt for the possibility to work in his group, introducing me to the world of STM, his many tips and fruitful discussions,

Priv.-Doz. Dr. Jörg Kröger, who guided me for the past years and let me work on 'his' STM,

Mr. Suren, Mr. Brach, Mr. Brix, Mr. Willing and the staff of the workshop for their tips for construction design and the fast and precise manufacturing,

Jörg Neubauer for help with and creation of fancy electronic devices,

Dr. Jürgen Rathlev for his help with computer problems,

Dr. Fischer, Dr. Kuntze and the complete staff of central administration who handled our orders,

the rest of the group: Dr. Thomas Jürgens, Patrick Schmidt, Henning Jensen, Dr. Laurent Limot, Dr. Nicolas Néel, Dr. Carlos Manzano, Hongna Wang, Xin Ge, Hans Grothmann, Heinz-Georg Börst, Michael Becker and Uschi Götzke for the great working atmosphere, fruitful discussions and a lot of fun.

last but not least my parents, who always encouraged me in my studies.

Part of this work was supported by the DFG-Schwerpunktprogramm 1093, which is gratefully acknowledged.

Lebenslauf

Name:	von Hofe
Vorname:	Thomas
Geburtsdatum:	24. Februar 1975
Geburtsort:	Krefeld
Staatsangehörigkeit:	deutsch
Familienstand	ledig

August 1981 - September 1981	Grundschule Bismarckstraße, Krefeld
Januar 1982 - Dezember 1983	Goethe-Schule, Buenos Aires, Argentinien
Januar 1984 - Juli 1985	Grundschule Bismarckstraße, Krefeld
August 1985 - Juli 1994	Gymnasium am Stadtpark, Krefeld
Juli 1994	Abitur
Oktober 1994	Beginn des Physikstudiums an der RWTH Aachen
Oktober 1995 - Juli 1996	Grundwehrdienst an der TSH/FSHT in Eschweiler
August 1997	Vordiplom in Physik
Februar 2001	Diplom in Physik
Februar 2001 - September 2001	Wissenschaftlicher Mitarbeiter am II. Physikalischen Institut der RWTH Aachen
September 2001	Beginn der Promotion an der CAU Kiel bei Prof. Berndt

Eidesstattliche Erklärung

Hiermit erkläre ich an Eides Statt, dass ich diese Arbeit selbständig unter der Beratung meiner wissenschaftlichen Lehrer und nur mit den angegebenen Hilfsmitteln erstellt habe. Diese Arbeit wurde weder ganz noch in Teilen an anderer Stelle im Rahmen eines Prüfungsverfahrens vorgelegt. Frühere Promotionsversuche wurden von mir nicht vorgenommen.

Kiel, den

Bibliography

[1] G. Moore. Electronics Magazine, 19 April 1965.

[2] D.P. Woodruff and T.A. Delchar. *Modern Techniques of Surface Science*. Cambridge University Press, Cambridge, UK, 2nd edition, 1994.

[3] G. Binnig and H. Rohrer. Helvetica Physica Acta **55**, 726 (1982).

[4] G. Binnig, H. Rohrer, Ch. Gerber, and E. Weibel. Appl. Phys. Lett. **40**, 178 (1982).

[5] G. Binnig, H. Rohrer, Ch. Gerber, and E. Weibel. Phys. Rev. Lett. **50**, 120 (1983).

[6] E. Burstein and S. Lundqvist (Eds.). *Tunneling Phenomena in Solids*. Plenum Press, New York, 1969.

[7] R.S. Becker, J.A. Golovchenko, and B.S. Swartzentruber. Phys. Rev. Lett. **55**, 987 (1985).

[8] G. Binnig, K.H. Frank, H. Fuchs, N. Garcia, B. Reihl, H. Rohrer, F. Salvan, and A.R. Williams. Phys. Rev. Lett. **55**, 991 (1975).

[9] B.C. Stipe, M.A. Rezaei, and W. Ho. Science **280**, 1732 (1998).

[10] F. Schwabl. *Quantenmechanik*. Springer Verlag, Berlin, 1998.

[11] J. Tersoff and D.R. Hamann. Phys. Rev. Lett. **50**, 1998 (1983).

[12] J. Tersoff and D.R. Hamann. Phys. Rev. B **31**, 805 (1985).

[13] N.D. Lang. Phys. Rev. B **34**, 5947 (1986).

[14] Thomas Jürgens. *Aufbau und Test eines Raumtemperatur-Ultrahochvakuum-Rastertunnelmikroskops*. PhD thesis, Christian-Albrechts-Universität zu Kiel, 2003.

[15] G. Binnig, H. Rohrer, Ch. Gerber, and E. Weibel. Phys. Rev. Lett. **49**, 57 (1982).

[16] N.D. Lang. Phys. Rev. Lett. **56**, 1164 (1986).

[17] N.D. Lang. Phys. Rev. Lett. **58**, 45 (1987).

[18] F. Calleja, A. Arnau, J.J. Hinarejos, A.L. Vázquez de Parga, W.A. Hofer, P.M. Echenique, and R. Miranda. Phys. Rev. Lett. **92**, 206101 (2004).

[19] G. Binnig and H. Rohrer. Phys. Rev. Mod. **59**, 615 (1987).

[20] D. Bonnell (Ed.). *Scanning Probe Microscopy and Spectroscopy*. Wiley-VCH, New York, 2001.

[21] A.M. Russell and D.A. Torchia. Rev. Sci. Instrum. **33**, 442 (1962).

[22] M.L. Meade. *Lock-in amplifiers: principles and applications*. Peter Peregrinus Ltd., London, UK, 1983.

[23] G.V.H. Wilson. J. Appl. Phys. **34**, 3276 (1963).

[24] J.G. Simmons. J. Appl. Phys. **34**, 1793 (1963).

[25] N.D. Lang. Phys. Rev. B **37**, 10395 (1988).

[26] H.F. Hess, R.B. Robinson, R.C. Dynes, J.M. Valles, Jr., and J.V. Waszczak. Phys. Rev. Lett. **62**, 214 (1989).

[27] M.F. Crommie, C.P. Lutz, and D.M. Eigler. Nature (London) **363**, 524 (1993).

[28] E.J. Heller, M.F. Crommie, C.P. Lutz, and D.M. Eigler. Nature (London) **369**, 464 (1994).

[29] Ph. Avouris, I.-W. Lyo, R.E. Walkup, and Y. Hasegawa. J. Vac. Sci. Technol. B **12**, 1447 (1994).

[30] J. Li, W.-D. Schneider, and R. Berndt. Phys. Rev. B **56**, 7656 (1997).

[31] P. Wahl, M.A. Schneider, L. Diekhöner, R. Vogelgesang, and K. Kern. Phys. Rev. Lett. **91**, 106802 (2003).

[32] Henning Jensen. *Zusammenbau eines Rastertunnelmikroskops und erste Messungen an einkristallinen Metalloberflächen*. Diploma thesis, Christian-Albrechts-Universität zu Kiel, 2003.

[33] H. Brune, G.S. Bales, J. Jacobsen, C. Boragno, and K. Kern. Phys. Rev. B **60**, 5991 (1999).

[34] M. Morgenstern, Th. Michely, and G. Comsa. Phys. Rev. Lett. **79**, 1305 (1997).

[35] L.J. Lauhon and W. Ho. Rev. Sci. Instrum. **72**, 216 (2001).

[36] L.J. Lauhon and W. Ho. Phys. Rev. Lett. **85**, 4566 (2000).

[37] L. Ottaviano, M. Crivellari, G. Profeta, A. Continenza, L. Lozzi, and S. Santucci. J. Vac. Sci. Technol. A **18**, 1946 (2000).

[38] T.P. Pearl and S.J. Sibener. Rev. Sci. Instrum. **71**, 124 (2000).

[39] W.W. Crew and R.J. Madix. Rev. Sci. Instrum. **66**, 4552 (1995).

[40] A.J. Leavitt, T. Han, J.M. Williams, R.S. Bryner, D.L. Patrick, C.E. Rabke, and Th.P. Beebe, Jr. Rev. Sci. Instrum. **65**, 75 (1994).

[41] H.-P. Rust, M. Doering, J.I. Pascual, T.P. Pearl, and P.S. Weiss. Rev. Sci. Instrum. **72**, 4393 (2001).

[42] L. Petersen, M. Schunack, B. Schaefer, T.R. Linderoth, P.B. Rasmussen, P.T. Sprunger, E. Laegsgaard, I. Stensgaard, and F. Besenbacher. Rev. Sci. Instrum. **72**, 1438 (2001).

[43] N.W. Ashcroft and N.D. Mermin. *Solid State Physics*. Saunders College Publishing, Fort Worth, USA, 1976.

[44] E.S.R. Gopal. *Specific Heats at Low Temperatures*. Heywood Books, London, 1966.

[45] S.M. Sze. *Physics of Semiconductor Devices*. John Wiley & Sons, New York, 1981.

[46] L. Bergmann and C. Schaefer. *Lehrbuch der Experimentalphysik*. Walter de Gruyter, Berlin, 1974.

[47] G.K. White. *Experimental Techniques in Low-Temperature Physics*. Oxford University Press, Oxford, UK, 1968.

[48] Internet-database *Engineering Fundamentals*, `www.efunda.com`.

[49] Jörg Kliewer. *Dynamics and Manipulation of Surface States*. PhD thesis, Rheinisch-Westfälische Technische Hochschule, 2000.

[50] Homepage of Kinetic Systems Inc., `www.kineticsystems.com`.

[51] H. Ibach and H. Lüth. *Festkörperphysik – Einführung in die Grundlagen*. Springer Verlag, Berlin, 1995.

[52] S.G. Davison and M. Stęślicka. *Basic Theory of Surface States*. Oxford University Press, Oxford, UK, 1992.

[53] A. Zangwill. *Physics at Surfaces*. Cambridge University Press, Cambridge, UK, 1988.

[54] I.E. Tamm. Z. Phys. **76**, 849 (1932).

[55] I.E. Tamm. Phys. Z. Sowjet **1**, 733 (1932).

[56] W. Shockley. Phys. Rev. **56**, 317 (1939).

[57] N. Memmel. Surf. Sci. Rep. **32**, 91 (1998).

[58] P.M. Echenique, R. Berndt, E.V. Chulkov, Th. Fauster, A. Goldmann, and U. Höfer. Surf. Sci. Rep. **52**, 219 (2004).

[59] P. Heimann, J. Hermanson, and H. Miosga. Phys. Rev. B **20**, 3059 (1979).

[60] W. Shockley. *Electrons and Holes in Semiconductors*. Van Nostrand, New York, 1950.

[61] J.D. Jackson. *Classical Electrodynamics*. John Wiley & Sons, New York, 1962.

[62] P.M. Echenique and J.B. Pendry. J. Phys. C: Solid State Phys. **11**, 2065 (1978).

[63] P.J. Jennings, R.O. Jones, and M. Weinert. Phys. Rev. B **37**, 6113 (1988).

[64] J. Rundgren and G. Malmström. J. Phys. C: Solid State Phys. **10**, 4671 (1977).

[65] M. Weinert, S.L. Hulbert, and P.D. Johnson. Phys. Rev. Lett. **55**, 2055 (1985).

[66] E.T. Whittaker and G.N. Watson. *A Course in Modern Analysis*. Cambridge University Press, Cambridge, UK, 4th edition, 1958.

[67] R. Loudon. Am. J. Phys. **27**, 649 (1959).

[68] J.H. Coombs and J.K. Gimzewski. J. Microsc. **152**, 841 (1988).

[69] T. Ando, A.B. Fowler, and F. Stern. Rev. Mod. Phys. **54**, 437 (1982).

[70] J.A. Kubby and W.J. Greene. Phys. Rev. B **48**, 11249 (1993).

[71] M. Milun, P. Pervan, and D.P. Woodruff. Rep. Prog. Phys. **65**, 99 (2002).

[72] T.-C. Chiang. Surf. Sci. Rep. **39**, 181 (2000).

[73] E.G. McRae. Rev. Mod. Phys. **51**, 541 (1979).

[74] E.G. McRae and M.L. Kane. Surf. Sci. **108**, 435 (1981).

[75] P.M. Echenique and J.B. Pendry. Prog. Surf. Sci. **32**, 111 (1989).

[76] E.N. Economou. *Green's Functions in Quantum Physics*. Springer Verlag, Berlin, 1983.

[77] W. Nolting. *Grundkurs Theoretische Physik 7: Viel-Teilchen-Theorie*. Vieweg, Braunschweig, 1997.

[78] J. Hedin and S. Lundqvist. Solid State Phys. **23**, 1 (1969).

[79] P.M. Echenique, J. Osma, M. Machado, V.M. Silkin, E.V. Chulkov, and J.M. Pitarke. Prog. Surf. Sci. **67**, 271 (2001).

[80] E.V. Chulkov, J. Kliewer, R. Berndt, V.M. Silkin, B. Hellsing, S. Crampin, and P.M. Echenique. Phys. Rev. B **68**, 195422 (2003).

[81] J.J. Quinn and R.A. Ferrell. Phys. Rev. **112**, 812 (1958).

[82] P.M. Echenique, J.M. Pitarke, E.V. Chulkov, and A. Rubio. Chem. Phys. **251**, 1 (2000).

[83] B. Hellsing, A. Eiguren, and E.V. Chulkov. J. Phys.: Condens. Matter **14**, 5959 (2002).

[84] J. Kliewer, R. Berndt, E.V. Chulkov, V.M. Silkin, P.M. Echenique, and S. Crampin. Science **288**, 1399 (2000).

[85] J. Tersoff and S.D. Kevan. Phys. Rev. B **28**, 4267 (1983).

[86] S.D. Kevan. Phys. Rev. B **33**, 4364 (1986).

[87] C. Corriol, V.M. Silkin, D. Sánchez-Portal, A. Arnau, E.V. Chulkov, P.M. Echenique, T. von Hofe, J. Kliewer, J. Kröger, and R. Berndt. Phys. Rev. Lett. **95**, 176802 (2005).

[88] J. Li, W.-D. Schneider, R. Berndt, O.R. Bryant, and S. Crampin. Phys. Rev. Lett. **81**, 4464 (1998).

[89] J. Klein, A. Léger, M. Belin, D. Défourneau, and M.J.L. Sangster. Phys. Rev. B **7**, 2336 (1973).

[90] L. Vitali, P. Wahl, M.A. Schneider, K. Kern, V.M. Silkin, E.V. Chulkov, and P.M. Echenique. Surf. Sci. **523**, L47 (2003).

[91] J.W. Döbereiner. *Zur Chemie des Platins in Wissenschaftlicher und Technischer Beziehung*. Balzsche Buchhandlung, Stuttgart, 1936.

[92] J.E. Ortega, E.M. Oellig, J. Ferron, and R. Miranda. Phys. Rev. B **36**, 6213 (1987).

[93] M. Tikhov, G. Rangelov, and L. Surnev. Surf. Sci. **231**, 280 (1990).

[94] G. Faraci and A.R. Pennisi. Surf. Sci. **409**, 46 (1998).

[95] S.Y. Davydov. Appl. Surf. Sci. **140**, 58 (1999).

[96] J.B. Taylor and I. Langmuir. Phys. Rev. **44**, 423 (1933).

[97] A.H. Somer. *Photoemissive Materials*. Wiley-VCH, New York, 1968.

[98] J.P. Muscat and D.M. Newns. Prog. Surf. Sci. **9**, 1 (1978).

[99] N.D. Lang. In *Physics and Chemistry of Alkali Metal Adsorption*, page 11. Elsevier, Amsterdam, 1989.

[100] K. Wandelt. In *Physics and Chemistry of Alkali Metal Adsorption*, page 25. Elsevier, Amsterdam, 1989.

[101] W.C. Fan and A. Ignatiev. Phys. Rev. B **37**, 5274 (1988).

[102] J. Cousty and R. Riwan. Surf. Sci. **204**, 45 (1988).

[103] D. Tang, D. McIlroy, X. Shi, C. Su, and D. Heskett. Surf. Sci. **255**, L497 (1991).

[104] Z.Y. Li, K.M. Hock, and R.E. Palmer. Phys. Rev. Lett. **67**, 1562 (1991).

[105] G.S. Leatherman and R.D. Diehl. Phys. Rev. B **53**, 4939 (1996).

[106] T. Masuda, C.J. Barnes, P. Hu, and D.A. King. Surf. Sci. **276**, 122 (1992).

[107] D.K. Flynn-Sanders, K.D. Jamison, J.V. Barth, J. Wintterlin, P.A. Thiel, G. Ertl, and B.J. Behm. Surf. Sci. **253**, 270 (1991).

[108] P. Kaukasoina, M. Lindroos, R.D. Diehl, D. Fisher, S. Chandavarkar, and I.R. Collins. J. Phys.: Condens. Matter **5**, 2875 (1993).

[109] D. Fisher and R.D. Diehl. Phys. Rev. B **46**, 2512 (1992).

[110] N.J. Wu, Z.P. Hu, and A. Ignatiev. Phys. Rev. B **43**, 3805 (1992).

[111] G. Pirug and H.P. Bonzel. Surf. Sci. **194**, 159 (1988).

[112] D.L. Doering and S. Semancik. Surf. Sci. **175**, L730 (1986).

[113] D.L. Doering and S. Semancik. Phys. Rev. Lett. **53**, 66 (1984).

[114] G. Besold, T. Schaffroth, K. Heinz, G. Schmidt, L. Hammer, K. Heinz, and K. Müller. Surf. Sci. **189/190**, 252 (1987).

[115] F. Grey and J. Bohr. In *Phase Transitions in Surface Films 2*, page 83. Plenum Press, New York, 1991.

[116] D.L. Doering. J. Vac. Sci. Technol. A **3**, 809 (1985).

[117] A.D. Novaco and J.P. McTague. Phys. Rev. Lett. **38**, 1286 (1977).

[118] J.P. McTague and A.D. Novaco. Phys. Rev. B **19**, 5299 (1979).

[119] H. Shiba. J. Phys. Soc. Jpn. **46**, 1852 (1979).

[120] H. Shiba. J. Phys. Soc. Jpn. **48**, 211 (1980).

[121] S. Andersson and J.B. Pendry. Solid States Commun. **16**, 563 (1975).

[122] J.E. Demuth, D.W. Jepsen, and P.M. Marcus. J. Phys. C: Solid States Phys. **8**, L25 (1975).

[123] C. von Eggeling, G. Schmidt, G. Besold, L. Hammer, K. Heinz, and K. Müller. Surf. Sci. **221**, 11 (1989).

[124] S. Aminpirooz, A. Schmalz, L. Becker, N. Pangher, J. Haase, M.M. Nielsen, D.R. Batchelor, E. Bøgh, and D.L. Adams. Phys. Rev. B **46**, 15594 (1992).

[125] U. Muschiol, P. Bayer, K. Heinz, W. Oed, and J.B. Pendry. Surf. Sci. **275**, 185 (1992).

[126] S. Mizuno, H. Tochihara, and T. Kawamura. Surf. Sci. **293**, 239 (1993).

[127] W. Berndt, D. Weick, C. Stampfl, A.M. Bradshaw, and M. Scheffler. Surf. Sci. **330**, 182 (1995).

[128] S.Å. Lindgren, L. Walldén, J. Rundgren, P. Westrin, and J. Neve. Phys. Rev. B **28**, 6707 (1983).

[129] M. Kerkar, D. Fisher, D.P. Woodruff, R.G. Jones, R.D. Diehl, and B. Cowie. Phys. Rev. Lett. **68**, 3204 (1992).

[130] D. Fisher, S. Chandavarkar, I.R. Collins, R.D. Diehl, P. Kaukasoina, and M. Lindroos. Phys. Rev. Lett. **68**, 2786 (1992).

[131] S. Schwegmann and H. Over. Surf. Sci. **360**, 271 (1996).

[132] R.D. Diehl and R. McGrath. Surf. Sci. Rep. **23**, 43 (1996).

[133] W.C. Fan and A. Ignatiev. J. Vac. Sci. Technol. A **6**, 735 (1988).

[134] I. langmuir and J.B. Taylor. Phys. Rev. **40**, 463 (1932).

[135] Z. Sidorski, I. Pelly, and R. Gomer. J. Chem. Phys. **50**, 2382 (1969).

[136] R.L. Gerlach and T.N. Rhodin. Surf. Sci. **19**, 403 (1970).

[137] G. Brodén and H.P. Bonzel. Surf. Sci. **84**, 106 (1979).

[138] J.E. Crowell, E.L. Garfunkel, and G.A. Somorjai. Surf. Sci. **121**, 303 (1982).

[139] N. Fischer, S. Schuppler, Th. Fauster, and W. Steinmann. Surf. Sci. **314**, 89 (1994).

[140] S.Å. Lindgren and L. Walldén. Phys. Rev. B **22**, 5967 (1980).

[141] S.Å. Lindgren and L. Walldén. Surf. Sci. **211/212**, 394 (1989).

[142] R. Dudde and B. Reihl. Surf. Sci. **287/288**, 614 (1993).

[143] D.A. Arena, F.G. Curti, and R.A. Bartynski. Phys. Rev. B **56**, 15404 (1997).

[144] S.Å. Lindgren and L. Walldén. Phys. Rev. B **38**, 3060 (1988).

[145] A. Carlsson, B. Hellsing, S.-Å. Lindgren, and L. Walldén. Phys. Rev. B **56**, 1593 (1997).

[146] G.M. Watson, P.A. Brühwiler, H.J. Sagner, K.H. Frank, and E.W. Plummer. Phys. Rev. B **50**, 17678 (1994).

[147] K.-H. Frank, H.-J. Sagner, and D. Heskett. Phys. Rev. B **40**, 2767 (1989).

[148] H. Petek and S. Ogawa. Prog. Surf. Sci. **56**, 239 (1997).

[149] D. Wegner, A. Bauer, and G. Kaindl. Phys. Rev. Lett. **94**, 126804 (2005).

[150] L. Bürgi, O. Jeandupeux, H. Brune, and K. Kern. Phys. Rev. Lett. **82**, 4516 (1999).

[151] K.F. Braun and K.H. Rieder. Phys. Rev. Lett. **88**, 096801 (2002).

[152] SAES Getters (Deutschland) GmbH, Gerolsteiner Strasse 1, 50937 Köln, Germany.

[153] K.H. Lau and W. Kohn. Surf. Sci. **65**, 607 (1977).

[154] J. Friedel. Nuovo Cimento Suppl. **7**, 287 (1958).

[155] K.H. Lau and W. Kohn. Surf. Sci. **75**, 69 (1978).

[156] P. Hyldgaard and M. Persson. J. Phys.: Condens. Matter **12**, L13 (2000).

[157] E. Wahlström, I. Ekvall, H. Olin, and L. Walldén. Appl. Phys. A **66**, S1107 (1998).

[158] J. Repp, F. Moresco, G. Meyer, and K.-H. Rieder. Phys. Rev. Lett. **85**, 2981 (2000).

[159] N. Knorr, H. Brune, M. Epple, A. Hirstein, M.A. Schneider, and K. Kern. Phys. Rev. B **65**, 115420 (2002).

[160] F. Silly, M. Pivetta, M. Ternes, F. Patthey, J.P. Pelz, and W.-D. Schneider. Phys. Rev. Lett. **92**, 016101 (2004).

[161] F. Silly, M. Pivetta, M. Ternes, F. Patthey, J.P. Pelz, and W.-D. Schneider. New Journal of Physics **6**, 16 (2004).

[162] G. Hörmandinger and J.B. Pendry. Phys. Rev. B **50**, 18607 (1994).

[163] F. Grey and J. Bohr. Europhys. Lett. **18**, 717 (1992).

[164] G. Benedek, J. Ellis, A. Reichmuth, P. Ruggerone, H. Schief, and J.P. Toennies. Phys. Rev. Lett. **69**, 2951 (1992).

[165] E. Hulpke, J. Lower, and A. Reichmuth. Phys. Rev. B **53**, 13901 (1996).

[166] G. Witte and J.P. Toennies. Phys. Rev. B **62**, R7771 (2000).

[167] H. Jensen, J. Kröger, R. Berndt, and S. Crampin. Phys. Rev. B **71**, 155417 (2005).

[168] M. Bauer, S. Pawlik, and M. Aeschlimann. Phys. Rev. B **55**, 10040 (1997).

[169] M. Bauer, S. Pawlik, and M. Aeschlimann. Phys. Rev. B **60**, 5016 (1999).

[170] B.N.J. Persson and H. Ishida. Phys. Rev. B **42**, 3171 (1990).

[171] S.Å. Lindgren and L. Walldén. Solid State Commun. **28**, 283 (1978).

[172] J. Kliewer and R. Berndt. Phys. Rev. B **65**, 035412 (2001).

[173] C.T. Campbell. J. Phys. Chem. **89**, 5789 (1985).

[174] J.J. Lander and J. Morrison. J. Appl. Phys. **36**, 1706 (1965).

[175] H. Öfner, S.L. Surnev, Y. Shapira, and F.P. Netzer. Phys. Rev. B **48**, 10940 (1993).

[176] J. Kraft, M.G. Ramsey, and F.P. Netzer. Phys. Rev. B **55**, 5384 (1997).

[177] I.G. Hill and A.B. McLean. Phys. Rev. B **56**, 15725 (1997).

[178] J. Kuntze. private communication.

[179] W. Krüger. Private communication.

[180] M. Kawaji, S. Baba, and A. Kinbara. Appl. Phys. Lett. **34**, 748 (1979).

[181] R.G. Musket, W. McLean, C.A. Colmenares, D.M. Makowiecki, and W.J. Siekhaus. Appl. Surf. Sci. **10**, 143 (1982).

[182] Ph. Avouris, I.-W. Lyo, and Y. Hasegawa. J. Vac. Sci. Technol. A **11**, 1725 (1992).

[183] R. Wolkow and Ph. Avouris. Phys. Rev. Lett. **60**, 1049 (1988).

[184] *Table of Periodic Properties of the Elements*. Sargent-Welch, Skokie, USA, 1980.